Translatome analysis and *in vivo* Ca^{2+} imaging of astrocytes in an Alzheimer's disease mouse model

Dissertation zur Erlangung
des Doktorgrades (Dr. rer. nat.)
der Mathematisch-Naturwissenschaftlichen Fakultät
der Rheinischen Friedrich-Wilhelms-Universität Bonn

Vorgelegt von:

Nelli Blank

Aus
Iwanowka, Kirgisistan

Bonn 2020

Angefertigt mit Genehmigung der Mathematisch-Naturwissenschaftlichen Fakultät der Rheinischen Friedrich-Wilhelms-Universität Bonn

1. Gutachter: Prof. Dr. Gabor C. Petzold
2. Gutachter: Prof. Dr. Michael Pankratz

Tag der Promotion 15.01.2021
Erscheinungsjahr 2021

Table of Content

Summary

One of the most prominent hallmarks of Alzheimer's Disease (AD) is the accumulation of amyloid-beta (Aβ) species, which have the tendency to form extracellular insoluble Aβ plaques and induce reactive astrogliosis in surrounding astrocytes. We have previously shown that peri-plaque reactive astrocytes become hyperactive in mouse models of AD (APP/PS1 and APPPS1-21), and that one key signalling pathway for this hyperactivity is mediated by purinergic signalling. However, it has remained unclear how astrocytes and astrocytic hyperactivity contribute to the onset and progression of AD, how astrocytic gene expression is altered in APP/PS1 mice, and what the consequences of altered gene expression are for astroglial signalling pathways. To identify transcriptional alterations in astrocytes associated with disease progression and/or aging, we precipitated astrocyte-specific messenger RNA (mRNA) in a RiboTag approach that allowed us to perform bulk RNA sequencing specifically from astrocytes isolated from wild type and APP/PS1 mice. To investigate alterations on a functional level, we performed *in vivo* Ca^{2+} imaging in astrocytes of awake behaving mice. To this end, we intravenously injected an adeno-associated virus (AAV) encoding for the green fluorescent calcium indicator GCaMP6f under the control of the astrocyte specific short GFAP promoter. This approach enabled us to longitudinally measure spontaneous Ca^{2+} transients in cortical astrocytes of APPPS1-21 mice and their wild type littermates and moreover, to correlate these data to behaviour and disease progression. Gene set enrichment analysis (GSEA) of upregulated differentially expressed genes (DEGs) in APP/PS1 mice uncovered specific enrichment in genes involved in Ca^{2+} signalling pathways, including several G-protein coupled receptors (GPCRs). Based on this investigation, we found the α1-adrenoceptor (α1-AR) *Adra1d* was upregulated in the stage before disease onset and in the early stage of Aβ pathology in APP/PS1 mice as well as during aging in wild type mice. To validate this result, we performed *in situ* hybridization of two different α1-AR genes, *Adra1a* and *Adra1d*, confirming an increased expression of both genes in cortical reactive astrocytes in APPPS1-21 mice. In other studies, it has been shown that Ca^{2+} responses in cortical astrocytes are induced by activation of α1-adrenergic signalling and that the release of the neurotransmitter (NT) norepinephrine (NE) is dependent on the behavioural state. Indeed, we detected a locomotion-triggered increase of Ca^{2+} transient frequency and prolonged signals in cortical astrocytes in APPPS1-21 mice. Together, these results indicate a contribution of α1-ARs in behaviour-associated Ca^{2+} signalling of cortical astrocytes related to Aβ pathology, which may lead to a better understanding of the role of α1-adrenergic signalling in astroglial-neuronal network dysfunction in AD.

1 Introduction

1.1 Alzheimer's disease

1.1.1 Brief history and neuropathological hallmarks

More than 100 years ago, the German physician Alois Alzheimer for the first time described a "peculiar" disease of the cerebral cortex. The clinical symptoms he observed in the case of his patient Auguste Deter were temporal and spatial disorientation and memory deficits. After her death at the age of 55, her brain featured a severe atrophy, neuritic plaques, neurofibrillary tangles (NFTs) and amyloid angiopathy, which all became the hallmarks of Alzheimer's disease (AD). Alzheimer correlated these abnormal structures and the shrinkage of the brain to the tremendous memory loss and cognitive impairment of Auguste Deter in her years of illness (Alzheimer 1911). In the subsequent 70 years, investigators started focussing on a better scientific understanding of underlying causes of dementia. Dementia is defined as a disease with loss of memory, thinking, orientation, learning, judge, speech, calculation and understanding (Grossman 1992). There are many forms of dementia, however, AD is the most common form and the fourth leading cause of death in the elderly (Katzman 1976). The main neuropathological hallmarks in AD that clearly distinguish the disease from other forms of dementia are the formation of amyloid β (Aβ) plaques in the parenchyma and the intracellular formation of NFTs (Figure 1-1). In addition to these altered structures, Alzheimer described the conspicuous structural changes of

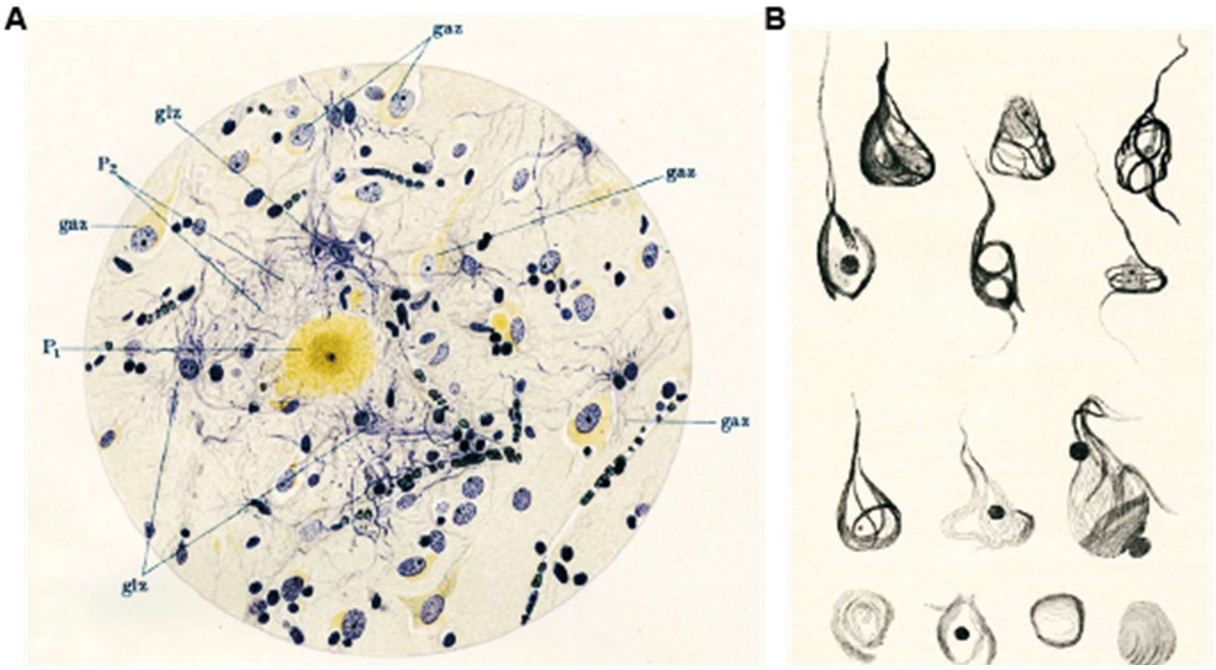

Figure 1-1 Illustrations of the original drawings from Alois Alzheimer published in 1911. (A) showing amyloid plaque deposits (P_1), intraneuronal (gaz) neurofibrillary tangles (NFTs) and gliosis (glz). (B) Drawings from the diverse forms of observed NFTs. (Alzheimer 1911)

glial cells. He especially noticed increased fibre-like structures in glial cells appearing particularly in proximity to Aβ plaques (Alzheimer 1911). These altered structures are potent contributors to neuroinflammatory responses involving microglia and astrocytes (Serrano-Pozo et al. 2013; Pike et al. 1995).

Aβ plaque formation is thought to occur as a first alteration in AD brains (Figure 1-3, red curves). Aβ plaques consist of the Aβ peptide derived from the proteolytic cleavage of the full length amyloid precursor protein (APP). APP processing can occur by α- and γ- secretase, known as the non-amyloidogenic pathway, resulting in soluble products. If APP is processed through the amyloidogenic pathway, APP is first cleaved by the β-secretase (or BACE1) releasing a soluble APPβ (sAPPβ) peptide. The residual transmembrane region and the C-terminus is then further processed by the γ- secretase complex, consisting of presenilin-1 (PS1) and presenilin-2 (PS2) proteins, resulting in the generation of an intracellular APP domain (AICD) and soluble Aβ monomers. Here, the produced Aβ38, Aβ40 and Aβ42 have the tendency to self-aggregate, whereas the Aβ42 peptide is the predominant component of the formed insoluble Aβ plaques in AD (Figure 1-2).

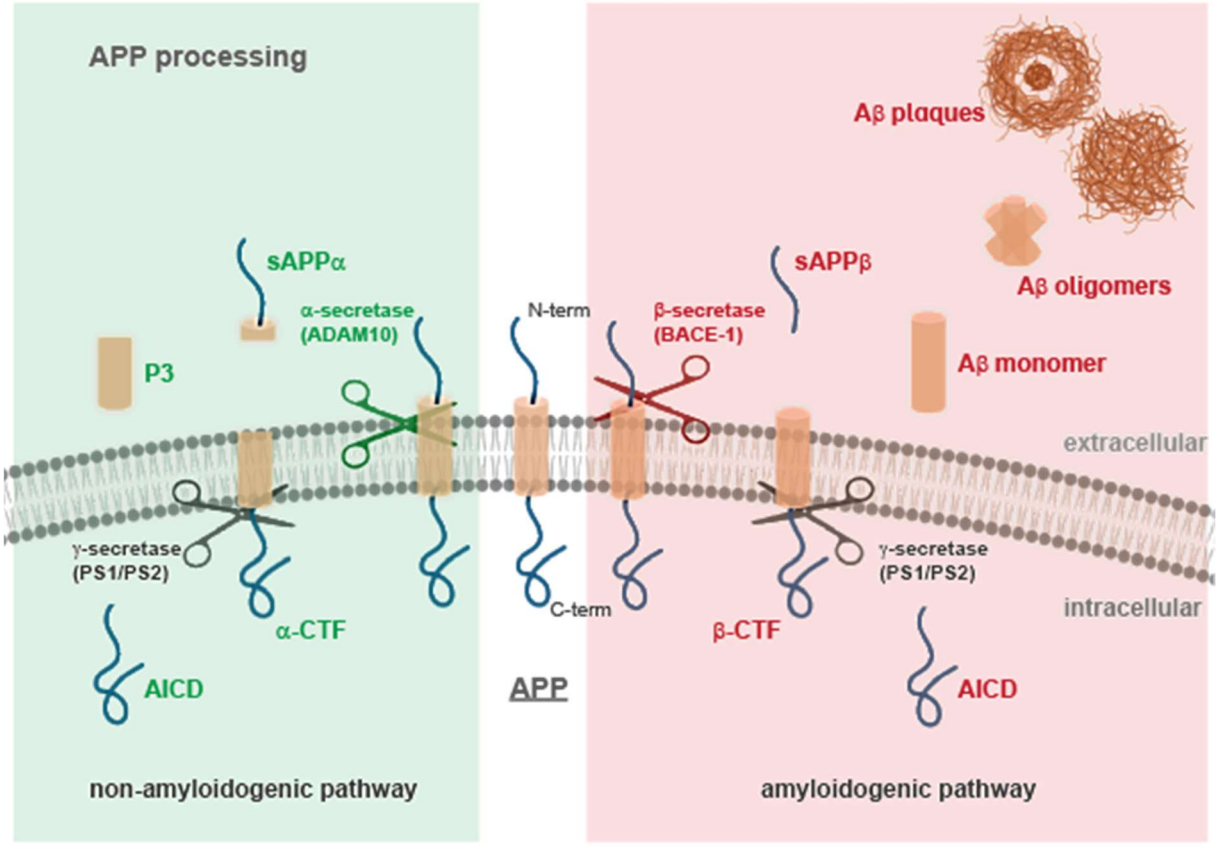

Figure 1-2 Schematic illustration of amyloid precursor protein (APP) processing. Non-amyloidogenic processing (green) facilitated by the cleavage with α-secretase followed by γ-secretase producing first soluble APPα (sAPPα) and α-C-terminal fragment (α-CTF) followed by the P3 peptide secretion in the extracellular space. Amyloidogenic processing (red) facilitated by the cleavage with β-secretase followed by γ-secretase producing first soluble APPβ (sAPPβ) and β-C-terminal fragment (β-CTF) followed by the Aβ monomer secretion in the extracellular space. Aβ monomers then form Aβ oligomers, which finally tend to from insoluble Aβ plaques. Both pathways produce the APP intracellular domain (AICD).

Imbalances between the production and the clearance of the Aβ peptides lead to a formation of soluble Aβ oligomers, which are linked to synaptic dysfunction and cognitive decline (Haass und Selkoe 2007). Furthermore, these soluble Aβ oligomers are prone to from insoluble Aβ plaques. The progressive aggregation of such Aβ plaques was long considered to be the underlying cause of the gradual neurodegeneration in AD. Lately, this concept has been challenged by studies showing that mainly Aβ oligomers of low molecular weight (MW) exhibit disease-relevant activity (Haass und Selkoe 2007; Ferreira et al. 2007). In light of this, it is discussed that low MW Aβ oligomer species exist in a complex equilibrium with soluble high MW Aβ species and insoluble Aβ plaques. Here the low MW Aβ oligomers act as neurotoxic key players in the Aβ pathology by dissociating from Aβ plaques that serve as their reservoir (Haass und Selkoe 2007; Ferreira et al. 2007; Yang et al. 2017; Sakono und Zako 2010).

The second neuropathological hallmark of AD is abnormal phosphorylation of the microtubule-associated protein tau (Figure 1-3, blue curves) (Braak und Braak 1991). Physiologically, tau promotes microtubule stabilization and is thereby involved in the transport of molecules along axons, axonal outgrowth and cell polarity (Drewes et al. 1998). The hyperphosphorylation of tau leads to a dissociation from microtubules and thus, prevents tau to fulfil its normal biological functions. In addition, hyperphosphorylated tau is prone to accumulate, resulting in the development of insoluble inclusions in neurons, the so-called NETs (Figure 1-1B). Loss of tau function and the gain of toxicity mediate the formation of dystrophic neurites that are causative to synaptic loss and neuronal death (Su et al. 1993; Ballatore et al. 2007).

Taken together, Aβ and hyperphosphorylated tau are suggested to cause the massive neuronal loss and neuroinflammation that results in apparent neurodegeneration (Figure 1-3, purple curve) and hence, brain atrophy leading to cognitive impairments (Figure 1-3, green curve) typical of AD (Leuzy et al. 2019). However, it is an ongoing debate whether and to which extent Aβ pathology or tau pathology are actually contributing to the onset that triggers pathological changes in AD (Small und Duff 2008).

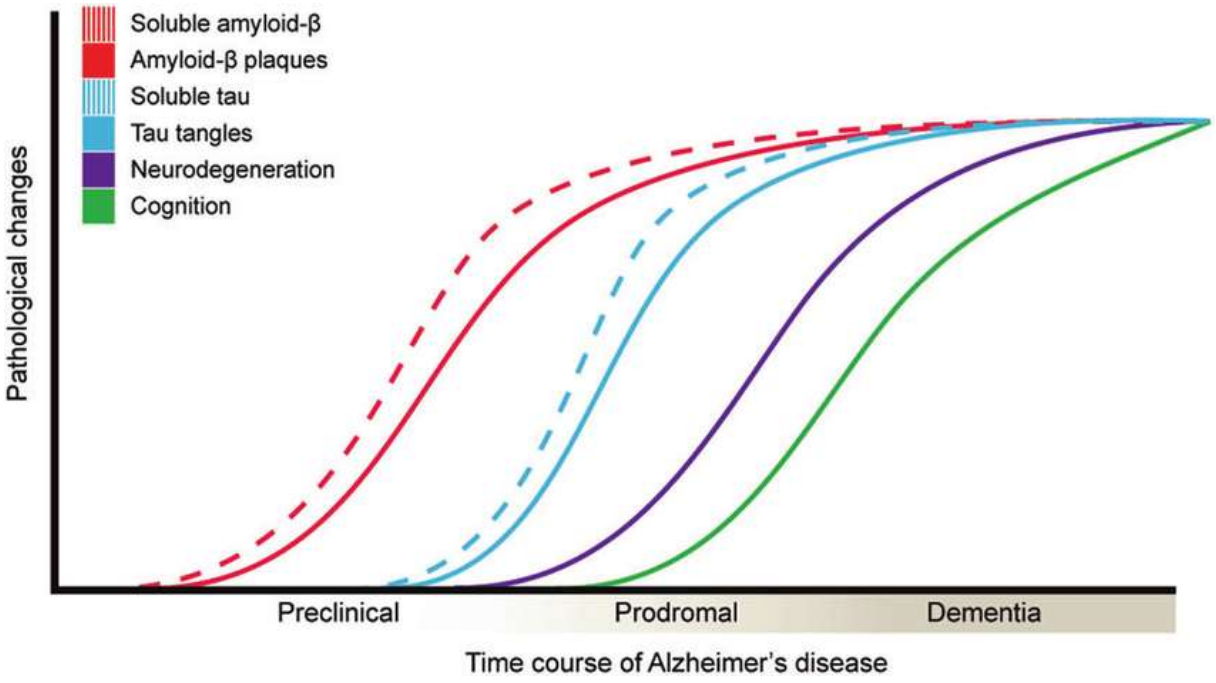

Figure 1-3 Progression hypothesis of pathological changes in Alzheimer's disease (AD). Biomarkers for amyloid β are detectable as abnormally increased in the cerebrospinal fluid (CSF) and in the positron emission tomography (PET) in the preclinical phase followed by abnormal hyperphosphorylated tau in the CSF and PET. Neurodegeneration and even later cognitive decline are firstly observable in the prodromal phase (Leuzy et al. 2019)

1.1.2 Risk factors

The main risk factor for AD is aging, contributing to the sporadic form of AD that represents around 95% of all AD cases (Hendrie 1998; Bird 2005). However, genetic, epigenetic, and environmental factors additionally influence AD occurrence. The inherited familial cases of AD (FAD) carry at least one autosomal dominant mutation in specific genes, leading to a predisposition for AD before reaching the age of 65 (Gatz et al. 2006). Early-onset AD is strongly associated to mutations in the gene for *APP* and the genes for one of the APP processing enzymes, consistent of *PS1* and *PS2* (Goate et al. 1991; Sherrington et al. 1995; van Broeckhoven et al. 1992). Mutations in these genes principally shift the processing of APP to the amyloidogenic pathway, and thereby lead to an elevation of the Aβ peptide, the main component of Aβ plaques (Thordardottir et al. 2017). Moreover, overexpression of normal APP leads to an increased Aβ production in Down syndrome patients as *APP* is located on chromosome 21 and thus, the triplet of this chromosome strongly enriches the predisposition for AD (Head et al. 2018).

Mutations in the gene of a specific *apolipoprotein E* (*APOE*) isoform, the *APOE4* allele, and mutations in the gene for the *triggering receptor expressed on myeloid cells 2* (*TREM2*) are mainly related to the late-onset, sporadic form of AD (Guerreiro et al. 2013; Simpson et al. 2011). However, a twin study showed strong evidence of 60-80% of the sporadic AD cases are linked to hereditary factors as well (Gatz et al. 2006).

Besides genetic factors, vascular disorders are observed as the most frequent risk factor, which were identified as the earliest and strongest predictors of sporadic AD (Iturria-Medina et al. 2016). Additionally, AD predisposition can also be influenced by lifestyle or general health condition of the individual. Several chronic diseases are known comorbidities in AD, and different environmental factors can act as positive or negative contributors on disease onset (Edwards Iii et al. 2019). So far, AD still represents an uncurable disease with no effective treatments in the pipeline. Drug candidates from promising preclinical trials kept failing when tested in AD patients (van Dyck 2018; Mehta et al. 2017). Similar to chronic cardiovascular diseases, modifying life style factors like physical activity showed strong beneficial evidence to prevent or at least to shift AD onset to older ages (Ngandu et al. 2015; Livingston et al. 2017).

1.1.3 AD models and drug therapies

Between the first description of AD and today, research successfully uncovered several cellular mechanisms, processes, molecules, and proteins associated with disease progression. Without the existence and usage of animal models, these advances would be hard to achieve or even impossible. Transgenic mice are commonly used as disease models to better understand AD pathology and to test potential treatment strategies. Increasing knowledge regarding the complex interplay of the neuropathological hallmarks in AD provided the chance to mimic different pathological alterations with transgenic mouse lines. Before the generation of the first transgenic mouse, amyloid β (Aβ) pathology was studied by Aβ peptide administration directly into the mouse brains (Yamada et al. 2005; van Dam und Deyn 2006). PDAPP was the first transgenic mouse line developing Aβ pathology by mutating and overexpressing the human *APP* with a common mutation at the γ-secretase cleavage site that is known to be associated with FAD (Games et al. 1995). Similarly, the next generated transgenic mouse lines, Tg2576 and APP23 also used *APP* as target gene with different common mutations (Hsiao et al. 1996; Calhoun et al. 1999). The formed Aβ plaques showed high structural similarities to Aβ plaques in humans but were not displaying the entire spectrum of AD pathologies, such as missing neuronal loss (Irizarry et al. 1997a; Irizarry et al. 1997b; Calhoun et al. 1998). Further advanced mouse lines were generated with multiple mutations in additional genes linked to FAD (e.g., PS1). These mice featured an elevated earlier accumulation of Aβ42 that is more prone to accumulate (Hall und Roberson 2012). To get closer to mimicking human AD pathology, mice with additional tauopathy were created, exhibiting Aβ plaques, NFTs and neuronal loss (Götz et al. 2004). Currently, a variety of AD mouse lines are commercially available, stressing specific pathological features of AD and are invaluable to study mechanisms altered in an AD context. Despite their significance for mechanistic studies and testing of potential drug targets, the available mouse models do not reflect the entire complexity of AD pathology. This may be the reason that no functional or beneficial drugs have been successfully discovered yet.

The current gold standard therapy in the clinic is a combination with cholinesterase inhibitors and a N-methyl-D-aspartate receptor (NMDAR) antagonist that modifies the cholinergic and glutamatergic metabolism. This treatment improves the cognition, memory and orientation, but is only a symptomatic and not a causal treatment (Campos et al. 2016). The first promising trial in mice was the immunization against Aβ peptides that reduced the disease progression in PDAPP mice (Schenk et al. 1999). Ever since, various monoclonal antibodies showed the ability to bind and clear Aβ in several mouse models but not in humans (van Dyck 2018; Wisniewski und Konietzko 2008). Developed β-secretase inhibitors showed promising effects in animal models by reducing the Aβ peptide (May et al. 2015; Kennedy et al. 2016). Unfortunately, these inhibitors failed proving efficacy in clinical trials in humans and were often accompanied by side effects (Cao

et al. 2018). Manipulating the activity of the γ-secretase was even more challenging due to the lack of target selectivity (Dovey et al. 2001; Lanz et al. 2010). However, there are still ongoing clinical trials with next generation secretase inhibitors (Figure 1-4) (Cummings et al. 2019).

Similarly, AD-associated tau pathology generated several promising treatment targets, including the inhibition of intracellular tau aggregates, prevention of hyperphosphorylation, induction of clearance or reduction of tau spread (Panza et al. 2016). Like for Aβ, targeting tau pathology was mainly unsuccessful thus far despite the better correlation of tau pathology with cognitive impairments compared to Aβ plaque progression (Cao et al. 2018).

One reason for the lack of efficacy of identified therapeutic targets in humans is presumably the usage of mice representing an early onset FAD pathology instead of the more common form of sporadic late onset AD (King 2018). Therefore, mouse lines were generated by inserting the known sporadic late onset risk factor genes, as *APOE4* and/or *TREM2* with and without additional Aβ pathology (Raffai et al. 2001; Murray et al. 2019). APOE4 has been demonstrated to be of high relevance in clinical trials resulting in significant differences between *APOE4* carriers compared to non-carriers when treating with the anti-Aβ monoclonal antibody Bapineuzumab (Salloway et al. 2014). Other strategies are focused on neuroprotection by reducing neuroinflammation and oxidative stress or by inducing beneficial signalling pathways (Cao et al. 2018).

Due to the complexity of known and unknown factors that cause AD, it is so far nearly impossible to consider all factors in the therapeutic treatment of AD. Usual challenges including blood brain barrier permeability and drug specification additionally complicate the development of new treatment strategies (Huang 2011). Besides, the lack of appropriate biomarkers makes early AD detection difficult, thus most clinical trials are performed with patients in a late stage of AD although treatment strategies would mainly convey beneficial effects to patients in the pre-symptomatic stage (Cao et al. 2018; Cummings et al. 2019). Figure 1-4 illustrates promising treatment strategies that were in phase III clinical trials in 2019, comprising drugs targeting symptoms and a broad spectrum of drugs related to disease-modifying therapies, which are still targeting the major hallmarks of AD. (Cummings et al. 2019). Overall, a growing community of AD researchers, an increasing number of identified molecular mechanisms, new hits for drug targets and newly discovered biomarkers give rise for optimism to determine a better treatment strategy for AD in the future.

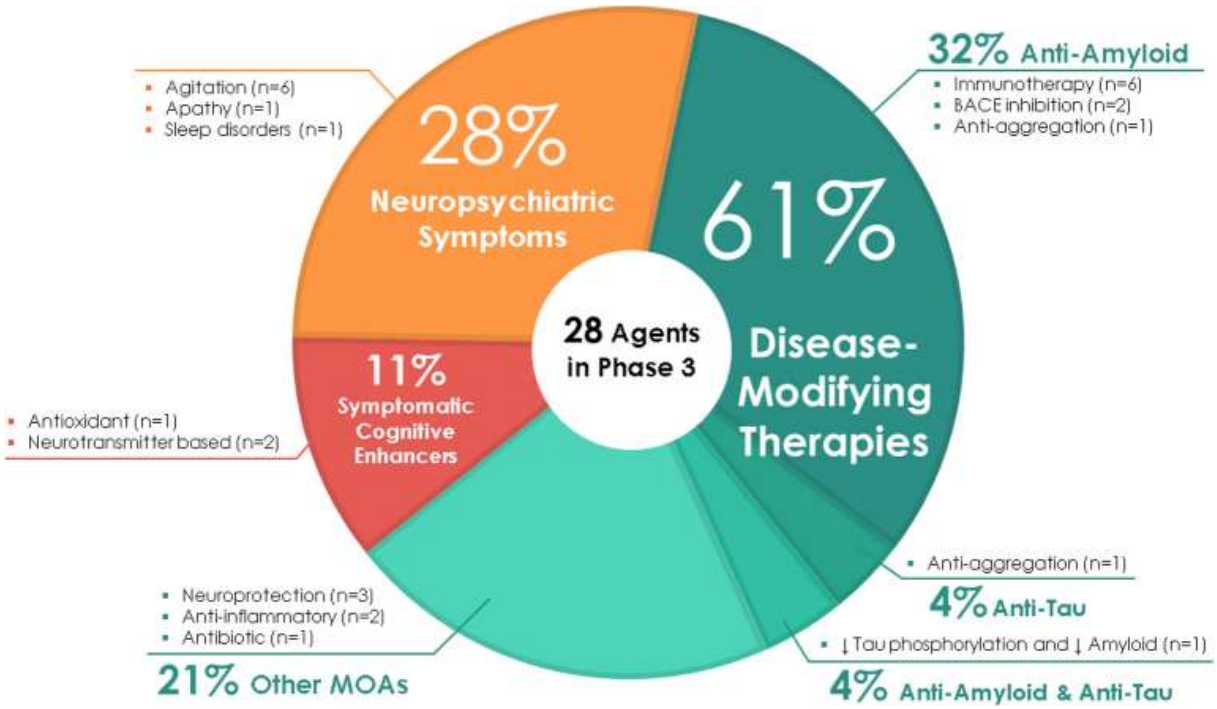

Figure 1-4 Mechanism of action of treatment strategies in phase3 from 2019 (Cummings et al. 2019).

1.2 Astrocytes

As R. Douglas Fields exemplified in his book "*The other brain",* glial cells were historically underestimated in neuroscience. Nowadays, it seems to be obvious that glial cells that represent 85 % of all brain cells need to be included into almost every neuroscientific question. The term glia (from the Greek word for "*glue"*) compromise cell types such as astrocytes, oligodendrocytes, and microglia. In the past decades, the field is increasingly focussing on glial cells based on the assumption that glial cells may have more essential functions in the brain besides of the characterization as being just the "glue" (Somjen 1988).

Astrocytes represent with around 20-40 % the most abundant cell type in the mammalian central nervous system (CNS). This abundance is dependent on the species and on the brain region. Overall, astrocytes display an extremely heterogenous cell population throughout and within the different brain regions (Lanjakornsiripan et al. 2018; Sofroniew und Vinters 2010; Khakh und Sofroniew 2015). Two main sub-classes distinguishable by specific morphology features are represented by the protoplasmic astrocytes in the grey matter and the fibrous astrocytes in the white matter. A uniform "bushy" morphology with high arborization of fine processes originating from thick main branches that ensheath synapses are characteristics for protoplasmic astrocytes, whereas fibrous astrocytes present long fibre-like processes that contact neurons through myelin-sheath gaps (Lundgaard et al. 2014). In addition, both types of astrocytes are connected to blood vessels and to other astrocytes via gap junctions generating large astrocytic networks throughout the brain (Sofroniew und Vinters 2010; The Fine Structure of the Nervous System. Neurons and their Supporting Cells. 3rd edition 1991) (Khakh und Sofroniew 2015; Herculano-Houzel 2014; Barres 2008). Such morphological complexity presents an invaluable number of interactions with other cell types, including neuronal synapses. Thus, astrocytes play an essential role in regulating blood brain barrier (BBB) function, metabolic homeostasis, ion and NT homeostasis, neurovascular coupling, and synapse formation, elimination and synaptic transmission (Khakh und Sofroniew 2015; Burda und Sofroniew 2014).

1.2.1 The tripartite synapse

Astrocytes with their unique bushy cell structure are organized in a non-overlapping network. The highly ramified structure of their fine processes enables their fine-tuned interplay with synapses (Bushong et al. 2002; Witcher et al. 2010). One cortical protoplasmic astrocyte in a mouse brain has around 100,000 synaptic interactions, whereas a human astrocyte has around 2,000,000 synaptic contacts, highlighting the relevance of astrocytes for neuronal functions. The interconnection between neuronal pre- and post-synapses and the fine peri-synaptic processes are known as the tripartite synapse (Figure 2-5) (Allen und Eroglu 2017). Formation of the tripartite synapse is a very dynamic process and dependent on existing conditions like neuronal activity, developmental state, physiological condition and disease context (Bernardinelli et al. 2014; Genoud et al. 2006). Electron microscopy images revealed the ensheathment of synapses by the fine peri-synaptic processes of astrocytes (Witcher et al. 2007). Due to the finely-tuned connectivity between astrocytes and pre- and post-synapses characterized by the expression of specific receptors, channels, and transporters, neuronal action potentials (APs) induce apparent astrocytic responses (Heller und Rusakov 2015). Figure 1-5 exemplifies a tripartite synapse and its responses. Here, an AP firing neuron releases NTs at its pre-synaptic terminal into the synaptic cleft. Subsequently, NTs bind to its ionotropic channels (NT receptor) at the post-synapse and at receptors located at the astrocytic processes that in turn, lead to an activation of the neuron and additional Ca^{2+} influx in the astrocyte. Furthermore, the NT act as a ligand for a GPCR on astrocytic peri-synaptic processes. Upon ligand binding, the conformational change of the receptor leads to the release of the G-protein. In the case of a Gq-protein release, intracellular phospholipase C is activated and produces the messenger molecule inositol-1,4,5-trisphosphate (IP_3) with subsequent activation of the IP_3 receptors (IP_3R) located in the endoplasmic reticulum (ER) (Foskett et al. 2007; Bazargani und Attwell 2017; Tanaka et al. 2013). Such IP_3R activation induces Ca^{2+} release from the ER, resulting in the activation of different other signalling cascades, including gliotransmitter (GT) secretion through vesicles or respective transporters (Montana et al. 2006). Consequently, GTs influence synaptic transmission and modulate neural plasticity via GT receptor activation on the neuronal terminals (Araque et al. 2014). Furthermore, due to this astrocytic response to neuronal activity, astrocytes further transmit this information to other cells via gap junctions (Bazargani und Attwell 2017). Considering this complex interplay between astrocytes and synapses, it is not surprising that disturbances within this system are associated to several CNS disorders (Halassa et al. 2007; Rudy et al. 2015).

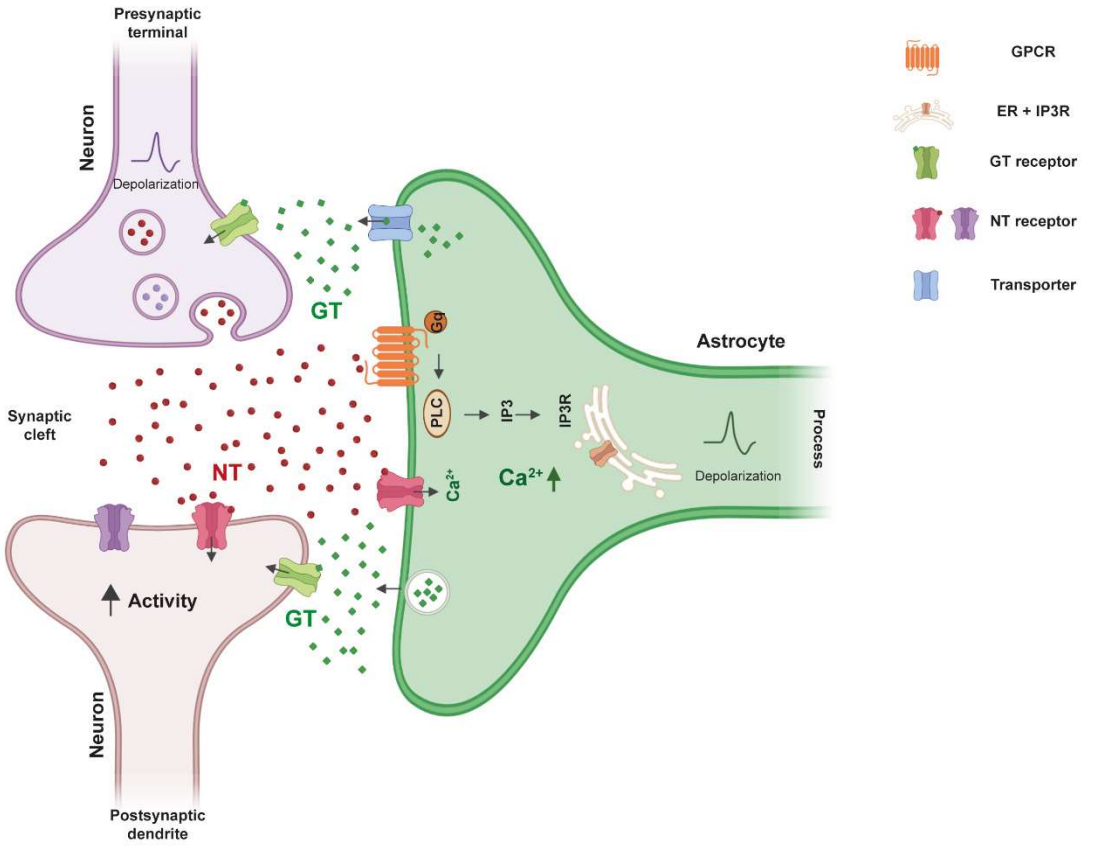

Figure 1-5 Schematic illustration of the neuron-astrocyte communication through the tripartite synapse. Neurotransmitter (NT, red) release on the presynaptic terminal (purple) is triggered by neuronal depolarization and leads to the activation of the postsynaptic neuron by NT binding on its NT receptors on the postsynaptic dendrite (pink). NTs bind to the Gq-protein coupled receptor (GPCR) on astrocyte processes (green), which activates the downstream signalling cascade though phospholipase C (PLC) that leads to an inositol-1,4,5-trisphosphate (IP_3) mediated intracellular Ca^{2+} elevation by the activation of the IP_3 receptors (IP_3R) on the endoplasmic reticulum (ER). Activation of NT receptors on the astrocytic process results in an additional Ca^{2+} influx from the extracellular space. Astrocytic Ca^{2+} elevation results in gliotransmitter (GT, green) release by exocytosis or through specific transmembrane transporters. Subsequent activation of GT receptors on the pre-and postsynaptic terminals influencing synaptic transmission.

1.2.2 Calcium signalling in astrocytes

Astrocytes are not electrically excitable, implying that intracellular Ca^{2+} elevation is not inducing membrane depolarisation. Hence, astrocytes do not "fire" action potentials like neurons do. However, astrocytic Ca^{2+} dynamics play a crucial role in numerous mechanisms, such as transcriptional regulation, gliotransmitter (GT) secretion and neurovascular coupling (Petzold und Murthy 2011; Verkhratsky et al. 2016; Papouin et al. 2017). Astrocytic Ca^{2+} elevations can occur either spontaneously or as response to received triggers (Khakh und Sofroniew 2015; Araque et al. 2014; Chai et al. 2017; Guerra-Gomes et al. 2017). In general, Ca^{2+} elevations are amplified by the release from intracellular Ca^{2+} stores or by influx through specialized channels from the extracellular space. The evoked Ca^{2+} signals are triggered by NTs such as norepinephrine, ATP, Glutamate, GABA, acetylcholine (ACh), nitric oxide, and endocannabinoids that are released from neurons (Guerra-Gomes et al. 2017; Halassa und Haydon 2010). Dependent on the involved NT type, astrocytic Ca^{2+} dynamics have a direct impact on synaptic plasticity and on neuronal circuits. The functional output for cellular Ca^{2} increase is the GT release that in turn, affects actions in other glia, neurons, and endothelial cells in a spatiotemporal dependency. GT secretion is mediated by diffusion through plasmalemmal channels, active translocation by transporters or regulated exocytosis (Figure 6) (Verkhratsky et al. 2016; Guerra-Gomes et al. 2017). The release via exocytosis is highly dependent on spatiotemporal Ca^{2+} concentrations and the formation of the soluble N-ethylmaleimide-sensitive fusion protein attachment protein receptor (SNARE) complex (Verkhratsky et al. 2016; Zhang et al. 2004).

Due to their morphological complexity and their physical contacts to various cell types, astrocytes exhibit high diversity of functional inputs from the environment (Khakh und Sofroniew 2015; Bindocci et al. 2017). Technical advancements such as fluorescent life-time imaging microscopy (FLIM), two-photon laser scanning microscopy (2PLSM) and the usage of fluorescent Ca^{2+}indicators enabled the visualisation of cellular Ca^{2+} dynamics in astrocyte cultures and living animals. Genetically encoded Ca^{2+} indicators (GECIs), such as GCaMP, further advanced the recordings of Ca^{2+} transients and revealed astrocytic Ca^{2+}dynamics as spatially and temporally extremely complex and diverse (Bindocci et al. 2017; Shigetomi et al. 2016; Kanemaru et al. 2014; Volterra et al. 2014).

Moreover, astrocytes show characteristic types of Ca^{2+} signals in the soma, branches, processes and their endfeet (Stobart et al. 2018b). Spontaneous Ca^{2+} signals occur without action potential firing in neurons and are localized to so called microdomains that are small active regions in branches or the finer processes and endfeet. However, dependent on the brain region, microdomains are also activated by neuronal activity (Shigetomi et al. 2013; Di Castro et al. 2011). Another characteristic Ca^{2+} signal type in astrocytes is the wave-like Ca^{2+} transient that covers astrocytic soma and the large branches and can occur in an extensive global Ca^{2+} rise spread

through the entire astrocyte. These Ca^{2+} waves are reduced when deleting astrocyte-specific IP_3R type2, highlighting the dependency on GPCR-mediated Ca^{2+} release (Haustein et al. 2014; Srinivasan et al. 2015). In addition to IP_3R-mediated Ca^{2+} signals, Ca^{2+} transients in endfeet are also dependent on Ca^{2+} entry via Transient Receptor Potential Cation Channel Subfamily V (TRPV4) (Dunn et al. 2013; Straub et al. 2006). Ca^{2+} response to behaviour such as locomotion appear as network-like signals that cover many astrocytes in parallel, as opposed to single-astrocyte signals described above, and are known to be triggered by neuronal NT release (Ding et al. 2013; Paukert et al. 2014). Intracellular Ca^{2+} release is not restricted to the ER, other cell organelles such as mitochondria, Golgi, and acidic organelles are known to express specific proteins that are involved in intracellular Ca^{2+} increases (Patel und Docampo 2010; Hill et al. 2014; Agarwal et al. 2017).

1.2.3 Astrocytic modulation of neural circuits

Astrocytes critically impact the activity of neurons, highlighting their contribution to neural circuits. Neurons comprise a remarkably diverse cell population that releases characteristic NTs dependent on the type of neurons in the specific neural circuit and microcircuit, respectively. Neural circuits describe primarily interconnections from specialized neurons in specific brain regions linked to a distinct functions (Khakh und Sofroniew 2015). Due to the apparent astrocyte involvement in the tripartite synapse, astrocytes are able to modulate local neural circuits, networks and thereby behaviour (Araque et al. 2014; Srinivasan et al. 2015; Paukert et al. 2014; Poskanzer und Yuste 2016). Like neurons, astrocytes secrete a specific spectrum of transmitters that are capable of modulating synaptic plasticity, homeostatic plasticity, stimulation or inhibition of synaptic transmission, long-term potentiation (LTP) or long-term depression (LTD) (Halassa und Haydon 2010; Perea und Araque 2005; Henneberger und Rusakov 2010).

1.2.4 Cortical astrocyte responses in an awake behavioural state

Astrocytes have recently been shown to specifically respond to neuronally released ACh and norepinephrine (NE) in different behavioural paradigms (McGinley et al. 2015). It has been demonstrated by pharmacological blockage of their receptors that ACh and NE release are strongly associated with neuronal activity modulation in the cortex, specifically in an arousal or heightened vigilance state (Paukert et al. 2014; Schiemann et al. 2015; Fu et al. 2014b). The arousal state is studied by inducing response upon whisker stimulation, foot shock or mechanical stimulation in slightly anesthetized mice or by an enforced locomotion in awake mice (Khakh und Sofroniew 2015). ACh is released from neuronal projections originated from different nuclei in the brainstem and the basal forebrain, the nucleus basalis (Eggermann et al. 2014). *In vivo* and *ex vivo* stimulations of the nucleus basalis resulted in a pronounced Ca^{2+} elevation in cortical astrocytes that was absent when metabotropic cholinergic muscarinic receptors (mAChRs) were blocked (Chen et al. 2012; Takata et al. 2011).

In addition, the locus coeruleus (LC) is a small nucleus located in the brainstem that sends its noradrenergic projections throughout the brain, making the LC the exclusive source of NE in the brain (Aston-Jones und Cohen 2005). Similarly to the ACh system, it has been observed that activation of the LC by either optogenetic or arousal-induced stimulation leads to a strong and broad Ca^{2+} elevation in cortical astrocytes (Ding et al. 2013; Bekar et al. 2008; Oe et al. 2020b). Astrocytes in the cortex express α1-ARs that mediate Ca^{2+} release through the IP_3 pathway, which can be inhibited by treatment with α1-AR antagonists or by depletion of LC neurons (Shigetomi et al. 2016; Ding et al. 2013). Taken together, both, the ACh and the NE system play an important role in astrocytic activation during arousal and vigilance and hence, in a global brain state (Kjaerby et al. 2017), highlighting the potential significance of astrocytes as modulators of neural circuits and behaviour.

1.3 Astrocytes in the context of aging and AD

Considering the enormous range of functions, the high abundance, and the heterogeneity of astrocytes, it is not surprising that this cell type undergoes drastic alterations upon pathological stimuli such as stroke, neurodegenerative diseases, tumours, trauma, infection, and aging. Astrocytes react insult-dependent with alterations in their gene expression profile, resulting in distinct morphological, molecular, and functional changes.

The phenotypic transformation of astrocytes is known as reactive astrogliosis (Matias et al. 2019). This phenomenon should not be considered as one specific change; it can differ in outcome dependent on many different aspects. To date, the role of reactive astrogliosis is unclear and debated as either being beneficial or detrimental to the surrounding (Sofroniew 2009; Pekny et al. 2014). The categorization of defined reactive phenotypes describing a neurotoxic or a neuroprotective astrocyte is highly controversial. In addition to the heterogeneity of nonreactive astrocytes, reactive astrocytes add further complexity to this particular cell type as they are molecularly and functionally diverse. On the one hand, reactive astrocytes secrete anti-inflammatory factors, leading to beneficial protective and potentially regenerative effects. On the other hand, astrocytes can also produce neurotoxic factors (Liddelow et al. 2017). Already Alois Alzheimer observed large bundles of filaments in glial cells especially in those in close proximity to the senile plaques (Alzheimer 1911). Today, these bundles are known to consist of accumulated glial fibrillary acidic protein (GFAP) filaments, which is the best-known marker gene that characterized reactive astrocytes (Wegiel und Wisniewski 1994). Increased expression of this cytoskeletal protein leads to a pronounced visible fibrillary structure in reactive astrocytes that varies in degree dependent on the specific insult (Escartin et al. 2019). Increased astrocyte reactivity represents a hallmark of physiological aging although the changes in morphology and function are strongly dependent on the brain region. Interestingly, reactive astrocytes in aged brains are similarly distributed to brain regions like reactive astrocytes in neurodegenerative diseases (Rodríguez et al. 2014). From a purely morphological view, astrocytes change their morphology from long, highly ramified processes to smaller cells with reduced complexity of their branches during ageing in humans, primates, and rodents (Jyothi et al. 2015; Castiglioni et al. 1991; Robillard et al. 2016).

Additionally, astrocytes shift their gene expression to a mild inflammatory state in response to normal aging (Rea et al. 2018; Clarke et al. 2018). The complement system as part of the innate immune system is known to play a key role in aged astrocytes as well as in astrocytes in diseases, including AD. Higher complement cascade activation results in increased synaptic pruning from astrocytes, leading to synapse and dendrite loss. Thereby, the enhanced activation of the complement system is considered as essential contributor to synapse elimination in aging and AD pathology (Boisvert et al. 2018). Age and age-related neurodegenerative diseases also

induce several other alterations in astrocytes such as an increased oxidative stress response and dysregulation of cholesterol synthesis (Boisvert et al. 2018).

Interestingly, the astrocytic functional response to neuronal activity characterized by intracellular Ca^{2+} elevation seems to be highly conserved during aging (Gómez-Gonzalo et al. 2017; Palygin et al. 2010). In AD mouse models, however, astrocytes showed increased activity in different brain regions and under several experimental conditions. Here, the increased frequency of Ca^{2+} signals is characterizing a fraction of astrocytes, especially these in close proximity to Aβ plaques, as hyperactive. Thus, enhanced Ca^{2+} signalling promotes further gliotransmitter release and thereby impacting synaptic transmission and neuronal activity. Such altered astrocytic Ca^{2+} response in AD mouse models indicates a disease-related astrocytic network dysfunction and points towards new possible treatment strategies targeting astrocyte-specific signalling pathways with relevance to AD pathology (Kuchibhotla et al. 2009; Delekate et al. 2014; Reichenbach et al. 2018; Pirttimaki et al. 2013).

1.4 Aim of the study

It is essential to gain a better understanding of the role of astrocytes in physiological and pathological mechanisms involved in aging and age-related neurodegenerative diseases such as AD. Astrocytes are extremely complex and multifunctional cells that may represent potential targets for novel treatment options in AD, as they are relevant on transcriptional, molecular, and functional levels in the context of AD. However, the altered mechanisms in astrocytes during AD pathology are still largely incomplete. Therefore, the overarching goal of this study was to investigate astrocytic alterations on a transcriptional and functional level in the context of AD. By investigating the astrocytic translatome during normal aging and in an AD mouse model during Aβ pathology progression, I firstly aimed to uncover changes in astrocyte-specific mechanisms. Secondly, I set out to identify functional alterations by measuring and analysing Ca^{2+} signals in cortical astrocytes in an AD mouse model under minimally invasive conditions and in the awake state. Finally, I aimed to interconnect findings from these translatome studies and functional assessments to identify potentially relevant mechanisms in cortical astrocytes during AD.

2 Results

2.1 Studying translational astrocytic changes during aging and Aβ pathology progression

In order to study translational changes in astrocytes during aging, the Cx43^{CreERT2}/RiboTag mouse line (Sanz et al. 2009) was utilized, which allows for immunoprecipitation of astrocyte-specific mRNA from brain tissue homogenate. In addition, crossing Cx43^{CreERT2}/RiboTag mice with APP/PS1 mice permitted the investigation of alterations in the astrocytic translatome during Aβ pathology progression. The AD mouse used here expresses the human gene for *APP* and the *PS1* with specific AD-causing mutations under the control of the prion protein promoter (Prp), facilitating an expression in all brain cells. The produced mutant proteins are correlated to the early-onset inherited form of AD and induce a progressive amyloidosis at the age of around 6 months in these mice (Jankowsky et al. 2001).

In the utilized mouse model, the promoter for the astrocyte-specific connexin 43 (Cx43) protein facilitates a cell-type specific Cre recombinase expression. The Cx43^{CreERT2}/RiboTag mice, are thereby referred to display the wild type condition, and the Cx43^{CreERT2}/RiboTag x APP/PS1 an Aβ pathological condition (APP/PS1). Moreover, the gene locus of the ribosomal protein L22 (*rpl22*) has a floxed (flanked with loxP sites) exon4 followed by an exon4 with three copies of the hemagglutinin (HA) epitope. Upon Cre activation with tamoxifen, the expressed rpl22^{HA} is incorporated into the actively translating polysomes. The resulting HA-tagged polysomes enable an astrocyte-specific mRNA extraction and immunoprecipitation from brain homogenates, followed by RNA sequencing analysis (Figure 2-1A).

The successful recombination after tamoxifen injection of the target vector was verified by immunohistochemical staining of the rpl22^{HA} protein in brain slices. To identify the cell specificity, I performed a counterstaining for an astrocyte-specific transcription factor, Sox9. As illustrated in Figure 2-1B, Sox9 immunoreactivity clearly identifies astrocytic nuclei while HA expression occurred in the astrocytic cytosol. Most of the Sox9 positive cells were additionally positive for HA (indicated by the white arrows), demonstrating astrocyte-specific Cre recombination. However, the presence of Sox9 single positive cells indicates that the recombination was not induced in all astrocytes (Figure 2-1B).

To further verify the cell-specificity of the RiboTag procedure, normalized gene expression analysis revealed a highly enriched expression profile of astrocyte marker genes *Kcnj10, Slc1a2 and Gja1* in the RiboTag samples, whereas marker genes for neurons (*Rbfox3, Nefl, Tubbb3*), oligodendrocytes (*Mog, Sox10, Gjc2*) or microglia (*Cd68, Ccl3, Tnf*) were absent (Figure 2-1C).

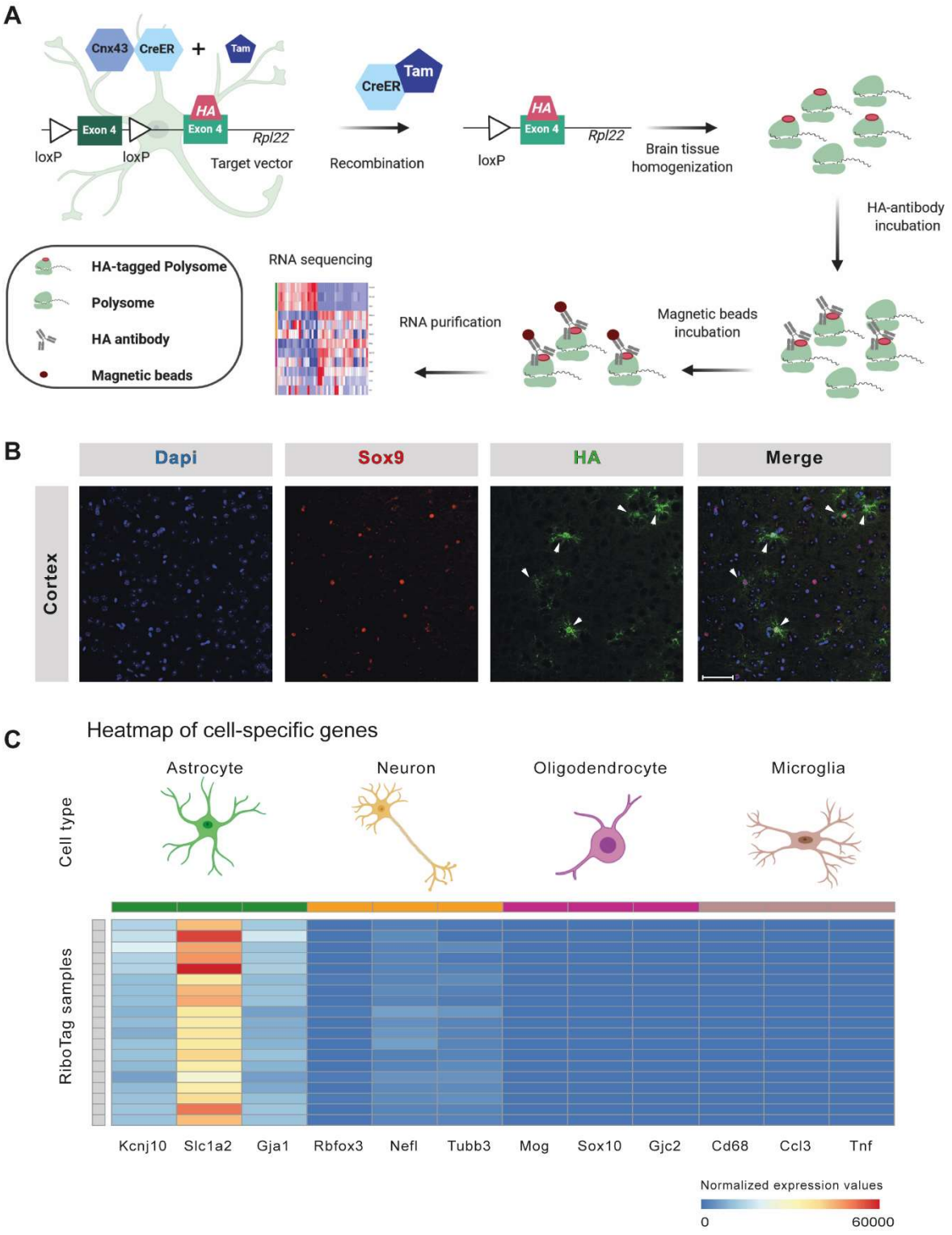

Figure 2-1 RiboTag approach and specificity. (A) Astrocyte-specific Cre expression was induced by tamoxifen injections of Cx43^{CreERT}/RiboTag mice. Activated Cre removes the endogenous exon4 of the *rpl22* target vector, resulting in a recombinant HA-tagged rpl22 protein, that tags, by incorporation into the ribosomal subunit, all astrocytic polysomes. After brain homogenization tagged polysomes (ribosomes + mRNA) are labelled with anti-HA antibodies followed by a pull-down using magnetic beads. Subsequently isolated mRNA was analysed by RNA sequencing. (B) Immunohistological staining with an anti-HA antibody demonstrated astrocyte-specific HA expression by using anti-Sox9 antibody to label astrocytic nuclei. Arrows indicate HA and Sox9 co-expressing cells. Scale bar = 50 µm. (C) Heatmap of normalized expression values of specific cell marker genes show an enrichment of astrocyte (green) specific marker genes (*Kcnj10, Slc1a2, Gja1*) while lacking the marker genes for neurons (yellow), oligodendrocytes (purple) and microglia (brown).

During aging or in the context of a neurodegenerative disease, such as AD, astrocytes change their gene expression profile (Nichols et al. 1993; Rodríguez et al. 2014; Simpson et al. 2011). To better understand the changes in astrocytes during normal aging and the potentially altered astrocytic gene expression during Aβ pathology progression, brains of wild type mice and APP/PS1 mice at different age ranges were investigated. In the herein used AD model, APP/PS1 mice with an age of 4 months (young) represent a timepoint before disease onset, while 8 months (middle-aged) and 12 months (old) old APP/PS1 mice represent the early stage and the late stage of Aβ pathology, respectively (Figure 2-2A).

RNA sequencing was performed with all generated samples, including RNA samples from all cell types of the brain (total mRNA) and the immunoprecipitated astrocytic mRNA (RiboTag mRNA). Initially, an exploratory data analysis was performed to understand the overall differences in gene expression between astrocyte (RiboTag) samples and all brain cells (total mRNA) of all present genes. The data was batch corrected and visualized in a principle component analysis (PCA) that summarizes the expression features of each sample. The PCA showed a clear separation of the two sample types along the direction of largest variance of data (first principle component; PC1), illustrating that there are features that are distinctly different between the two groups. Hence, total mRNA samples showed a dense cluster, demonstrating a high similarity of their gene profile, while the RiboTag samples cluster into the other direction in a more spread-out manner, indicating higher gene expression variabilities within the RiboTag samples (Figure 2-2B).

In order to understand astrocyte-specific differences between the groups with higher resolution, the RiboTag samples were further analysed in greater detail. After normalization, PCA was performed, which showed a clear separation of middle-aged APP/PS1 from old APP/PS1, whereas young APP/PS1 mice clustered between these groups (Figure 2-2C). A similar pattern emerged in young, middle-aged, and old wild type mice (Figure 2-2C). Interestingly, when comparing APP/PS1 with wild type cohorts, old wild type mice showed a tendency towards old APP/PS1 mice, while young and middle-aged wild type and young and middle-aged APP/PS1 mice were clearly separated (Figure 2-2C).

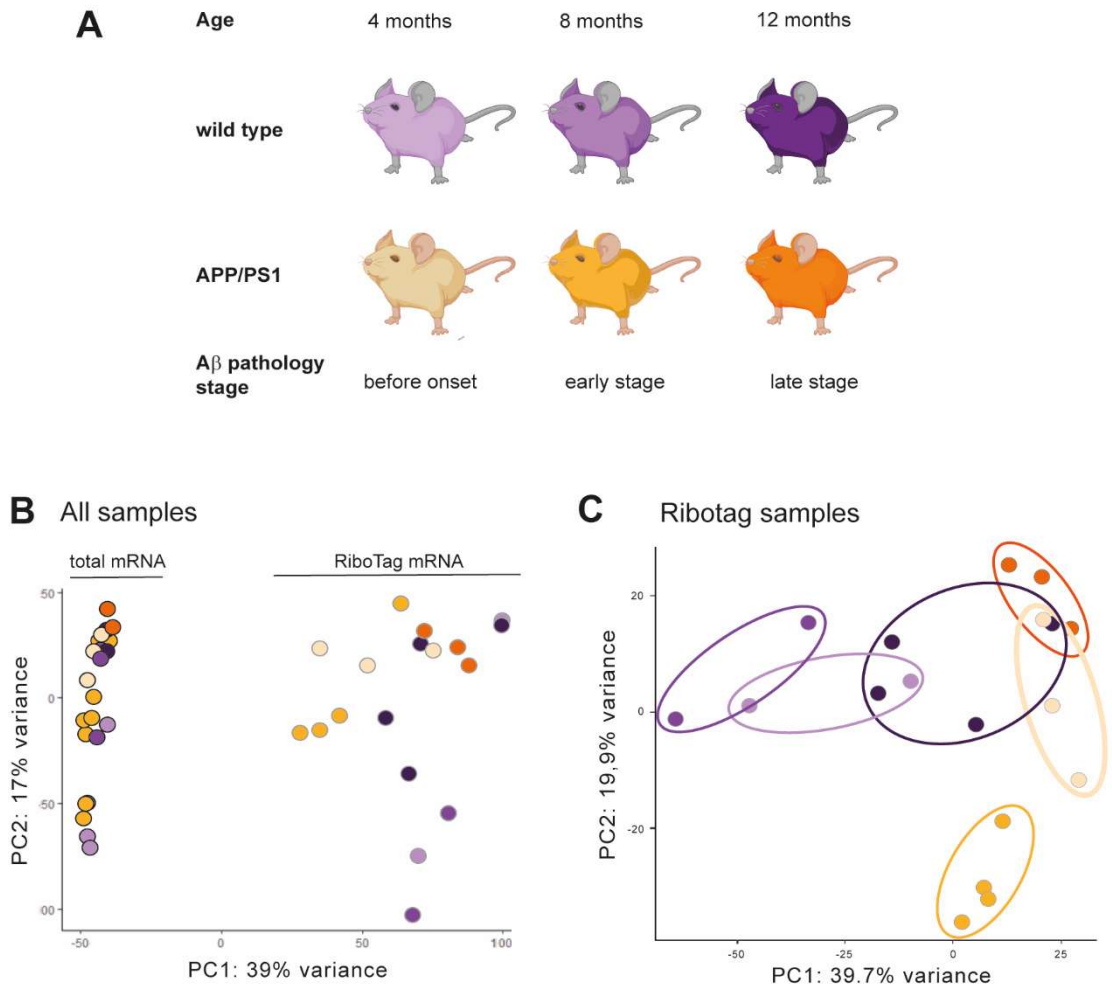

Figure 2-2 Experimental setup and exploratory data analysis. (A) Illustration of the experimental setting of the RiboTag approach using two different groups, wild type (violets) and APP/PS1 (oranges) mice. Each group consists of 4 months, 8 months, and 12 months old mice to mimic Aβ pathology progression in the APP/PS1 mice, before onset, early and late stage. (B) Principle component analysis (PCA) in 45 samples, consisting of total mRNA and RiboTag mRNA, illustrate gene expression differences of the total mRNA sample (left) with a clear separation from RiboTag mRNA samples, which do not form one distinct cluster. (C) PCA from RiboTag mRNA samples showed a similar orientation of the APP/PS1 group from all cohorts, along the PC1 axis, whereas the wild type samples were more spread and separate, except from 12 months old cohort, which showed a tendency towards APP/PS1 old mice (sample orientation of each condition is indicated by boundaries with condition corresponding colours); n = 2-4 mice

Next, differential gene expression was tested using the FDR-adjusted p-value < 0.05, which resulted in 1,665 upregulated (red) and 1,294 downregulated (blue) genes in all APP/PS1 mice compared to wild type mice. The highest number of differentially expressed genes (DEGs), with 1,337 up and 1,228 downregulated genes, we identified in the comparison between middle-aged APP/PS1 mice and middle-aged wild type mice. In contrast, the old APP/PS1 vs. wild type mice showed the lowest number of DEGs (34 up- and 14 downregulated genes: Figure 2-3A).

I also compared DEGs between the two mouse lines which were up- or downregulated during aging. We found low numbers of DEGs when comparing 8 months vs. 4 months old mice (wild type: 4 up- and 8 downregulated genes; APP/PS1: 24 up- and 207 downregulated), where only one shared DEG was upregulated in both groups (Figure 2-3A, Venn diagram). In contrast, we observed a high number of DEGs that were shared when comparing the expression in the old cohort (12 months) to the middle-aged mice (8 months) of both mouse lines (98 up- and

5 downregulated DEGs; Figure 2-3A, Venn diagram). Comparing DEGs in APP/PS1 mice vs. wild type mice, there is a strong overlap in the up- and downregulated genes from the 4 months old and 8 months old cohort (Figure 2-3B, C).

Taken together, the DEG analysis revealed a pronounced gene expression change in the stage before disease onset which shows a strong overlap with the gene expression change in the stage of the early onset stage for Aβ pathology. Furthermore, we detected the highest gene expression variability between middle-aged and old mice for both mouse lines.

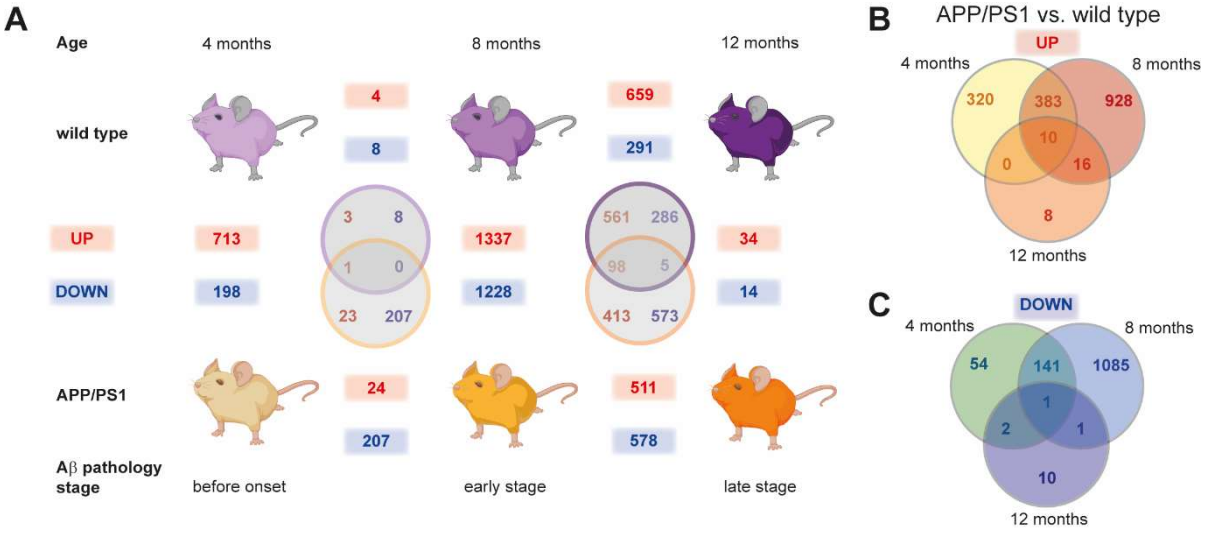

Figure 2-3 Differential genes expression analysis. (A) Up (red) and downregulated (blue) genes between the different age cohorts and the changes in APP/PS1 (oranges) vs. wild type (violets) mice. Overlap in the Venn diagrams illustrates identical regulated genes in both groups in the age matched comparison. (B) Overlap of upregulated genes in all three age cohorts of APP/PS1 vs. wild type mice. (C) Overlap of downregulated genes in all three age cohorts of APP/PS1 vs. wild type mice. Genes were defined with an FDR-adjusted p-value <0.05; n= 2-4 mice

2.1.1 Astrocyte gene expression changes with age in wild type and APP/PS1 mice

To gain insight into the main changes of gene expression changes related to normal aging, we performed a gene set enrichment analysis (GSEA) to detect gene clusters for specific biological terms, using gene ontology (GO) or Kyoto Encyclopedia of Genes and Genomes (KEGG) as database resources. GO enrichment analysis of the DEGs upregulated in aged wild type mice showed two distinct enrichments, both of which related to synapses, synapse organization and regulation of synaptic plasticity (Figure 2-4A). Whereas the heatmap of DEGs involved in synapse organization showed an upregulation in old wild type mice, the same genes were even higher upregulated in young and middle-aged APP/PS1 mice (Figure 2-4B). Studying this gene set in more detail by generating a gene interaction network uncovered two sub-clusters (Figure 2-4C). Genes appearing in the axonal guidance term like *Trem2, Grin1, Ephb3, Negf* and *Abl1* are upregulated in old wild type group but upregulated to a greater extent in all APP/PS1 mice.

The other sub-cluster contains genes encoding for neurexins and neuroligins, which as synaptic adhesion molecules and thereby play a crucial role in synaptic transmission and neuronal communication. Genes in this cluster are significantly upregulated during normal aging, while increases are stronger and appear earlier in APP/PS1 mice (Figure 2-4D).

Another interesting group of DEGs related to aging is a group of 98 overlapping genes upregulated in old mice of both groups (Figure 2-3A, Venn diagram). GSEA of this gene set was unsuccessful. Nevertheless, a string network analysis (SNA) identified 20 genes related to metabolism. Mapping this sub-cluster uncovers genes involved in lipid metabolism, like *Cers1* and *Sphk1*. Both genes encode for proteins involved in lipid modification and are thereby involved in the production of lipid based second messengers like sphingosine-1-phosphate (S1P), which is involved in several important cellular processes, including inflammatory signalling and pro-apoptotic pathways (Wit et al. 2019; Fischer et al. 2011). Another gene affecting the regulation of the second messenger ATP in astrocytes is the ectonucleotidase *Entpd2*. By regulating extracellular ATP to ADP transition, Entpd2 is indirectly controlling the activation of purinergic receptors and thereby the activation of astrocytes (Wink et al. 2006). Furthermore, the upregulation of the *Psmb10* (Figure 2-4E), which has been associated to AD before (Orre et al. 2013) may be indicative of astrocyte-associated neuroinflammation during aging as the Psmb10 protein is a subunit of the immunoproteasome that activates upon IFNγ release (Kudriaeva et al. 2017).

Taken together, two main enrichment terms were detected during aging for genes that showed an upregulation in old wild type mice and APP/PS1 mice: genes important for synapse organization and synaptic plasticity during aging in wild type mice, that were remarkably upregulated earlier in APP/PS1 mice. The second group is related to metabolism and metabolic pathways with genes in old mice of both groups.

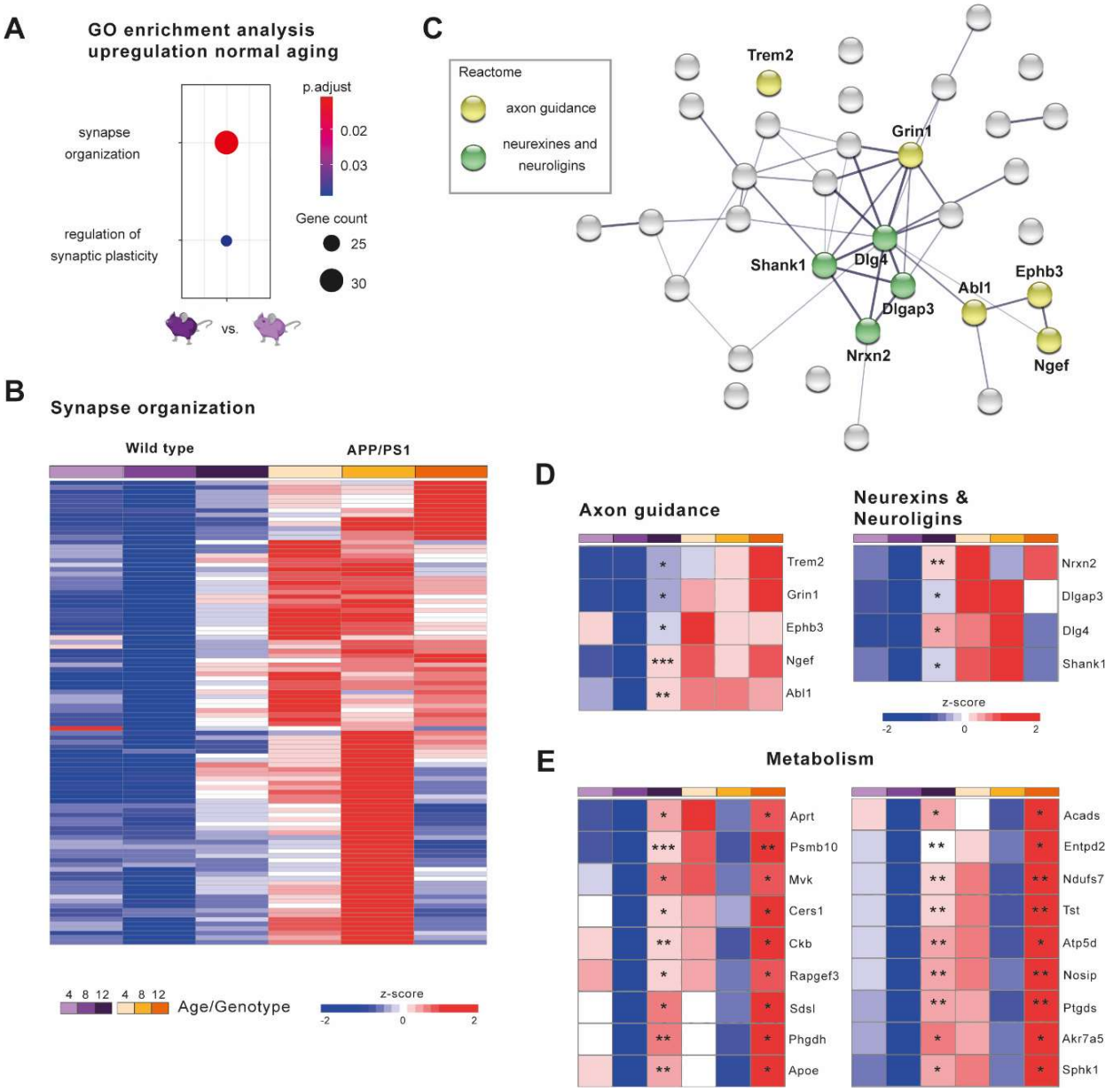

Figure 2-4 GSEA and SNA during normal aging. (A) GO enrichment analysis of DEGs comparing gene expression of old vs. middle-aged wild type mice showed an upregulation of genes involved in synaptic organization and the regulation of synaptic plasticity. Colour scale from red to blue indicates the increasing p-value. Dot size indicating the gene count of the found DEGs in the enrichment term. (B) Heatmap representing mean expression of the 34 DEGs included in the term synaptic organization, demonstrating an upregulation in old wild type mice as well as in APP/PS1 mice. (C) Interactome of the genes corresponding to the heatmap uncovering two sub-clusters with genes associated to axon guidance (yellow bubbles) and genes belonging to neurexins and neuroligins (dark green bubbles) (D) Mean expression heatmap of individual genes from sub-cluster axon guidance and neurexins and neuroligins. (E) 20 DEGs from 98 identified DEGs that were simultaneously upregulated in old mice of both groups. Significance was determined by comparing the expression from 12 months vs. 8 months old mice of the corresponding group. Z-score indicates minimal and maximal z-scaled expression. Bars above the heatmaps indicate the genotype (violets for wild type and oranges for APP/PS1 mice) and colour intensity the age cohorts (young indicated by light colours getting darker with age).

2.1.2 Reactive astrocyte gene expression profiles in response to aging and Aβ pathology progression

Reactive astrocytes show very characteristic features like morphological, molecular and functional alterations (Burda und Sofroniew 2014). In addition to the classification of nonreactive and reactive astrocytes, a specific set of upregulated genes has been defined in reactive astrocytes in all brain pathologies as well as during aging, the so-called pan-reactive marker genes. In addition to this gene set, there are two more classifications of genes that have been proposed as a way to describe the astrocytic phenotype based on its expression profile. These are the so-called neurotoxic or A1 astrocytes and the neuroprotective or A2 astrocytes. Accordingly, the reaction of astrocytes to neuroinflammation (e.g., induced by a lipopolysaccharide (LPS)-treatment) is resulting in an upregulation of genes that may lead to neurotoxicity (A1 phenotype). Neuroprotective astrocytes (A2 phenotype) increase the expression of genes that are typically detected in astrocytes after middle cerebral artery occlusion (MCAO) and have been proposed to be beneficial to neurons (Liddelow et al. 2017; Clarke et al. 2018; Boisvert et al. 2018).

To identify the specific reactive astrocyte phenotype according to this postulated classification in our experimental model, frequently published known gene sets for astrocyte phenotyping were used (Liddelow et al. 2017; Rakers et al. 2019). The expression level of these phenotype-specific genes was visualized in heatmaps. Significances were determined by comparing the expression level in age-matched APP/PS1 and wild type mice (4, 8 and 12 months).

Analysis of pan-reactive marker genes showed that several pan-reactive genes (*Osmr*, *Gfap*, *Hspb1*, *Aspg*) were upregulated in APP/PS1 mice compared to wild type mice (Figure 2-5A). Analysis of A1 vs. A2 phenotypic profiles revealed no clear-cut dichotomy between these gene sets. Specifically, genes associated with the A1 phenotype showed no significant upregulation, although there was a tendency for higher expression of some genes (Figure 2-5B). Likewise, A2-specific genes appeared mostly not regulated except for *Sphk1* and *Cd14* which showed a significant upregulation in young APP/PS1 compared to wild type (Figure 2-5C). None of the A1 or A2 marker genes showed a significant upregulation during normal aging in wild type mice (Figure 2-5A-C). In summary, although this analysis showed an upregulation of some pan-reactive marker genes, the data are not compatible with a clear dichotomy of A1 and A2 astrocytes in APP/PS1 mice.

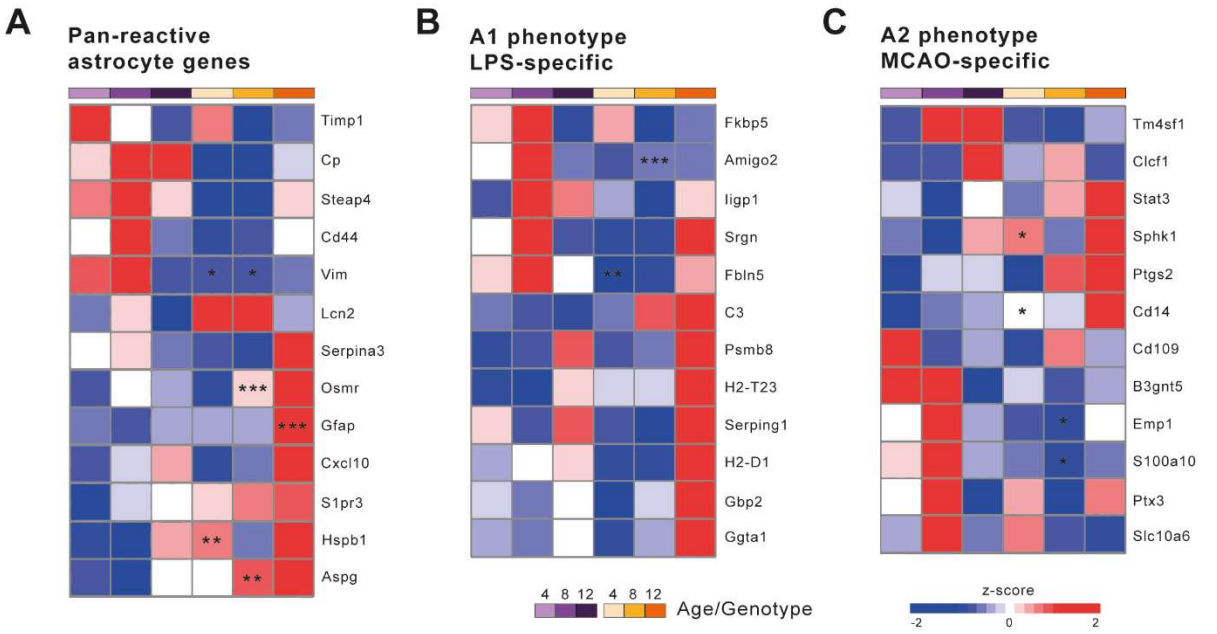

Figure 2-5 Gene expression of marker genes for reactive astrocytes of postulated reactive astrocyte phenotypes. (A) Mean expression heatmaps of 13 genes referred to pan-reactivity, (B) 12 genes to LPS-specific reactivity or A1 phenotypic and (C) MCAO-specific reactivity or A2 phenotypic showed no distinct upregulation related to disease progression or aging for each of the postulated reactive astrocyte phenotypes. In all phenotypes some genes show a tendency to be upregulated in the late stage of Aβ pathology, while for others rather a decreased expression. Only *Osmr* in middle-aged, *Gfap* in old, *Hspb1* in young and *Aspg* in middle-aged were significantly upregulated in APP/PS1 mice. However, *Vim* is significantly downregulated in young and middle-aged APP/PS1 mice in the gene set for pan-reactive genes. For the classified LPS-specific as well as for MCAO-specific *Amido2*, *Fbln5*, *Emp1*, *S100a10* were downregulated in one of the APP/PS1 cohorts compared to wild type, whereas the one significant upregulation was detected in *Sphk1* in young APP/PS1 mice. Significance was determined by comparing the expression from APP/PS1 vs. wild type mice in the different age cohorts

2.1.3 Transcriptional changes in astrocytes induced by progressive Aβ pathology

Next, I performed a GSEA analysis of all upregulated DEGs in APP/PS1 mice To estimate which biological processes or pathways are associated with the genes identified as differentially expressed in APP/PS1 mice during aging, a GSEA of the upregulated DEGs was performed. Here, GO enrichment analysis uncovered that only genes involved in synapse organization were upregulated in all cohorts of APP/PS1 mice, sharing upregulation of some identical genes belonging to the 10 upregulated genes from the overlap in the Venn diagram in Figure 2-2C. Nevertheless, upregulated DEGs from middle-aged and old APP/PS1 mice contribute to more equal terms, where most of them belong to synaptic or axonal regulatory processes. Remarkably, in these cohorts, genes associated to learning or memory and cognition were upregulated. Similarly, enriched genes from the middle-aged APP/PS1 mice were mainly related to synaptic terms, whereas the old cohort contained terms associated with glial activation, glial development, and immune responses (Figure 2-6A).

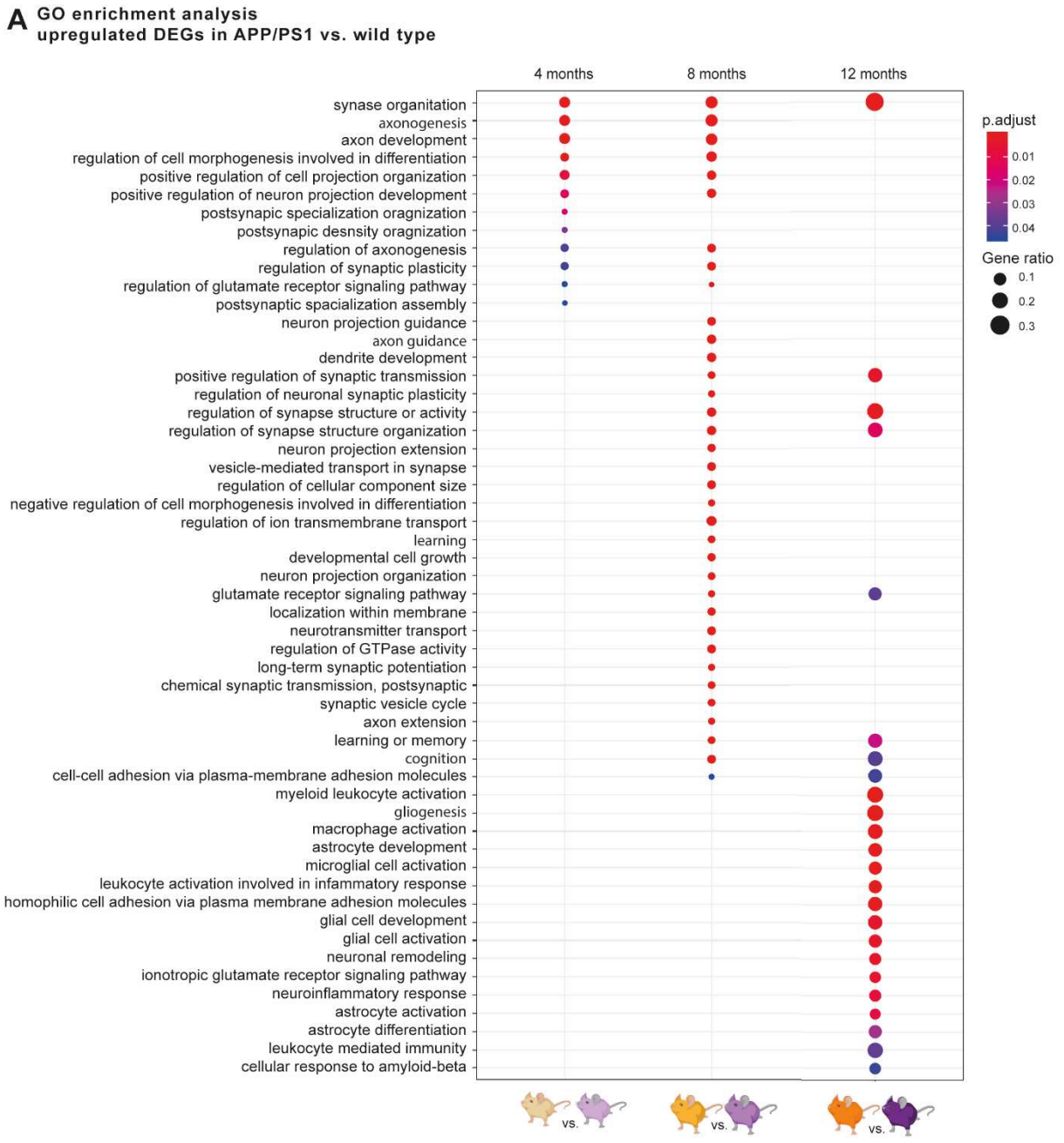

Figure 2-6 GO enrichment analysis of APP/PS1 vs. wild type within each age cohort. (A)GO enrichment analysis of DEGs comparing gene expression of APP/PS1 vs. wild type mice for each age cohort showed an upregulation of genes involved in synaptic organization in all ages. 4 months old and 8 months old have many similar terms identified, most of them dealing with synaptic or axonal processes. Some overlapping terms from 8 months old and 12 months old upregulated DEGs are involved in learning or memory and cognition, whereas in the old APP/PS1 mice many terms are connected to glial/astrocyte activation, differentiation and development and inflammatory terms. Colour scale from red to blue indicates the increasing p-value. Dot size indicating the gene ratio of the matching DEGs in the term to all genes defining the term.

To perform an analysis that is more pathway-specific, I used KEGG as an additional database. The KEGG enrichment for the middle-aged APP/PS1 mice showed axonal guidance and calcium signalling pathways as most prominent terms, whereas in the old mice the most prominent genes belong to the innate immune and complement/coagulation system as well as disease terms such as Streptococcus aureus infection (Figure 2-7A).

Based on the importance of calcium signalling in astrocytes, and the goal of this thesis to gain more insight into calcium signalling mechanisms, I performed a more detailed analysis of genes included in this enrichment term. This analysis revealed several surface proteins, such as receptors and channels (e.g. *Adra1d*, *Drd1a*, *Cacla1d*), as well as several downstream effector proteins (Figure 2-7B).

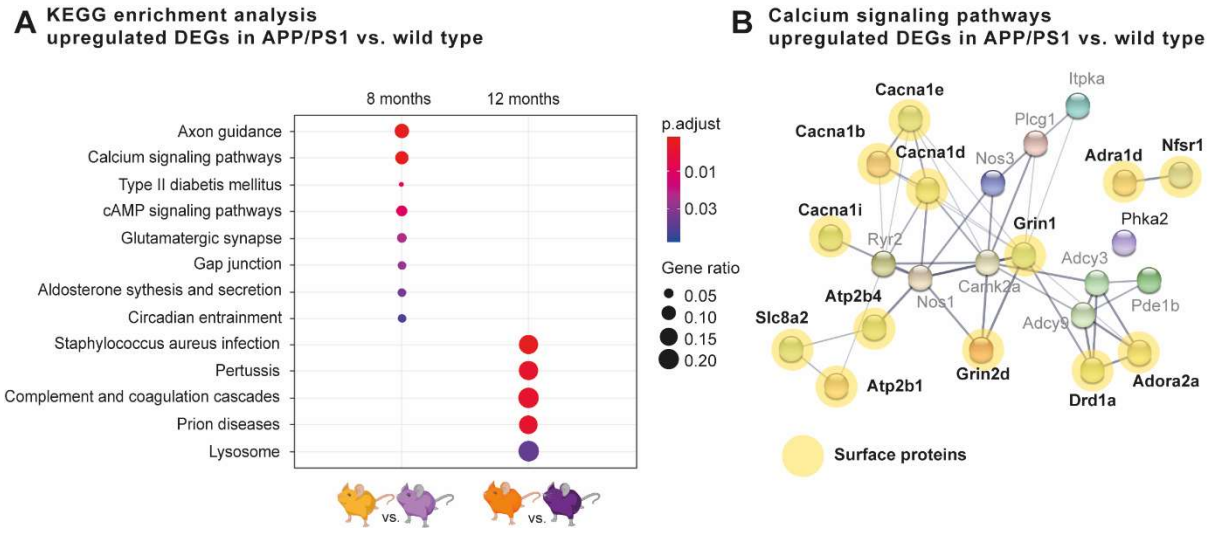

Figure 2-7 KEGG enrichment analysis of APP/PS1 vs. wild type. (A) KEGG enrichment analysis of DEGs comparing gene expression of APP/PS1 vs. wild type mice for each age cohort showed an upregulation of genes involved in axonal guidance and other signalling pathways like calcium signalling pathways and cAMP signalling pathways in 8 months old APP/PS1 mice. 12 months old APP/PS1 mice have upregulated DEGs involved in Staphylococcus aureus infection or complement and coagulation cascade, both containing genes for proteins associated in innate immunity. Colour scale from red to blue indicates the increasing p-value. Dot size indicating the gene ratio of the matching DEGs in the term to all genes defining the term. (B) SNA interactome of the 14 genes matching DEGs in the defined term calcium signalling pathways with labelled surface proteins in yellow. Thickness of the lines in the network indicating the strength of data support.

To better define the expression and ultimately the role of membrane-bound receptors that are involved in astrocyte signalling, I additionally performed a cluster analysis of expression changes of surface and downstream effector proteins, called surfaceome (https://www.proteinatlas.org/about/licence). Specifically, Cluster Profiler was used to analyse and visualize functional profiles of genes or gene clusters of our dataset related to the surfaceome, based on the common ontology and pathway databases (HALLMARK, GO, KEGG, Reactome, Disease). The subsequent sustained output was a surfaceome gene cluster network, indicating the identified clusters with all genes referred to the clusters that also allows the estimation of similarities of each cluster by proximity (Figure 2-8A). In addition, gene clusters were visualized in a heatmap to obtain an overview of the gene expression levels for each condition.

The surfaceome of our data set consisted of 7 different clusters, indicated by the coloured bars on the right site of the heatmap with the corresponding gene numbers that each cluster includes (Figure 2-8). From each cluster, the most relevant enrichment terms were selected from the Reactome (green), KEGG (purple) and Disease (brown) GSEA. In the pink cluster, which contains 172 genes enriched in terms of the immune system (21 genes, p.adjust = 0.03) and metabolic pathways (12 genes, p.adust < 0.01), these processes were activated in wild type mice during aging and in old APP/PS1 mice. The midnight blue cluster, which contained the highest number of genes (306), showed an upregulation in APP/PS1 mice of all age groups, as well as in old wild type mice. This cluster included terms for signal transduction, such as GPCRs (39 genes, p.adjust = 0.02) in the Reactome analysis. In addition, calcium signalling pathways (21 genes, p.adjust = 0.02) were found in the KEGG enrichment analysis for this cluster. Furthermore, this gene cluster showed also relevance to our disease model with an enrichment in AD-related genes (20 genes, p.adjust = 0.008) in the Disease enrichment database, confirming that this cluster has a strong relevance in our experimental model (Figure 2-8B). Within this cluster, I also identified several sub-clusters with genes related to neurotransmitter signalling. For example, several GPCRs of the acetylcholine receptor signalling pathways and adrenergic receptor signalling pathways were upregulated. I also identified another sub-cluster with genes relevant for calcium signalling, such as cation channels (*Trpm2, Ttpv2*) or subunits for voltage-gated calcium channels (*Cacna1h, Cacna1i* (subunits from $Ca_v3.2/3$ channel)) (Figure 2-8C). The yellow cluster (158 genes) revealed genes that were upregulated exclusively in APP/PS1 mice and downregulated in all wild type cohorts. These genes are mostly associated with the innate immune system (20 genes, p.adjust < 0.0001) and axonal guidance (9 genes, p.adjust = 0.01), as well as neurodegenerative diseases (20 genes, p.adjust = 0.02) (Figure 2-8B). In a small subset of genes from the innate immune system, specific genes involved in the complement and coagulation cascade were identified. The complement system is known to play a crucial role in microglia and astrocytes during AD where it is thought to support the engulfment of synaptic compartments

(Lian et al. 2016; Lian et al. 2015). In contrast, there are also several genes involved in axonal extension, development and, as shown here, axonogenesis. Additionally, an enrichment in genes implicated in neurodegenerative diseases (20 genes, p.adjust = 0.02) was observed (Figure 2-8D). The salmon cluster (253 genes) showed similar terms as the midnight blue and yellow clusters, including a very general term with neuronal system (50 genes, p.adjust < 0.0001) and genes related to calcium signalling pathways (23 genes, p.adjust < 0.001). However, genes in this cluster were upregulated in young and middle-aged APP/PS1 mice, and downregulated or unaffected in the old APP/PS1 and in any wild type mice cohort. The next three clusters (blue, cyan, turquoise) showed a different pattern with upregulated genes in the young and middle-aged wild type mice and a downregulation in all APP/PS1 mice and old wild type mice. The blue cluster (220 genes) showed genes involved in homeostasis (16 genes, p.adjust = 0.004) and metabolic pathways (14 genes, p.adjust = 0.04). Only a small number of genes were obtained in the cyan cluster (60 genes) with genes implicated in signal transduction (14 genes, p.adjust = 0.03) and GPCR ligand binding (9 genes, p.adjust = 0.02). The turquoise cluster (67genes) contained a low number of terms, such as genes involved in cytokine signalling in immune system (6 genes, p.adjust = 0.02) and development (5 genes, p.adjust = 0.04).

Overall, based on the number of genes and their purported function, the most promising clusters for gene manipulation and further investigation in the context of AD were the yellow cluster as well as the midnight blue cluster (Figure 2-8B).

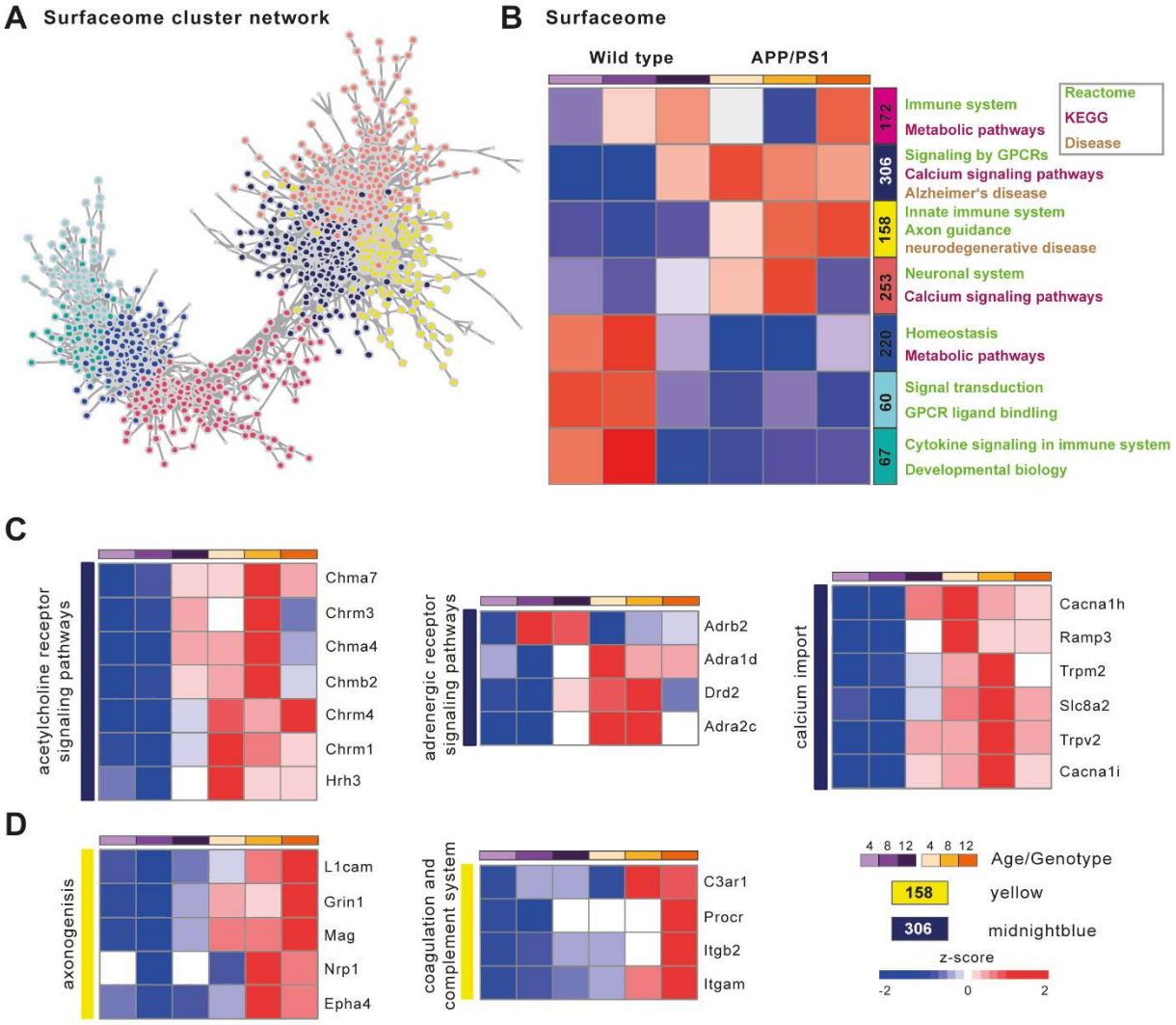

Figure 2-8 Surfaceome gene cluster network and corresponding relevant GSEA (A) Gene cluster network, illustrating all genes from the used gene set for surface proteins and the direct downstream effector proteins. Each dot represents one gene, distance between the dots the similarities or relationship and the colours referred to the gene cluster. (B) Heatmap indicating mean expression of genes included in the corresponding cluster for each age and genotype condition. The four upper clusters (pink, midnight blue, yellow and salmon) showed a general direction to genes higher expressed in APP/PS1 and old wild type mice and a low expression in 4 months and 8 months old wild type mice. The opposite is observable for the lower three clusters (blue, cyan, turquoise). Numbers in the coloured bars indicate the genes identified in each cluster. Relevant terms from GSEA using Reactome, KEGG and Disease enrichment database are assigned to the corresponding cluster. (C) Midnight blue sub-clusters of individual genes found differentially expressed in the term calcium signalling pathways, like neurotransmitter receptor signalling pathways as for acetylcholine or adrenalin. An additional sub-cluster showed different channels regulating the calcium import. (D) Yellow sub-clusters of individual genes found differentially expressed in the term axon guidance, like axonogenesis. Additional sub-cluster from the term innate immune system, showed genes from the coagulation and complement system, mainly upregulated in the old APP/PS1 mice. Z-score indicates minimal and maximal z-scaled expression. Bars above the heatmaps indicate the genotype (violets for wild type and oranges for APP/PS1 mice) and colour intensity the age cohorts (young indicated by light colours getting darker with age).

2.1.3.1 SUMMARY

The RNAseq data set revealed an important role of genes involved in synapse organisation during normal aging, but even stronger and earlier due to Aβ pathology. Genes associated with metabolism and metabolic pathways are upregulated to a similar extend to aging regardless of the Aβ pathology in APP/PS1 mice.

GSEA of the regulated surface proteins and downstream effector proteins uncovered critical gene clusters with a high relevance to neurodegenerative diseases and AD. These two main important clusters included genes related to the innate immune system and axon guidance as well as important GPCRs involved in cholinergic and adrenergic signalling and several genes associated to Ca^{2+} signalling pathways.

2.2 *In vivo* Ca^{2+} imaging of cortical astrocytes in awake behaving mice

To enable the recording of Ca^{2+} responses in the cell soma and the processes of astrocytes in awake behaving mice, an astrocytic transduction with a GECI is required. Therefore, I used an adeno-associated virus (AAV) encoding for the astrocyte-specific short *GFAP* (*GfaABC1D*) promoter (Lee et al. 2008) followed by the sequence of *GCaMP6f*, which enalbes the expression of this green-fluorescent GECI specifically in astrocytes.

2.2.1 Intravenously administered AAV facilitates a non-invasive transduction of astrocytes

Transducing cortical astrocytes with AAVs for expression of the genetically encoded calcium indicator GCaMP6f was performed by intercranial injections. Injecting substances into the brain tissue requires skull opening and piercing the dura by inserting a glass capillary. This procedure results in a high expression of the AAV-inserted gene in a small fraction of cells surrounding the injection site. In addition, a scar is formed at the injection site, leading to reactive astrogliosis as illustrated by increased Gfap expression in the cortex (Figure 2-9 upper panel). To avoid these disadvantages of cranial injections and ensure more widespread GCaMP6f expression, we took advantage of a recently developed AAV capsid variant, AAV.PHP.eB that enables a transduction of the whole brain by a single intravenous injection (Chan et al. 2017). Transducing astrocytes with the intravenously administered AAV enables, in theory, a transduction of all astrocytes in the brain. Comparing GCaMP6f expression in the cortex from both injection approaches, intravenous injection resulted in an even expression of numerous astrocytes without inducing reactive astrogliosis evidenced by the relative absence of Gfap-expressing astrocytes in the cortex (Figure 2-9 lower panel). With both injection routes, a pronounced Gfap expression in the adjacent hippocampus is visible. However, it is known that hippocampal astrocytes show gene expression differences compared to cortical astrocytes, including high expression of Gfap under normal conditions (Hinkle et al. 1997). In addition, intracranial injection disrupted some of the normal cortical layer structure as illustrated in Figure 2-9 (Dapi channel), which is in clear contrast to the intravenously transduced brain where distinct cortical layers were still visible (Figure 2-12).

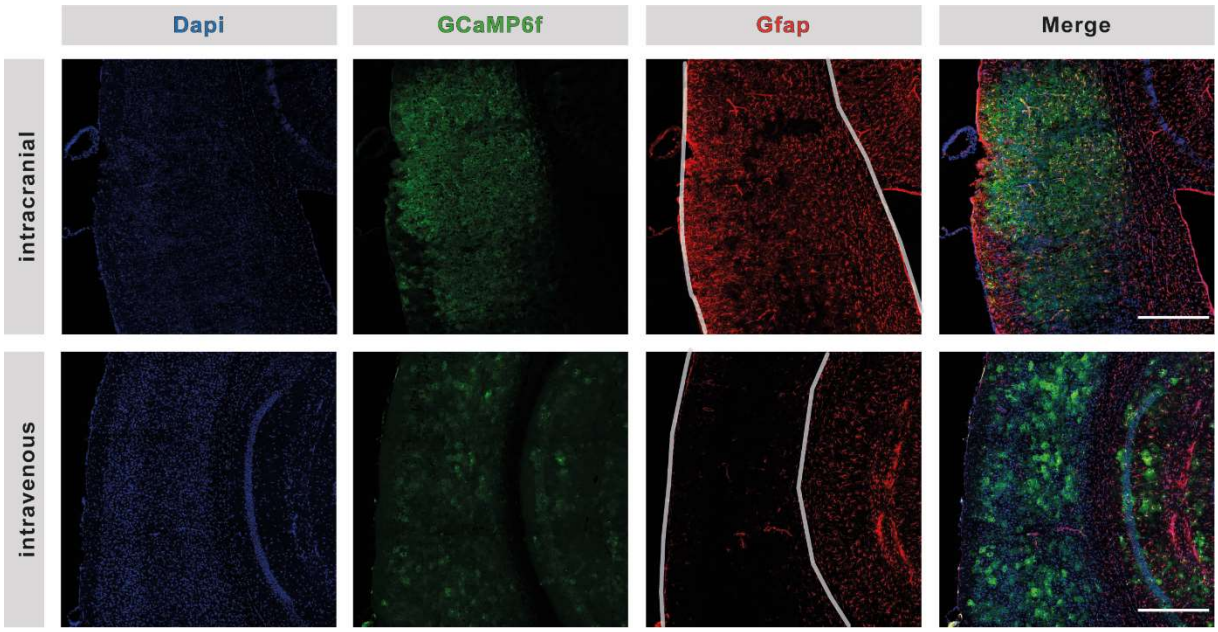

Figure 2-9 Comparing AAV transduction approaches to enable GCaMP6f expression in cortical astrocytes by immunohistological staining. (upper panel) Intracranially injected AAV caused tissue disruption, seen in the organisation of the Dapi stained nuclei (blue), induced high GCaMP6f expression (green) and triggered the Gfap expression (red) in astrocytes at the injection site. Merging all channels demonstrated a colocalization of the GCaMP6f expressing astrocytes with the Gfap positive astrocytes. (lower panel) after intravenous injection, the cortical layer organization was not affected, clearly visible in the Dapi channel, fraction of astrocytes expressing GCaMP6f and nearly no Gfap staining is detectable in the cortex. Region within the grey borders label cortex. Scale bars indicate 500 µm.

Overview images of other brain regions demonstrate the successful transduction of astrocytes with GCaMP6f-positive cells in the cerebellum, small fraction of astrocytes in the hippocampus and an even distribution of transduced astrocytes in the cortex. To prove the cell specificity, anti-Sox9 antibody was used to label all astrocytic nuclei (Sun et al. 2017) (Figure 2-10), and transduction efficiency was determined from the cortex by counting GCaMP6f-positive astrocytes and Sox9-positive nuclei.

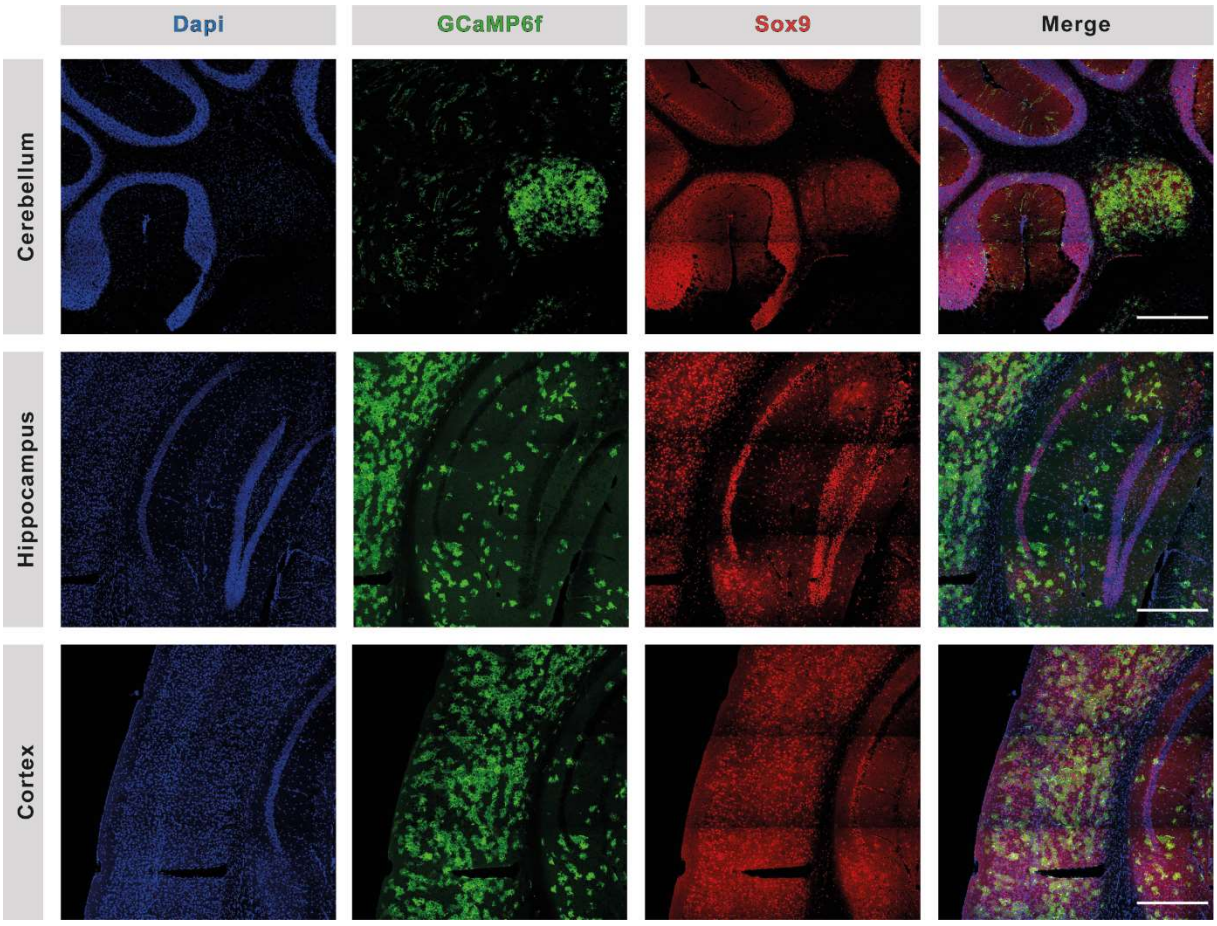

Figure 2-10 Transduction of astrocytes in different brain regions. GCaMP6f positive astrocytes were detected in the cerebellum (upper panel) the hippocampus (middle panel) and the cortex (lower panel). Astrocytic nuclei were visualized by counter staining with a Sox9 antibody and all nuclei by Dapi staining **Due to the auto fluorescent property, plaques colocalize and are visible in the Sox9 channel and the Dapi channel of APPPS1-21 mice** Scale bars indicate 500 µm.

This analysis showed a relatively high variability between individual mice regardless of genotype, but no differences in the transduction efficiency between wild type and APPPS1-21 mice. GCaMP6f and Sox9 double positive cells are visualized by white arrows in Figure 2-11A. Overall, systemic administration of AAV-GCaMP6f resulted in a mean transduction of 30.58% in cortical astrocytes, without significant differences between wild type (mean± SD; 37.86% ± 21.02) and APPPS1-21 mice (mean± SD; 23.31% ± 13.14; p = 0.145; Figure 2-11B). Therefore, systemic transduction of astrocytes with GCAMP6f was feasible and efficient, I consequently chose this method over intracerebral injections for the subsequent *in vivo* imaging studies.

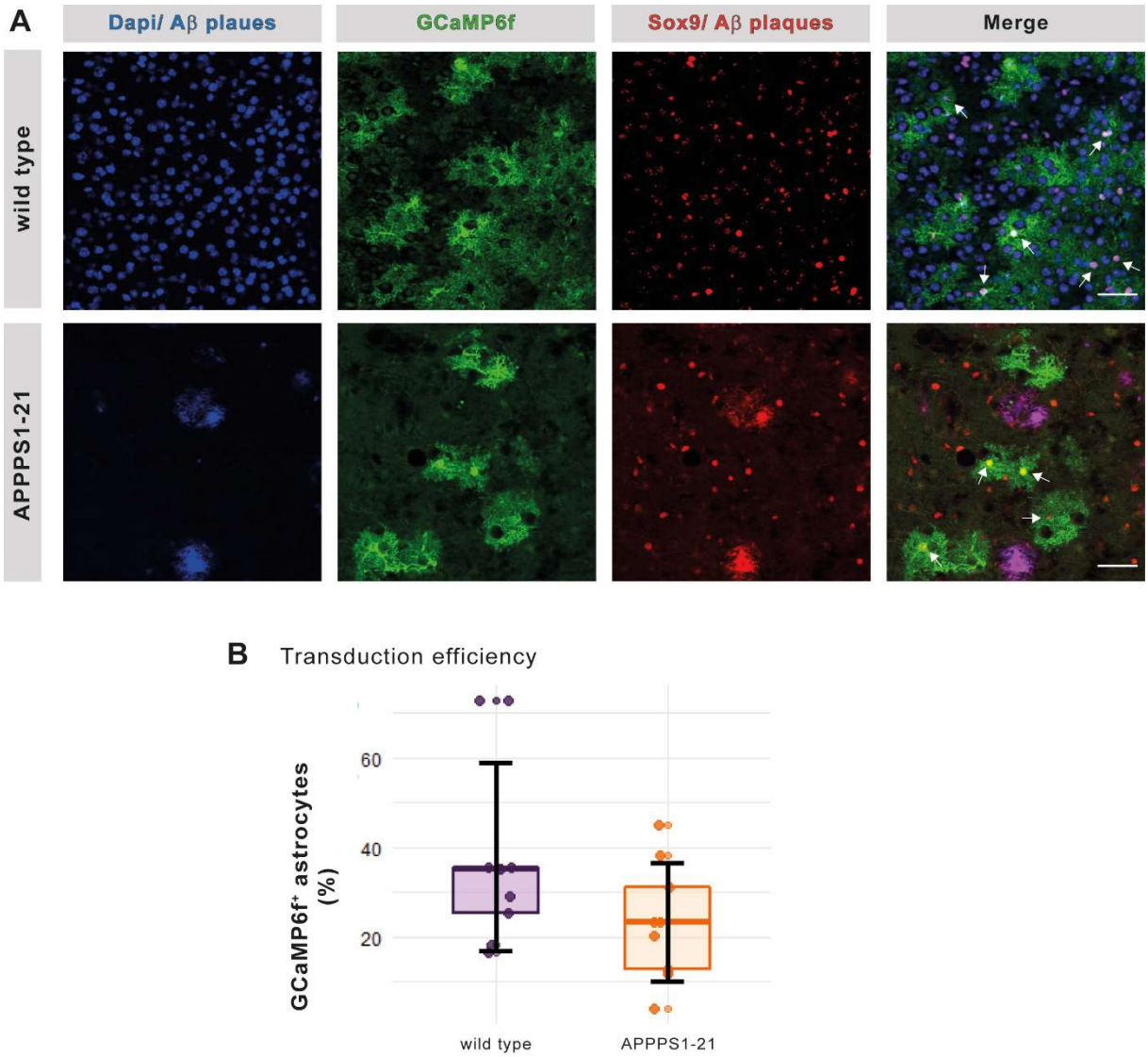

Figure 2-11 Quantification of the transduction efficiency. (A) Representative images of the immunohistological staining to quantify transduction efficiency in cortical astrocytes in wild type brains (upper panel) and APPPS1-21 brains (lower panel). Anti-GFP antibody was used to enhance fluorescent signal from expressed GCaMP6f and anti-Sox9 was used to label astrocytic cell nuclei. All nuclei and Aβ plaques were visualized in the Dapi channel and Aβ plaques were additionally detectable in the Sox9 channel. Successfully transduced and counted astrocytes are indicated by white arrows in the merged channel. Scale bars indicate 50 µm. (B) Boxplot of quantified transduction efficiency for GCaMP6f positive astrocytes in percent of cortical astrocytes. One data point represents average percentage of expression from 10 field of views of one mouse. Whiskers represent standard deviation. Kruskal-Wallis test; p = 0.145; n = 18

2.2.2 Identification of Ca^{2+} transients in cortical astrocytes

Since the RNAseq analyses had revealed an upregulation of adrenergic signalling receptors, I next determined whether this would also result in functional changes of Ca^{2+} activity in awake and behaving mice. For the recording of astrocytic Ca^{2+} activity, a chronic cranial window was implanted above the primary somatosensory cortex (Figure 2-12A) without injuring the brain tissue and dura. To enable an astrocyte-specific expression of GCaMP6f, a specific AAV was administered intravenously (Figure 2-12B) instead of the commonly used intracranial microinjection (Chen et al. 2013; Chan et al. 2017). This experimental setup allowed the simultaneous recordings of Ca^{2+} dynamics in cortical astrocytes in mice running on a linear treadmill head-fixed under a 2PLSM (Figure 2-12C). This approach is superior to studies conducted in anesthetized mice since anaesthetics-induced reduction of astrocyte activity was avoided (Thrane et al. 2012; Goldey et al. 2014) and furthermore, enabled a longitudinal investigation to identify alteration during Aβ progression in APPPS1-21 mice.

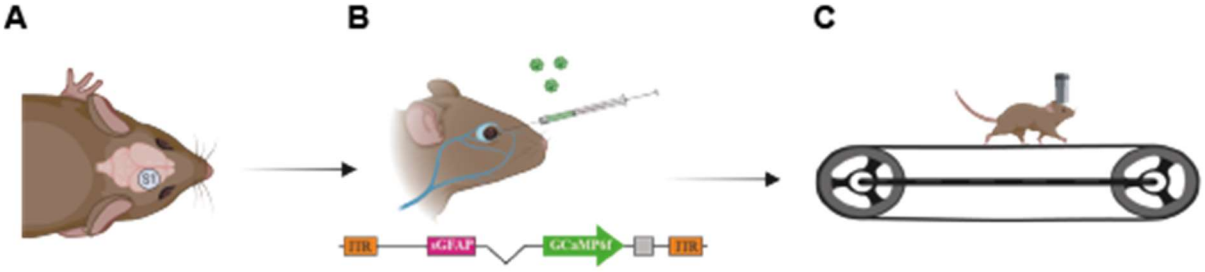

Figure 2-12 Scheme of experimental procedure. (A) Chronic cranial window implantation above the primary somatosensory cortex. After recovery of the mouse, (B) retro-orbital intravenous AAV injection. Containing the target vector, encoding for the short GFAP promoter (sGFAP) controling the expression of cytosolic GCaMP6f in astrocytes. (C) After a certain expression period, longitudinal awake *in vivo* two-photon Ca^{2+} imaging was performed.

The astrocytic Ca^{2+} signals that were recorded as 5 minutes time series, showed spatiotemporally highly dynamic signal changes that were visible as green-fluorescent domains of different intensities within astrocytes (Figure 2-13). As described in previous studies, Ca^{2+} dynamics during resting conditions appeared to be activated in a random fashion (Ding et al. 2013; Paukert et al. 2014; Zheng et al. 2015). However, during locomotion, broad wave-like signals occurred, as illustrated in Figure 2-13.

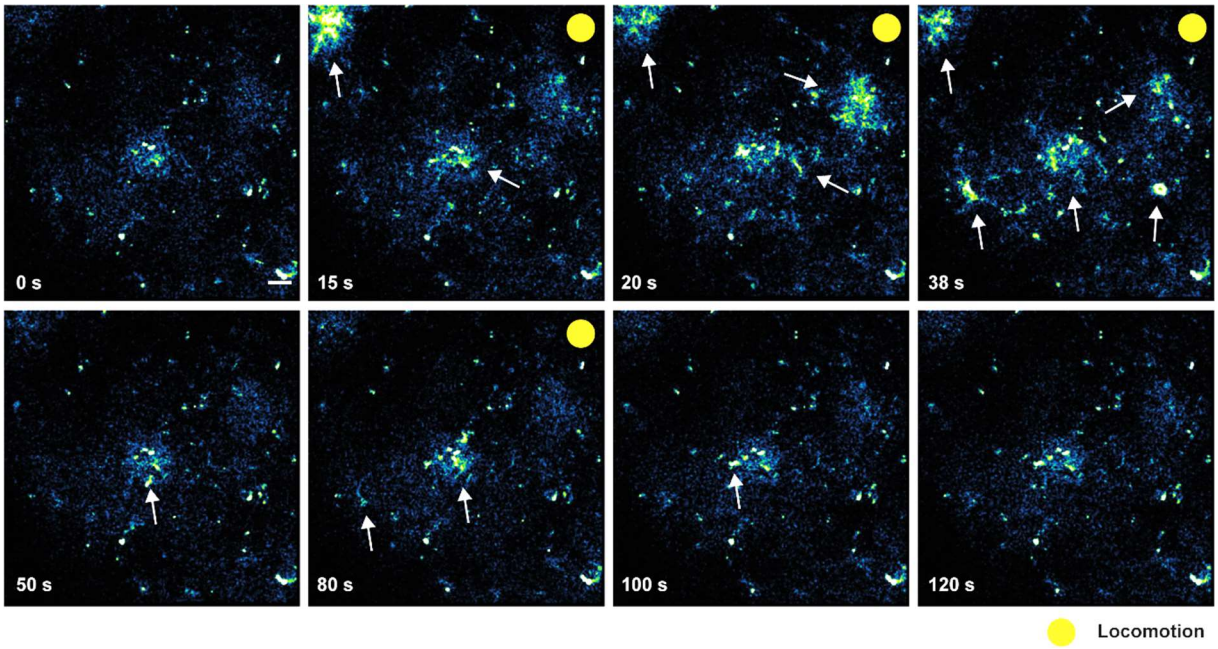

Figure 2-13 Representative time series of imaged Ca^{2+} dynamics. Individual images of different time points from a time series illustrating the astrocyte activity by recording Ca^{2+} signals. Fluorescent intensity of cytosolic GCaMP6f is indicated from black with, no signal over light green to yellow, with a strong signal. Locomotor activity in this series is indicated by the yellow dot and time in seconds (s) is indicated in the left corner. Scale bar indicates 20 µm.

Figure 2-14A shows example images of distinct time points from the above-mentioned time series revealing spatiotemporally distinct Ca^{2+} dynamics. Arrows indicate time-dependent activated whole astrocytes or astrocytic domains (Figure 2-14A). To detect individual regions of interest (ROI) and to investigate the frequency of events and their kinetics in these domains, I used different customized tools suitable for our generated dataset. Therefore, the image sequence was pre-processed using ImageJ by applying a 3D background noise filter and projecting it along the time axis (Figure 2-14B). Using this domain detection tool, the resulting data was generated as a table containing raw intensity data of each ROI over time. To subsequently verify the detection of Ca^{2+} events, the intensity data was analysed using a machine learning tool that helped to detect peaks that fulfilled prespecified features. Specifically, a classifier was trained to identify invalid and valid peaks, enabling an unbiased analysis of Ca^{2+} events in all recorded time series (Figure 2-14C). The processing of the Ca^{2+} imaging time series with this pipeline results in a dataset with kinetic features of the events as well as the extracted Ca^{2+} traces of the active domains. Figure 2-14D illustrates a representative Ca^{2+} trace from the labelled active domain marked by the red circle in the image. In this example, the trace shows a locomotion-induced Ca^{2+} increase in an active domain of an astrocyte process.

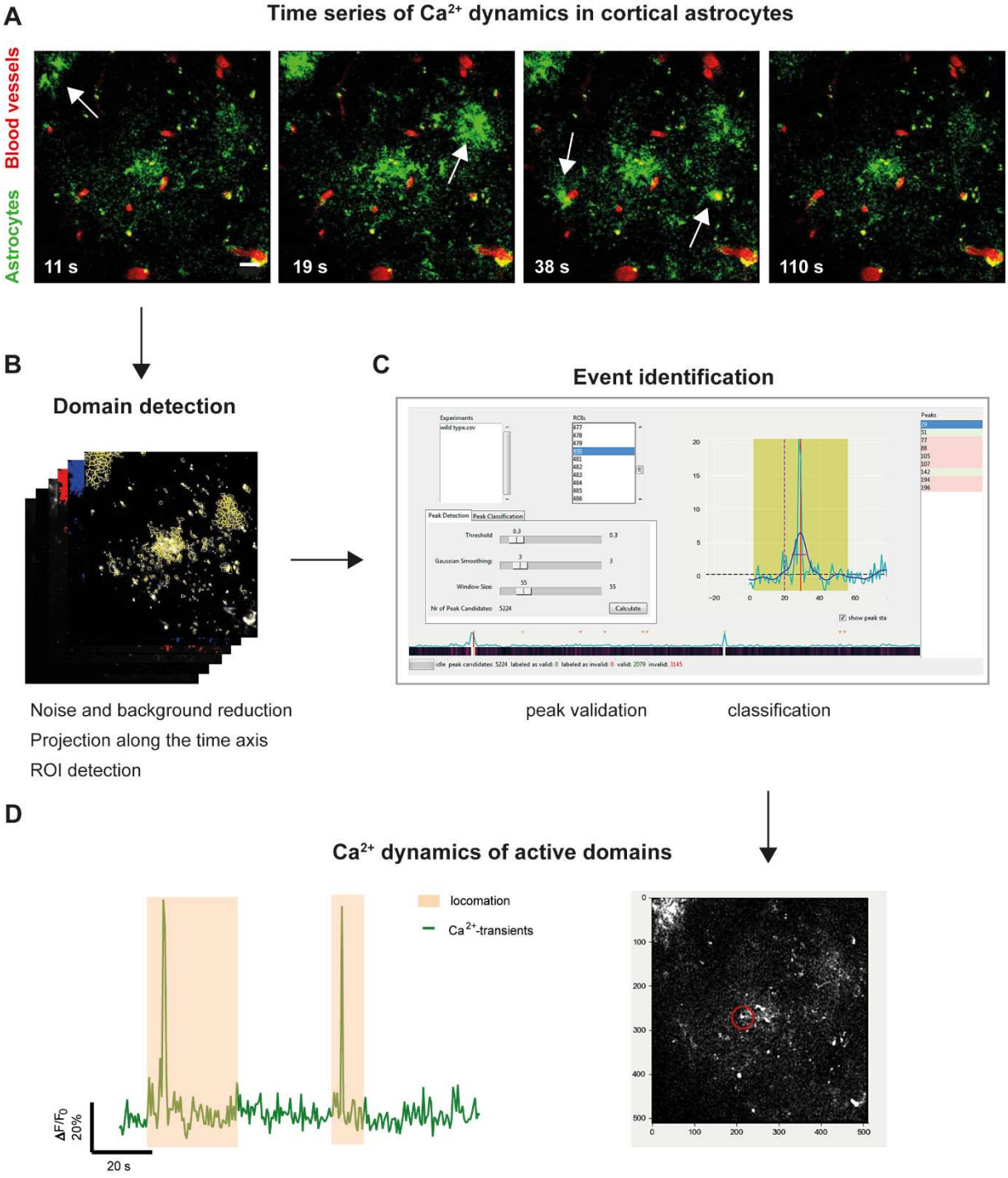

Figure 2-14 Analysis of astrocytic Ca^{2+} dynamics. (A) Example images from four diffenent time points (11 s, 19 s, 38 s and 110 s) to illustrate Ca^{2+} dynamics in cortical astrocytes. Scale bar indicates 20 µm (B) Domain detection after noise and background reduction, based on the projection along the time axis. (C) Event identification by validation and classification of peaks. (D) Illustation of an extracted example Ca^{2+} trance (green curve) of one detected active domain (red circle) over the complete time series representing Ca^{2+} dynamics in response to locomotion (orange shaded).

2.2.3 Locomotion induces Ca^{2+} transients in cortical astrocytes

In our RNAseq data analysis described above, we detected gene expression changes related Ca^{2+} signalling that were significantly regulated by aging itself. Therefore, we decided to perform the *in vivo* Ca^{2+} imaging in another AD mouse model to avoid the potentially confounding influence of aging and to investigate changes solely related to amyloid pathology. Thus, I used the APPPS1-21 mouse line which expresses similar transgenes as the APP/PS1 mice. Both mouse lines express mutated forms of the *APP* and the *PS1* gene. The distinction to the APP/PS1 mouse line is a different mutation within the *PS1* gene. In addition, the transgene expression is controlled by the neuron-specific promotor Thy1. Together these differences lead to an early and robust Aβ pathology within the used mice with 5 to 8 months of age (Radde et al. 2006).

Ca^{2+} imaging was performed on two different 2PLSM setups for technical reasons, resulting in two different imaging frequencies 3.82 Hz and 14.8 Hz. In cortical astrocytes, I observed extremely rare Ca^{2+}transients under resting conditions and even less frequent in anesthetized mice (Data not shown). Due to the low baseline activity of cortical astrocytes, the recordings of Ca^{2+} responses require the wakefulness of the mouse and stimulus to acquire a sufficient Ca^{2+} response (Ding et al. 2013; King et al. 2020). Studies investigating Ca^{2+} transients in cortical astrocytes of anesthetized mice compared to awake mice demonstrated a drastically lower frequency of spontaneous as well as evoked Ca^{2+} transients (Thrane et al. 2012). Furthermore, it has been shown very recently that the Ca^{2+} baseline under resting conditions influences the peak and amplitude of evoked Ca^{2+} transients (King et al. 2020).

In this study, I recorded Ca^{2+} transients in resting states as well as during locomotor activity. As illustrated in the Figure 2-13 and the example trace of Figure 2-14D, locomotion of the mouse resulted in a clear increase in the fluorescence intensity in astroglial active domains. To further investigate this locomotion-triggered increase and to uncover alterations between wild type and APPPS1-21 mice, active domains in all recorded field of views (FOVs) were analysed. To illustrate the fluorescence intensity differences upon locomotion, Figure 2-15A shows examples of active domains of astrocytes for each genotype. Sum projection of the corresponding time series and active domains of the astrocyte are shown in a ROI map next to the projection image (Figure 2-15A). Aβ plaques are strongly auto fluorescent and are thereby additionally visualized in the projection image from the APPPS1-21 mouse time series, indicated in dark blue of the corresponding ROI map (Figure 2-15A, right panel). Kymographs of these active domains showed a simultaneous fluorescence intensity elevation when the mouse started to run in both genotypes (Figure 2-15B). The status of the mouse defined as either “locomotion” or “rest” was determined by recording the position on the linear treadmill. In Figure 2-15B, running sections are visualized in black and resting sections in grey. By comparing the fluorescence intensity of these example kymographs, APPPS1-21 mice showed a higher intensity in the active

domains, which is furthermore visualized in three representative traces of active domains for both genotypes (Figure 2-15C). Comparing the representative kymographs and single traces in APPPS1-21 mice reveals an increased intensity in the active domains upon locomotion, indicating a higher Ca^{2+} fluctuation in the transgenic animals.

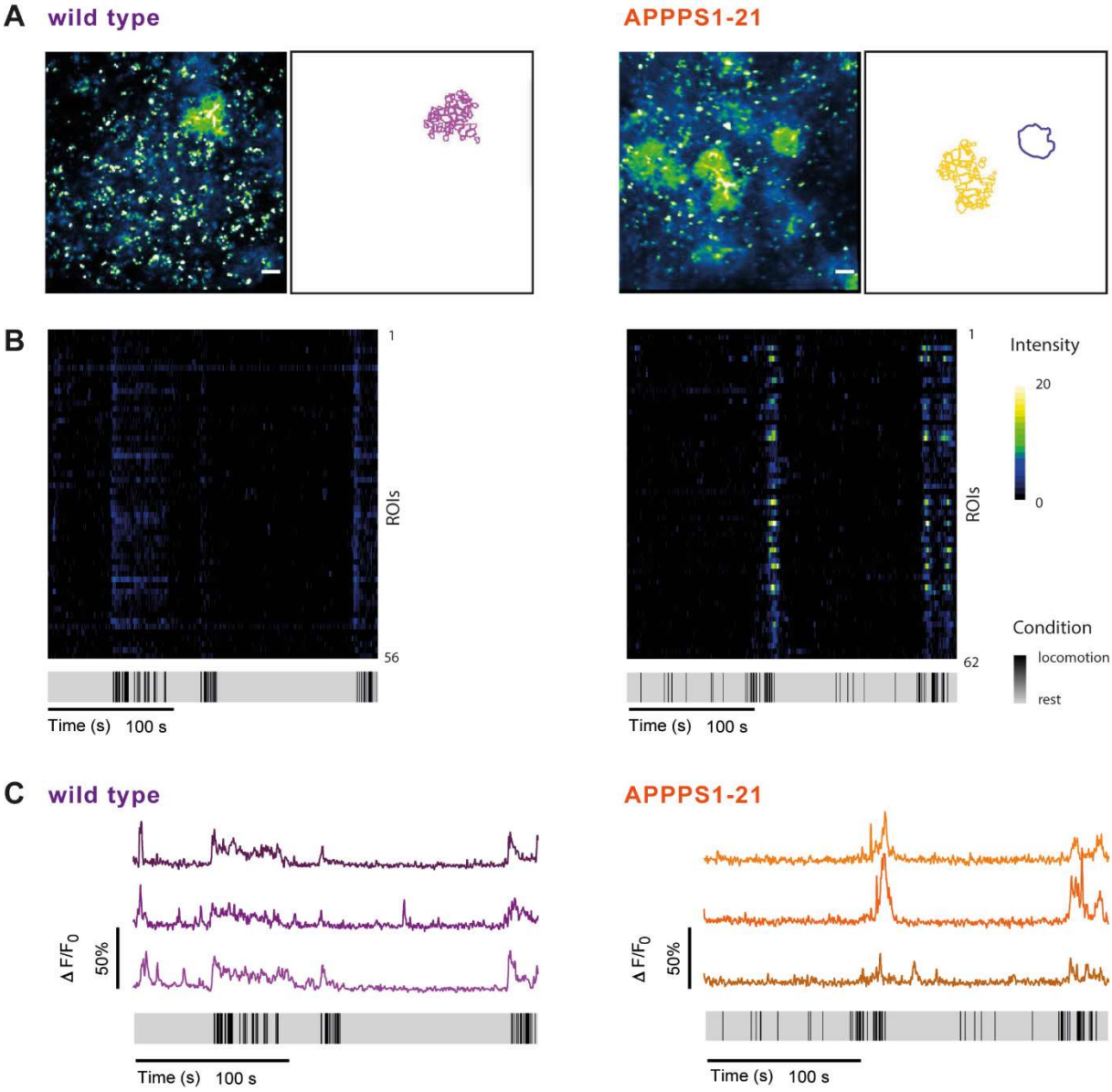

Figure 2-15 Locomotion-induced Ca^{2+} response in cortical astrocytes. (A) Sum projection (left panel) of representative time series to illustate active astrocytes with the corresponding active domains (ROI map) for wild type (violet) and APPPS1-21 (orange) mice. Aβ plaque is indicated by the dark blue border in the ROI map for APPPS1-21 mouse. (B) Kymographs demonstrating colour-coded fluorescence intensity representing the Ca^{2+} change over time of 300 s. State of the mouse is indicated by the condition panel showing states of locomotion in black and resting in grey. (C) Extracted single Ca^{2+} traces from active domains of both genotypes represented in fluorescent change in % normalized to wild type data.

The analysis of the kinetics of all detected Ca^{2+} signals during states of locomotion and resting revealed that the Ca^{2+} signal amplitude was similar in both imaging setups during locomotion in APPPS1-21 mice. The only statistically significant difference was a higher amplitude under resting conditions compared to locomotion in wild type mice in the slow imaging setup (Figure 2-16A; Table 1). Another kinetic feature that I investigated was the duration of the Ca^{2+} signals, measured as the full duration at half-maximum (FDHM). There were no changes in FDHM in data obtained with the slow imaging setup between rest and locomotion or the two genotypes, respectively (Figure 2-16B; Table 2). However, in the fast imaging setup data, FDHM was significantly longer during locomotion than during rest in both genotypes (Figure 2-16B; Table 2). Moreover, FDHM was significantly longer in APPPS1-21 compared to wild type mice in both behavioural states (Figure 2-16B; Table 2).

Further descriptive kinetic properties of Ca^{2+} signals are rise time and decay time. However, none of these features seemed to be altered in any condition or genotype and were not affected by imaging speed in this analysis (Figure 2-17A, B).

Overall, Ca^{2+} imaging of cortical astrocytes showed a strong dependency of Ca^{2+} signals to the stimulus of locomotion and a longer duration of these signals compared to resting condition. In addition, comparing FDHM in wild type and APPPS1-21 mice, I identified a higher FDHM in APPPS1-21 in both conditions, i.e. locomotion and rest, with the fast imaging setup.

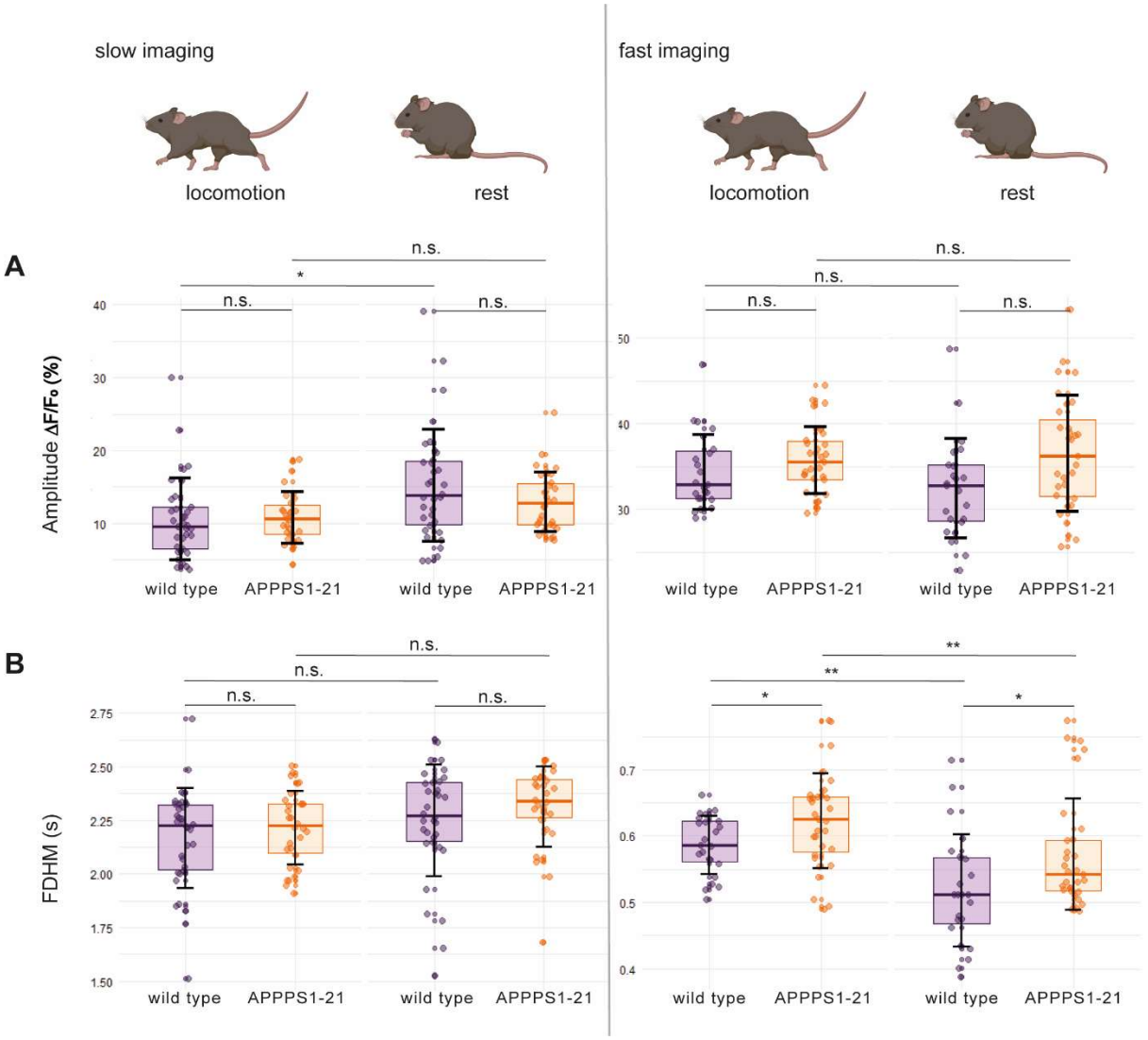

Figure 2-16 Signal kinetics of Ca^{2+} signals in cortical astrocytes. (A) Amplitude detected in the slow imaging was increased during rest in wild type mice, while no change was detected in APPPS1-21 animals or with fast imaging for both genotypes. (B) Full duration at half-maximum (FDHM) was unchanged in slow imaging data and significantly higher in APPPS1-21 mice during locomotion as well as in resting periods. In addition, Ca^{2+} signals were significantly longer upon locomotion compared to signals in resting mice for both genotypes. Whiskers represent standard deviation. Kruskal-Wallis test followed by Wilcoxon pairwise comparisons test; * $p < 0.05$, ** $p < 0.01$; n = 8-12 time points from 3 mice/genotype for slow imaging data and 4-5 mice/genotype for fast imaging data.

Table 2-1 Overview of the Amplitude for each condition.

Imaging setup	Condition	Genotype	Mean ± SD (%)
Slow	Locomotion	Wild type	10.94 ± 8.11
Slow	Locomotion	APPPS1-21	10.61± 4.3
Slow	Rest	Wild type	16.28 ± 14.68
Slow	Rest	APPPS1-21	12.14± 5.1
Fast	Locomotion	Wild type	34.43± 6.3
Fast	Locomotion	APPPS1-21	35.66± 6.87
Fast	Rest	Wild type	33.04 ± 9.56
Fast	Rest	APPPS1-21	37.08 ± 12.01

Table 2-2 Overview of the full duration at half-max (FDHM) for each condition.

Imaging setup	Condition	Genotype	Mean ± SD (s)
Slow	Locomotion	Wild type	2.18± 0.36
Slow	Locomotion	APPPS1-21	2.22± 0.26
Slow	Rest	Wild type	2.28± 0.42
Slow	Rest	APPPS1-21	2.28± 0.29
Fast	Locomotion	Wild type	0.59 ± 0.08
Fast	Locomotion	APPPS1-21	0.63 ± 0.1
Fast	Rest	Wild type	0.51 ± 0.12
Fast	Rest	APPPS1-21	0.58 ± 0.13

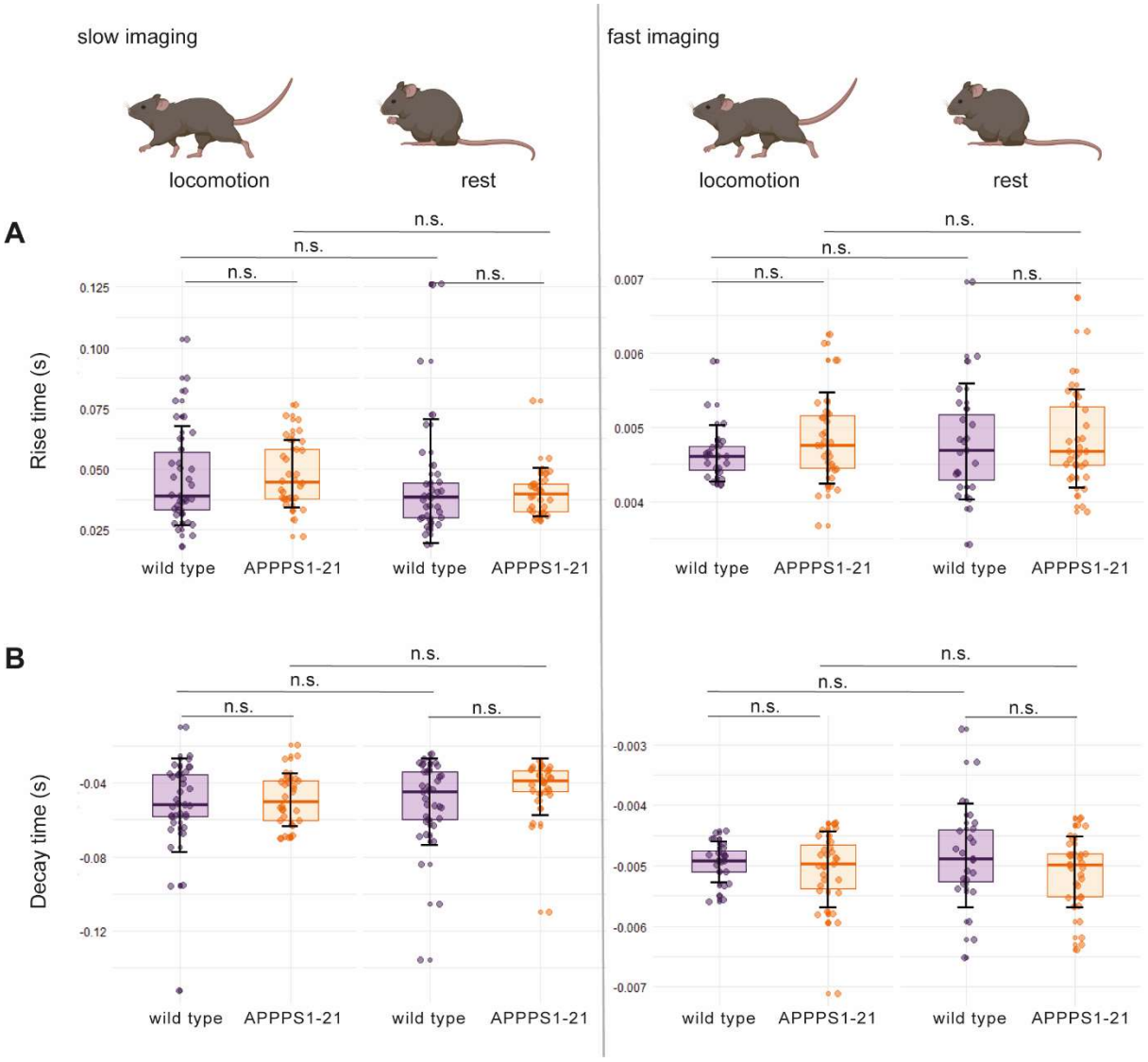

Figure 2-17 Rise and decay time of Ca^{2+} events. (A) Rise time of Ca^{2+}signals showed no differences in any experimental condition. (B) likewise, the decay time. Whiskers represent standard deviation. Kruskal-Wallis test followed by Wilcoxon pairwise comparisons test; ns = $p > 0.05$; n = 8-12 time points from 3 mice/genotype for slow imaging data and 4-5 mice/genotype for fast imaging data.

2.2.4 Higher frequency of Ca^{2+} events in APPPS1-21 mice

Experiments using acute cranial windows in anesthetized mice conducted in our lab as well as by others, demonstrated hyperactivity or higher activity of cortical astrocytes in AD mouse models with Aβ pathology (Kuchibhotla et al. 2009; Delekate et al. 2014; TAKANO et al. 2007). This higher activity points to a functional change of astrocytes due to Aβ pathology (Perez-Nievas und Serrano-Pozo 2018). To investigate whether this hyperactive astrocytic phenotype also exists under awake conditions, I recorded the frequency of Ca^{2+} events in a longitudinal fashion in weekly imaging sessions. Here, the APPPS1-21 mouse model was imaged within the age range from 5 to 8 months where mice have been reported to show Aβ plaque deposition that further increased over the two to three months of imaging period (Radde et al. 2006). For the analysis, I first determined the area per FOV occupied by active astrocytes. This analysis showed no differences between the genotypes. (mean ± SD: wild type = 20.6% ± 9.7%; APPPS1-21 = 23.8% ± 9.9%; p = 0.318; Figure 2-18A). The spatial size of individual astrocytic active domains was also similar, although there was a tendency for larger domain sizes in APPPS1-21 mice (Figure 2-18B, Table 2-3).

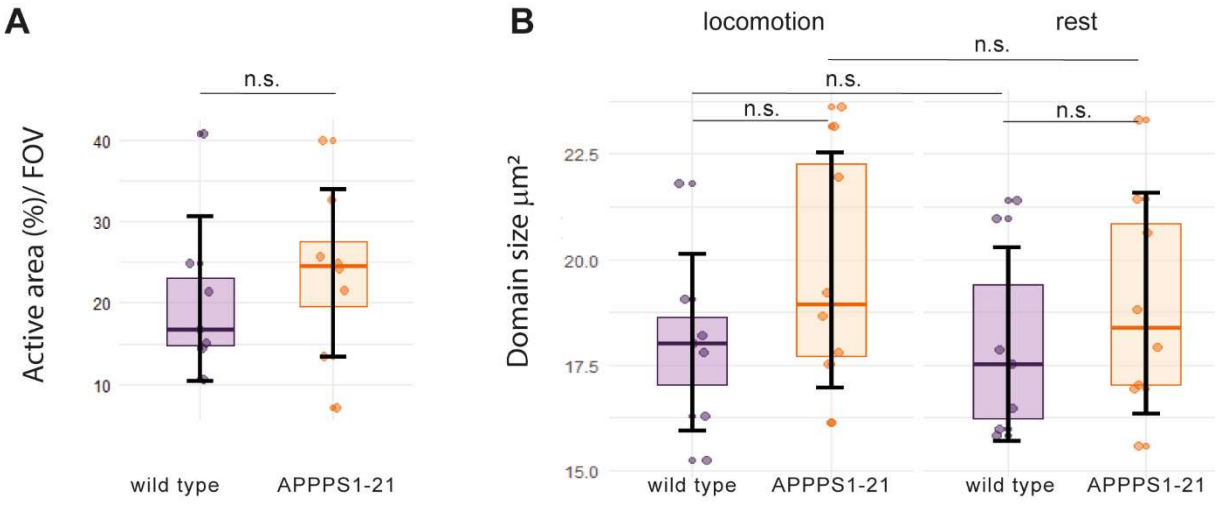

Figure 2-18 Active analysed area and domain size. (A) Mean area of active astrocytes in % from each FOV was not changed (B) Detected mean domain size of each FOV in µm² was slightly but nonsignificantly increased in APPPS1-21 mice in both conditions. Whiskers represent standard deviation. Kruskal-Wallis test. ns= p > 0.05; n = 8-12 time points from 7-8 mice/genotype.

Table 2-3 Overview of the domain size in µm² for each condition.

Condition	Genotype	Mean ± SD (µm²)
Locomotion	Wild type	18.05 ± 2.09
Locomotion	APPPS1-21	19.76 ± 2.80
Rest	Wild type	18.00 ± 2.30
Rest	APPPS1-21	18.96 ± 2.62

Next, I determined the frequency of Ca^{2+} events occurring within the defined active domains during locomotion and during rest from data sets of both microscopic setups (i.e. slow and fast imaging speed). The dataset from slow imaging comprises of longitudinal data for 12 weeks and fast imaging data for 8 weeks. The frequency of events per second remained stable across the span of imaging timepoints in both setups and genotypes (Figure 2-19A). However, when all data were pooled, the data showed a significantly higher frequency in APPPS1-21 mice for both setups and in both behavioural states (Figure 2-19B; Table 3).

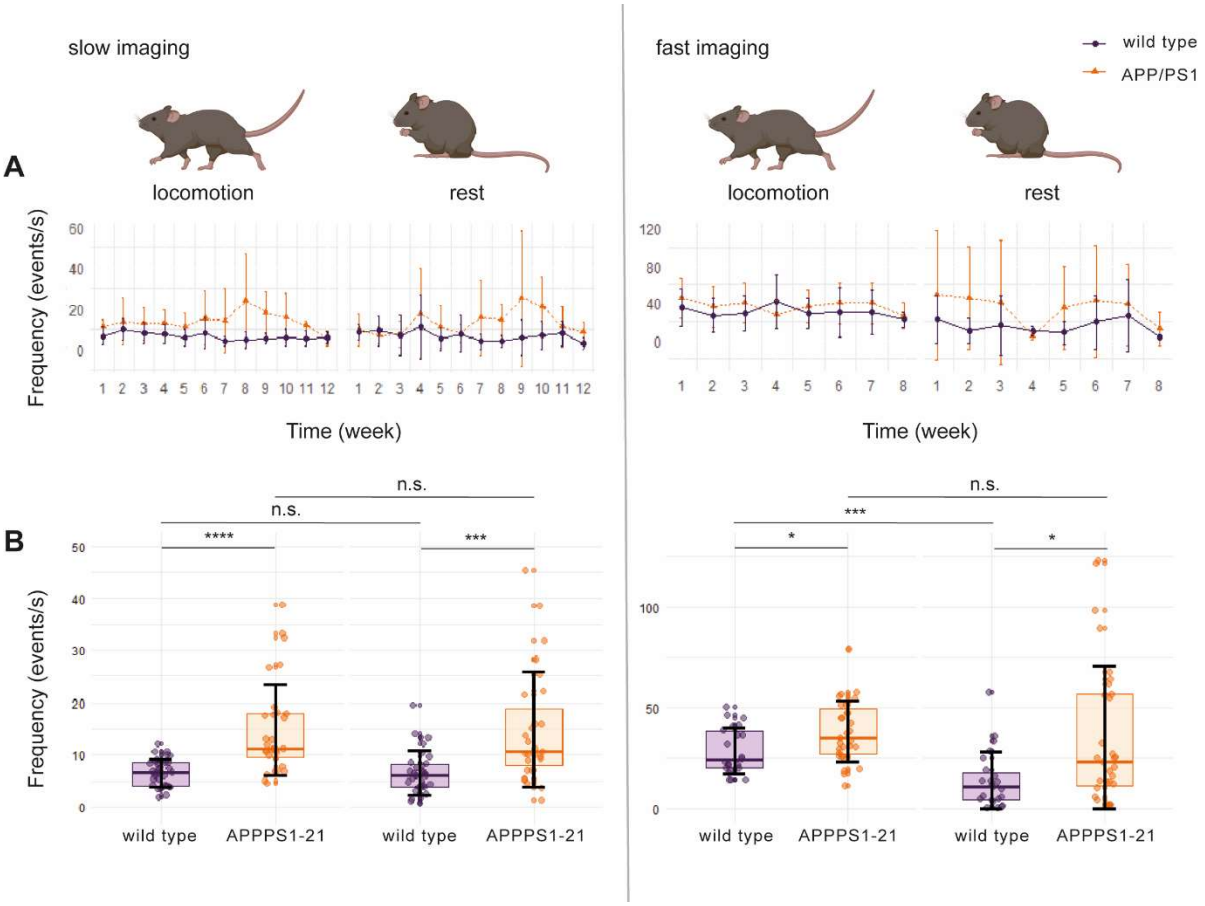

Figure 2-19 Frequency of Ca^{2+} events over time and overall. (A) Frequency of Ca^{2+} events over time upon locomotion and during rest. APP/PS1 mice showed tendency of more events in all conditions with both imaging setups. However, frequency was unchanged over time. (B) Mean events from each time point per mouse showed an increased frequency in APPPS1-21 mice compared to wild type with the same magnitude for both conditions with slow imaging. Fast imaging data demonstrated higher frequency in APPPS1-21 mice at the same magnitude for both conditions compared to wild type, but frequency in wild type mice during rest was significantly lower to frequency upon locomotion. Kruskal-Wallis test followed by Wilcoxon pairwise comparisons test; ns = $p>0.05$, * $p < 0.05$, ** $p < 0.01$, *** $p < 0.001$, **** $p < 0.0001$; n = 8-12 time points from 3 mice/genotype for slow imaging data and 4-5 mice/genotype for fast imaging data.

Table 2-4 Overview of Ca^{2+} event frequency for each condition.

Imaging setup	Condition	Genotype	Mean ± SD (events/s)
Slow	Locomotion	Wild type	6.64 ± 4.68
Slow	Locomotion	APPPS1-21	13.55 ± 10.94
Slow	Rest	Wild type	6.77 ± 8.37
Slow	Rest	APPPS1-21	12.68 ± 14.41
Fast	Locomotion	Wild type	29.75 ± 20.8
Fast	Locomotion	APPPS1-21	38.45 ± 21.09
Fast	Rest	Wild type	15.32 ± 24.5
Fast	Rest	APPPS1-21	38.08 ± 55.2

Taken together, *in vivo* Ca^{2+} imaging of cortical astrocytes in awake mice showed a locomotion-triggered Ca^{2+} response in astrocytes. Furthermore, the detected events showed slower kinetics upon locomotion compared to resting conditions, while events were slower in both conditions in APPPS1-21 mice. In addition, higher frequencies of events per second in APPPS1-21 mice compared to wild type mice were observed for all conditions.

2.3 Increased expression of α1-ARs in reactive cortical astrocytes in APPPS1-21 mice

In the preceding paragraphs, I used RNAseq data from astrocyte-specific mRNA to identify an upregulation of genes in APP/PS1 mice related to calcium signalling pathways. Calcium signalling is often regulated by surface protein activation, ligand binding to transmembrane receptors and channels. One differentially expressed GPCR in astrocytes is the α1-adrenoceptor (α1-AR) Adra1d, that showed a significant upregulation in APP/PS1 mice of all age cohorts in my dataset (Figure 2-8C). In addition to Adra1d, another α1-AR, Adra1a, is also known to be highly expressed by astrocytes (Zhang et al. 2014). To verify the upregulation of Adra1a and Adra1d in the context of Aβ pathology additionally in the APPPS1-21, and to estimate their expression in cortical and hippocampal astrocytes, I performed a multiplex fluorescence *in situ* hybridization, called RNAscope. The used mice were 7 months old and thereby reflect the Aβ plaque burden comparable to the mice used in the Ca^{2+} imaging experiments. To enable an astrocyte-specific quantification of Adra1a and Adra1d expression, I used a Sox9-specific probe to label all astrocytes and a Gfap-specific probe to identify reactive astrocytes. All cell nuclei and Aβ-plaques were visualized by Dapi.

An exemplified overview image of the stained wild type brain slices reveals prominent Adra1a distribution in the cortex while other brain regions were only sparsely labelled (Figure 2-20A). In contrast, Adra1d is densely localized in the upper layer of the cortex, and also highly expressed in the pyramidal cell layer of the hippocampus and in thalamic regions (Figure 2-20B).

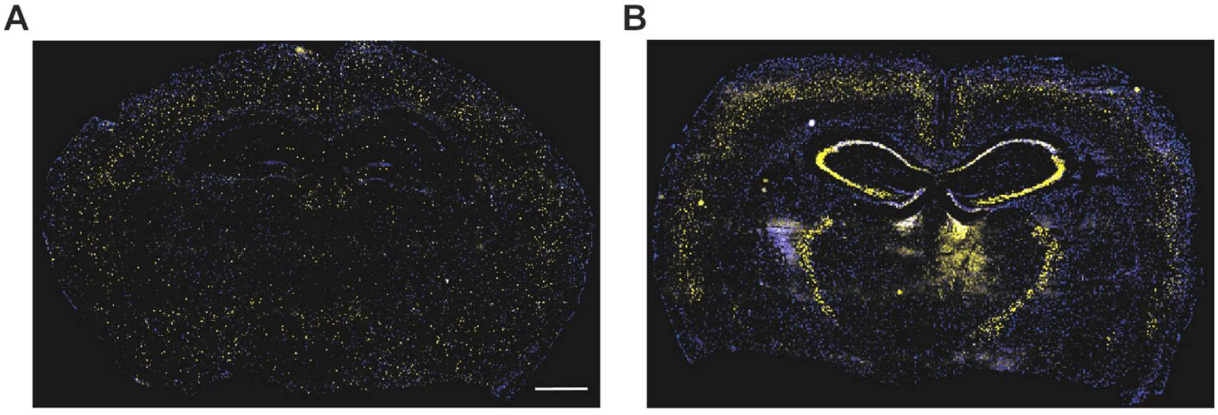

Figure 2-20 Localization of Adra1a and Adra1d in the brain. (A) Overview of Adra1a labelled mRNA (yellow) showed a main distribution of Adra1a positive cells in the cortex and a sparse labelling of cells throughout the other brain regions. (B) Overview of Adra1d labelled mRNA (yellow) showed a main distribution of Adra1d positive cells in the upper layers of the cortex, high labelling in the pyramidal cell layer of the hippocampus and a region in the thalamus. Nuclei were visualized by Dapi staining. Scale bar indicates 1 mm.

Higher magnified images from the cortex and the hippocampus demonstrated a dot-like staining for all used probes (Figure 2-21A, B). Visual inspection already showed a gene expression change between mice for Gfap, with an increase in the cortex (Figure 2-21A, lower panel). Both Sox9 and Gfap showed a rather spotted distribution across the entire cell body, while Adra1a staining localized to the nucleus or adjacent to the nucleus. For further analysis, I dichotomised astrocytes into reactive (Gfap-positive) and nonreactive (Gfap-negative) astrocytes. Quantification of cortical Adra1a expression revealed a significant decrease in nonreactive astrocytes (mean ± SD: wild type = 3.74% ± 4.09%; APPPS1-21 = 0.85% ± 2.26%; $p < 0.01$), while its expression was significantly increased in reactive astrocytes of APPPS1-21 mice (mean ± SD: wild type = 4.97% ± 3.85%; APPPS1-21 = 10.35% ± 5.37%; $p < 0.01$; Figure 2-21C, left). In contrast, hippocampal Adra1a expression was independent of astrocyte activation status (Figure 2-21C, right): comparable expression levels were found in nonreactive astrocytes (mean ± SD: wild type = 0.76% ± 2.41%; APPPS1-21 = 1.10% ± 2.7%; $p > 0.05$) and in reactive astrocytes (mean ± SD: wild type = 3.11% ± 6.39%; APPPS1-21 = 2.25% ± 3.26%; $p > 0.05$). Similar labelling patterns were observed for the Adra1d (Figure 2-22A, B). Like Adra1a, quantification revealed a decrease of Adra1d-positive nonreactive astrocytes in APPPS1-21 mice (mean ± SD: wild type = 28.93% ± 17.67%; APPPS1-21 = 10.21% ± 14.48%; $p < 0.01$), while reactive astrocytes presented with a higher Adra1d expression in APPPS1-21 mice compared to wild type (mean ± SD: wild type = 36.08% ± 15.25%; APPPS1-21 = 51.95% ± 17.91%; $p < 0.01$; Figure 2-22C, left). Interestingly, quantification of hippocampal Adra1d expression resulted in equal expression pattern in both nonreactive astrocytes (mean ± SD: wild type = 31.41% ± 19.94%; APPPS1-21 = 37.43% ± 19.64%; $p > 0.05$) and reactive astrocytes (mean ± SD: wild type = 47.91% ± 22.32%; APPPS1-21 = 43.79% ± 21.01%; $p > 0.05$; Figure 2-22C, right).

Taken together, the isoforms of α1-adrenergic receptors, Adra1a and Adra1d, both show markedly higer numbers of positive reactive astrocytes in the cortex but not the hippocampus of APPPS1-21 mice.

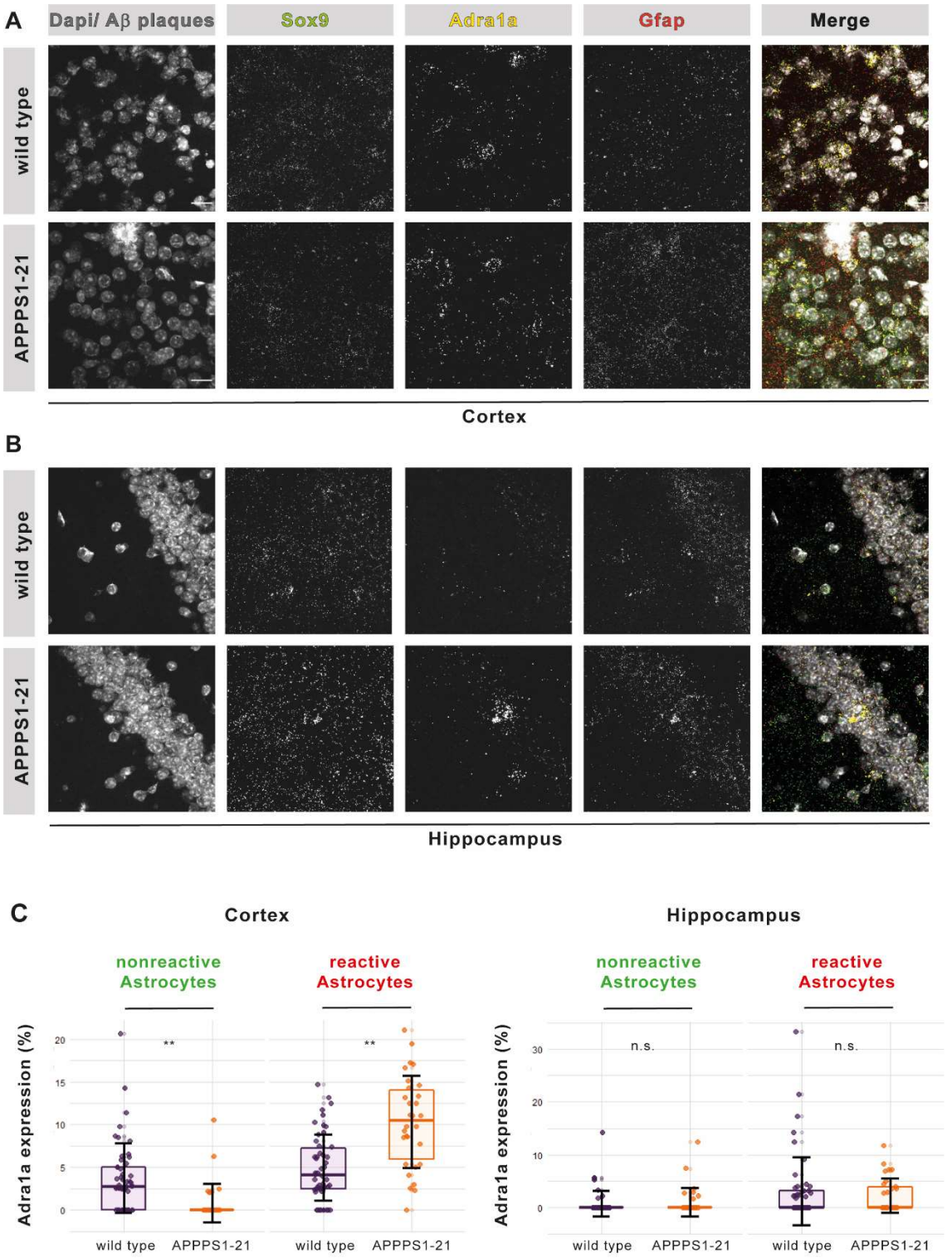

Figure 2-21 Adra1a expression in cortical and hippocampal astrocytes. (A, B) Multiplex fluorescent RNA *in situ* hybridization for Sox9 (green), Adra1a (yellow) and Gfap (red) in wild type (violet) and APPPS1-21 (orange) brains. Nuclei and Aβ plaques were visualized in the Dapi channel. Sox9 probe was utilized to identify all astrocytes and Gfap to identify reactive astrocytes. Scale bars indicate 50 µm. (A) Maximum intensity projections of z-stack images from the cortex. (B) Maximum intensity projections of z-stack images from the hippocampus. (C) Boxplot of determined Adra1a expression in nonreactive astrocytes (Sox9 single positive cells; green) was decreased ($p < 0.01$) and increased ($p < 0.01$) in reactive astrocytes (Sox9 and Gfap double positive cells, red;) in the cortex (left) of APPPS1-21 mice. In the hippocampus (right) no change was detected (nonreactive astrocytes $p > 0.05$; reactive astrocytes $p > 0.05$). One data point represents one field of view (FOV). 10 FOVs per mouse and per region were analysed. Whiskers represent standard deviation. Kruskal-Wallis test followed by Dunn's multiple comparisons test; ns = $p>0.05$, **$p <0.01$; n = 3-5 mice

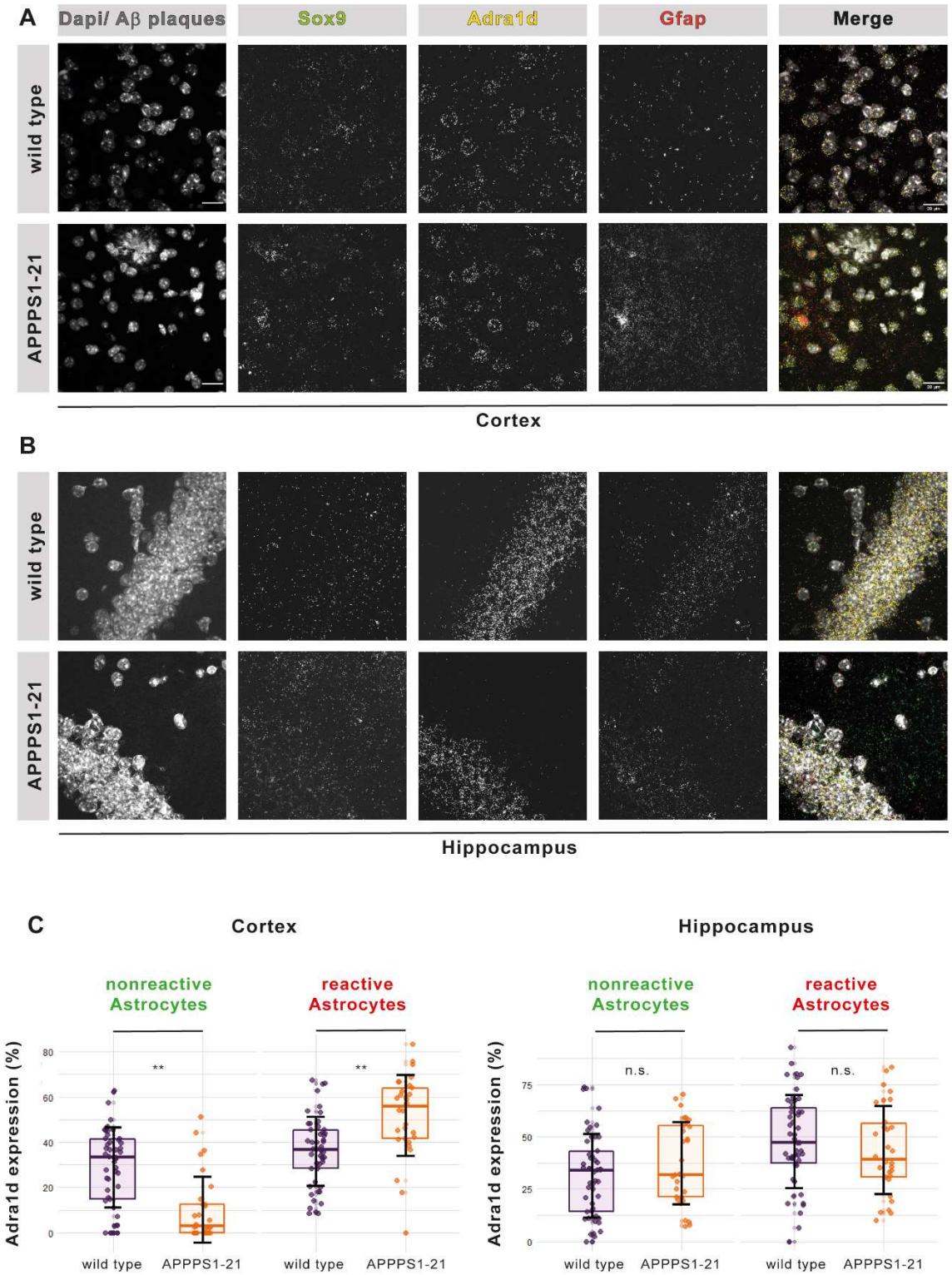

Figure 2-22 Adra1d expression in cortical and hippocampal astrocytes. (A, B) Multiplex fluorescent RNA *in situ* hybridization for Sox9 (green), Adra1d (yellow) and Gfap (red) in wild type (violet) and APPPS1-21 (orange) brains. Nuclei and Aβ plaques were visualized in the Dapi channel. Sox9 probe was utilized to identify all astrocytes and Gfap to identify reactive astrocytes. Scale bars indicate 50 µm. (A) Maximum intensity projections of z-stack images from the cortex. (B) Maximum intensity projections of z-stack images from the hippocampus. (C) Boxplot of determined Adra1a expression in nonreactive astrocytes (Sox9 single positive cells; green) was decreased ($p < 0.01$) and increased ($p < 0.01$) in reactive astrocytes (Sox9 and Gfap double positive cells, red;) in the cortex (left) of APPPS1-21 mice. In the hippocampus (right) no change was detected (nonreactive astrocytes $p > 0.05$; reactive astrocytes $p > 0.05$). One data point represents one field of view (FOV). 10 FOVs per mouse and per region were analysed. Whiskers represent standard deviation. Kruskal-Wallis test followed by Dunn's multiple comparisons test; ns = $p>0.05$, **$p <0.01$; n = 3-5 mice

3 Discussion

Here, I have found that the astrocytic translatome of the APP/PS1 mouse model of AD shows alterations in specific pathways associated with Ca^{2+} signalling. Specifically, and confirmed by *in situ* hybridization in APPPS1-21, I detected significant changes in the expression of α1-adrenoreceptors on reactive astrocytes in the cortex. I also showed that this genetic alteration correlated with altered Ca^{2+} responses during locomotion, as assessed by *in vivo* imaging of awake behaving mice, an effect mediated by adrenergic signalling. These data indicate that α1-adrenoreceptors may contribute to astroglial-neuronal network dysfunction during behavioural states in AD.

3.1 Advanced cell-type specific mRNA isolation

Genetic changes of astrocytes due to aging or neurodegenerative diseases have been addressed by several studies using different mouse models or techniques. (Clarke et al. 2018; Boisvert et al. 2018; Bronzuoli et al. 2019). The advantage of the RiboTag technique used in the present thesis is the extraction of cell-specific actively translated mRNA (Sanz et al. 2009). The classical procedure to isolate cell specific mRNA is fluorescent activated cell sorting (FACS) (Swartzlander et al. 2018; Zamanian et al. 2012). However, this technique features several limitations for the isolation of most of the brain cells. First, due to the morphological complexity of astrocytes, tissue dissociation leads to a massive loss of their highly ramified processes. Additionally, mechanical steps during the procedure and the tissue disruption induce immediate early genes and other stress-related responses and might trigger considerable changes in the transcriptional state (Sanz et al. 2009; Kang et al. 2017). Furthermore, the lack of appropriate specific cell surface markers represents one of the main issues resulting in a contamination of other cell types and/or a small yield of RNA. Consequently, the small yield leads to the need of pooling samples from different animals. In addition, the relatively harsh procedure results in a low RNA integrity number, which then represents a poorly suitable sample for further analysis as required for RNAseq or quantitative PCR (qPCR) (Swartzlander et al. 2018). Moreover, ribosomal mRNA translation not only takes place in cell somata close to the nucleus, but also occurs in fine distal processes, which may be lost during traditional cell-sorting techniques (Boulay et al. 2017). In the RiboTag approach, whole brains or regions are removed and directly frozen, reducing the probability of transcriptional changes induced by the procedure, and enabling the capture of all translating mRNAs including those from fine processes. The major advantage of RiboTag is the specific purification of translated mRNAs, excluding untranslated mRNA from the RNAseq analysis resulting in a dataset representing strictly speaking the translatome and not the whole transcriptome (King und Gerber 2016).

The brain incorporates a high variety of cell types and if mRNA isolation is not restricted to one, distinct changes in one specific cell type are diluted by the contamination from the residual cells (Okaty et al. 2011; Srinivasan et al. 2016). This fact is clearly displayed in the principle component analysis (PCA) of my dataset, where the total mRNA of all cell types showed no distinct separation amongst the different age cohorts or genotypes. However, total mRNA clusters clearly away from the RiboTag mRNA (Figure 2-2B). In contrast, the PCA based on the RiboTag mRNA indicated a distinct overall gene expression profile of the APP/PS1 mice clustering away from wild type mice. This, as well as the enrichment for astrocytic markers in RiboTag mRNA samples (Figure 2-1), attest to the purity as well the ability to perform comprehensive comparative analyses using this approach.

3.2 Age-related gene expression changes and their relation to Aβ pathology

To identify significant gene expression changes, DEGs were determined using comparisons between different age cohorts and between the different groups in the same age cohort. While identified DEGs in wild type mice represent age-related gene expression changes, identified DEGs in the APP/PS1 group represent changes related to Aβ pathology progression. Based on the plaque development, 4 months old APP/PS1 mice with no Aβ plaques reflect gene expression changes before AD onset, 8 months old cohorts mimic the early stage of AD with a rising Aβ plaque formation. Finally, the 12 months old mice feature a massive Aβ plaque burden and thus reflect the late onset of Aβ pathology (Jankowsky et al. 2001). Thereby, DEGs in the APP/PS1 group are induced, in addition to age-related changes, also by Aβ pathology progression (Figure 2-2A).

During normal aging in wild type mice, the highest number of DEGs were identified in comparison to middle-aged and old cohorts. This indicates that the major gene expression changes occur during normal aging between 8 months and 12 months of age. Previous studies addressing the expression changes in aged mice demonstrated an upregulation of genes involved in synapse elimination, and neuroinflammation and a decrease of genes for cholesterol synthesis (Clarke et al. 2018; Boisvert et al. 2018). In our data set, upregulated DEGs in the old mice vs. middle-aged revealed two clusters of genes (Gene ontology, (GO)-enrichment), synapse organization and regulation of synaptic plasticity (Figure 2-4A). Interestingly, genes in the synapse organization cluster were even stronger increased in all APP/PS1 mice, indicating an earlier increase of age-related alterations in APP/PS1 mice (Figure 2-4B). The interactome of these gene cluster illustrated two further sub-clusters, with 5 genes belonging to axion guidance and 4 for neurexins and neuroligins (Figure 2-4 C, D). These genes are poorly studied in astrocytes so far, but it is well known that astrocytes contribute to synaptic engulfment,(Gratuze et al. 2018; Jay et al. 2019), and the neurexin and neuroligin system has been implicated in neuronal connectivity and synaptogenesis (Hillen et al. 2018).

The high number of DEGs in the age-matched comparisons of APP/PS1 vs. wild type revealed pronounced gene expression changes in young (presymptomatic) and middle-aged (early stage disease) APP/PS1 mice. Surprisingly, mice with the highest plaque burden mimicking the late onset stage showed a marginal number of DEGs (Figure 2-2A). This indicates that on the one hand, the most relevant disease-related mechanisms are affected prior to the high abundance of plaques, and on the other hand, that aging itself induces similar changes as AD. One possible explanation might be related to the Aβ oligomer hypothesis which posits that Aβ oligomers are more toxic than insoluble Aβ plaques (Ferreira et al. 2007; Cline et al. 2018). While no identical genes were regulated when comparing middle-aged vs. young AD and wild type mice, the

comparison of old vs. middle-aged showed a set of DEGs identically regulated in both groups. These alterations might hence occur with aging, i.e. without an influence of Aβ pathology. Interestingly, only one GO-enrichment term was potentially relevant, containing genes associated to metabolism (Figure 2-4E). Astrocytes controlling blood brain barrier function and are thereby essential for brain homeostasis and metabolism (Zlokovic 2008). Genes such as *Sphk1* and *Cers1* are important in lipid metabolism, whereas *Entpd2* metabolizes ATP. These example genes are involved in processes producing important intracellular and extracellular second messengers as S1P or ADP. Both feature a significant impact on important cellular mechanisms as apoptosis or purinergic signaling (Delekate et al. 2014; Reichenbach et al. 2018; Wit et al. 2019; Fischer et al. 2011; Wink et al. 2006).

GO-enrichments from the age-matched APP/PS1 vs. wild type comparisons again confirmed the relevance of the synapse organization term as the only common term in all age cohorts. Furthermore, several other terms related to synaptic regulations were also found overlapped between 4- and 8-months old APP/PS1 mice. Interestingly, overlapping terms in 8- and 12-months old APP/PS1 vs. wild type mice are related to learning and memory, and cognition. APP/PS1 mice develop memory deficits upon Aβ pathology, examined by classical behavioural testing (Ashe 2001; Reichenbach et al. 2019). Hence, these GO-enrichments imply an alteration in genes associated to learning and memory in the early and late stage of Aβ pathology. While further terms related to synaptic regulations were uncovered in the early stage, terms referring to glial changes and to immune response in the mice mimicking the late stage of disease (Figure 2-6).

Taken together, the main astrocytic changes related to aging include genes linked to synapse biology, and these alterations occur earlier and are persistently induced by Aβ pathology. The higher number of DEGs in the presymptomatic and early disease stage may point to a stronger impact of Aβ oligomers than Aβ plaques. Additionally, the common group of genes upregulated in all old mice in wild type and in APP/PS1 indicate an Aβ pathology independent and age-related effects.

3.3 Astrocytic genetic phenotypes defined by Aβ pathology and aging

Reactive astrogliosis is the remarkable change on a morphological, molecular, and functional level to various pathological insults. Which gene expression changes occur is strongly dependent on the type of stimulus and the brain region. However, in the astrocyte research field the definition of the specific features of a reactive astrocyte is still not entirely resolved (Escartin et al. 2019). The upregulation of the *Gfap* and *Vim* genes is defined as the best-known feature for astrocyte reactivity. In addition to these genes, several others were frequently observed as astrocyte reaction on pathological stimuli and were thereby referred as pan-reactive marker genes. In addition to this classification there were genes correlated to a neurotoxic (A1) or neuroprotective (A2) astrocytic phenotype (Liddelow et al. 2017; Rakers et al. 2019).

Surprisingly, the data set analysed in this thesis does not support a specific astrocytic A1, A2 or pan-reactive phenotype (Figure 2-5). Even if some signature genes show a non-significant tendency to be elevated, a clear enhancement of these genes would be required to classify one specific phenotype. In general, *Gfap* upregulation is not only related to neurodegenerative diseases but also to normal aging (Clarke et al. 2018; Boisvert et al. 2018). However, two recent studies found nearly opposite expression patterns during aging and in AD models. Where the one study identified a new hippocampal astrocyte population with an specific heightened *Gfap* expression in aging and in particular in their AD model, another study showed a reduced Gfap protein level in hippocampal astrocytes from aged mice with and without AD-like pathology (Bronzuoli et al. 2019; Habib et al. 2020). These contrary conclusions illustrate that even the best-established marker for astrocyte reactivity does not consistently have to follow the classical expression pattern. Unexpectedly, the second well-known marker *Vim* was neither upregulated in APP/PS1 mice nor in aged mice in our data set (Figure 2-5A). However, amongst others, increased *Vim* expression, similar to the other depicted reactive markers, show extreme regional differences (Clarke et al. 2018; Boisvert et al. 2018). AD-related phenotypic changes were previously described to change towards purportedly neurotoxic astrocytes, similar to normal aging (Clarke et al. 2018; Habib et al. 2020).This classification failed verification with our generated data (Figure 2-5B). Interestingly, other recent studies have also failed to identify a clear-cut distinction between A1 and A2 phenotypes in various disease models (Ceyzériat et al. 2018; Wu et al. 2019; Diaz-Castro et al. 2019).

In summary, the dataset obtained in my thesis does not confirm the view that astrocytic reactivity can broadly be divided into two opposite genetic phenotypes. Astrocytes represent an extremely complex, highly heterogenous and regionally diverse cell type (Matias et al. 2019; Habib et al. 2020). Thus, future studies using single-cell RNAseq techniques will be necessary to identify regional heterogeneities as well as the full spectrum of astrocytic phenotypes.

3.4 Upregulated genes in astrocytic Ca^{2+} signalling pathways linked to Aβ pathology

Astrocytes are neuronal interaction partners at the synaptic terminals and can affect synaptic transmission (Di Castro et al. 2011; Haustein et al. 2014; Panatier et al. 2011). The detection of genes related to specific pathways and processes was determined based on the gene set enrichment analysis using KEGG database (Kanehisa 2019).Genes involved in terms such as axon guidance, Ca^{2+} signalling pathways, cAMP signalling pathways, glutamatergic synapses and gap junctions underlined the relevance of altered signalling cascades in the early stage of Aβ pathology. Only at the later stage an apparent shift towards genes associated with innate immunity arises, exemplified by the term coagulation and complement system (Figure 2-7A).

Due to the astrocytic contribution at the tripartite synapse, astrocytes express a large variety of cell surface signalling proteins. In the interactome of the genes provided by the enrichment term Ca^{2+} signalling pathways, a high abundance of neurotransmitter receptors and ion channels was identified (Figure 2-7B). The cluster analysis of the surfaceome, which includes cell surface proteins and downstream effector proteins, uncovered seven distinct gene clusters with diverse enrichment terms detected by Reactome, KEGG, and Disease enrichment analysis databases (Yu et al. 2012). In particular, clusters associated with terms such as the immune system or terms pointing to specific signalling cascades or processes were upregulated in APP/PS1 mice. In addition, the Disease Enrichment analysis showed that two clusters (midnight blue and yellow) also contain genes associated with neurodegenerative diseases and specifically Alzheimer's disease. While the yellow cluster comprise terms of the innate immune system and axon guidance, the midnight blue cluster comprise genes for GPCR signalling and Ca^{2+} signalling pathways (Figure 2-8B).

In the yellow cluster, the sub-cluster "axonogenesis" includes the cell adhesion molecule *L1cam*. Overexpression of this gene has been shown to be beneficial for the reduction of Aβ plaque load and astrogliosis in an APP/PS1 mouse model (Djogo et al. 2013; Leshchyns'ka und Sytnyk 2016). However, the role of L1cam overexpression in astrocytes in the context of AD has not been reported so far and the mechanism of action and how Aβ is reduced by astrocytes is unclear. Another interesting gene is *Grin1*, a channel-subunit for an ionotropic NMDA receptor (NMDAR). Released glutamate activates the receptor expressed by astrocytes which result in an intracellular Ca^{2+} rise (Palygin et al. 2010). In addition, in the case of an overexpression or an increased activation of the astrocytic NMDAR, this can lead to a glutamate-triggered excitotoxicity (Liu et al. 2019). A further promising candidate is the erythropoietin producing hepatocellular A4 (*EphA4*) that is involved in axonal outgrowth. Our data are in line with studies showing higher levels of EphA4 in AD patients and a correlation to synaptic dysfunction, thereby contributing to the

cognitive impairment induced by Aβ pathology (Fu et al. 2014a). Furthermore, *EphA4* was also found upregulated specifically in reactive astrocytes, and the blockage of this receptor had a beneficial outcome with regard to synaptic dysfunction and astrocyte reactivation in different disease models (Fu et al. 2014a; Frugier et al. 2012; Goldshmit und Bourne 2010) (Figure 2-8D).

The complement and coagulation system is associated with synaptic pruning during development and microglia-mediated synaptic loss by phagocytosis in AD (Luchena et al. 2018). Astrocyte-microglia communication through the complement system by C3 secretion from astrocytes and C3 receptor (C3ar1) activation on microglia had a beneficial effect for Aβ clearance (Lian et al. 2016). We also identified upregulated *C3ar1* in our dataset (Figure 2-8D). Interestingly, in microglia the activation of C3ar1 leads to an intracellular activation of the Stat3 pathway. Stat3 in astrocytes is strongly associated to induce astrocyte reactivity in different neurodegenerative disease and especially in AD (Reichenbach et al. 2019; Litvinchuk et al. 2018; Ben Haim et al. 2015). The other three genes, *Procr, Itgb2,* and *Itgam* are genes typically expressed in other cell type as endothelial cells, immune cells, and microglia (Clarke et al. 2018; Glawe et al. 2009; Wojtukiewicz et al. 2019) and my study is the first to identify their upregulation in astrocytes in an AD model.

The midnight blue cluster, containing the highest number of genes, demonstrated the direct significance to AD as discussed above and is thereby probably the most relevant cluster for this study. This sub-cluster specifically showed an upregulation of genes that are contributing to GPCR-induced Ca^{2+} elevation, such as cholinergic signalling and adrenergic signalling receptors, or proteins supporting Ca^{2+} import from the extracellular space. In fact, it has been shown that activated cholinergic receptors on astrocytes induce IP_3-dependent intracellular Ca^{2+} release, and it was also demonstrated that some subtypes might influence the communication to the vasculature at the astrocytic endfeet. The cholinergic system is known to play a crucial role in learning and memory, thus an altered expression of this receptors on astrocytes might have an impact on learning and memory deficits in AD (Kuchibhotla et al. 2009; Navarrete et al. 2012; Elhusseiny et al. 1999) (Figure 2-8C).

The sub-cluster of adrenergic signalling receptors includes three GPCRs sensing NE, each with a distinct cellular response. The Adrb2 receptor is a beta2 adrenergic receptor (β2-AR) that is connected to various pathway responses. In astrocytes, the most important signalling pathway mediated though Adrb2 is glucose uptake via a G_s-protein initiated cAMP-dependent activation of the glucose transporter 1 (Glut1). Dysregulations of this system is linked to AD (Dong et al. 2012). In our data, this receptor was expressed at lower levels in APP/PS1 than in wild type mice, however Adrb2 is upregulated in both groups if compared to the 4-month old mice. The AR Adra1d is an α1-AR associated with a G_q-protein activation and is linked to the signalling cascade activating the IP_3-mediated intracellular Ca^{2+} release (O'Donnell et al. 2012). This study is the first

to show that astrocytic *Adra1d* is upregulated in an AD model In our data, *Adra1d* was significantly upregulated in 4- and 8-month old APP/PS1 mice, while in 12-month old APP/PS1 mice *Adra1d* was not significantly upregulated anymore compared to wild type. This is due to an increased level of *Adra1d* in old wild type mice, again demonstrating the convergence of wild type and transgenic mice at old age due to genetic effects of aging itself (Figure 2-8C). Nevertheless, the relevance of α1-AR signalling in astrocytes was demonstrated in several studies not referring to one specific isoform of the existing three α1-AR (Ding et al. 2013; Paukert et al. 2014). The third type of upregulated AR was the α2-AR Adra2c, which activates the $G_{i/o}$-mediated cascade, inhibiting the cAMP production and consequently negatively regulating the neurotransmitter release at the presynaptic terminal (O'Donnell et al. 2012). The function in astrocytes however is not yet clear. Of note, a study performed with human AD patient tissue revealed reduced *ADRA1D* and *ADRA2C* expression in the hippocampus(Szot et al. 2006), however cell specificity was not tested and opposing expression levels may exist in neurons and astrocytes.

Another route for Ca^{2+} entry, beside the release from intracellular stores, is the regulated influx from the extracellular space. Some of these genes related to calcium import represent different subunits of the *low-voltage gated Ca^{2+} channel alpha 1* (*Cacna1h, Cacna1i* (*Cav3*.2, *Cav3.3*)), and the *transient receptor potential cation channels* (TRP channels; *Trpm2, Trpv2*) (Figure 2-8). The low-voltage gated ion channel activity mainly supports the balanced intracellular Ca^{2+} level in the astrocyte responding to the Ca^{2+} concentration to the extracellular space (Rungta et al. 2016), but specific data about its role in physiology and diseases are scarce. Trpm2 and Trpv2 are nonselective Ca^{2+} permeable cation channels. Trpm2 in astrocytes is activated by a critical intracellular Ca^{2+} concentration or by different danger associated molecules from the extracellular space (Wang et al. 2016). Therefore, the activation of Trpm2 by reactive oxygen species (ROS) can lead to a higher activation which may contribute to the expression changes during aging (Wang et al. 2016; Jiang et al. 2018). Furthermore, Aβ is also able to activate these channels (Sita et al. 2018). In contrast, the thermosensitive Trpv2 responds to endogenous lipid metabolism or heat (Shibasaki et al. 2013), but its role in astrocytes and especially in the context of neurodegenerative diseases is largely unknown. A further important protein for ion homeostasis in astrocytes is the Na^+/Ca^{2+} exchanger 2 (Slc8a2 or Ncx2), which regulates ion exchange specifically at the fine astrocytic processes ensheathing excitatory synapses. Additionally, NCXs are controlled by the cytosolic Na^+/Ca^{2+} concentration and provide short-lived Ca^{2+} transients in microdomains triggered by ongoing synaptic activity (Minelli et al. 2007; Brazhe et al. 2018). The upregulation of *NCX2* has also been observed in synaptic terminals from AD patients, confirming our data (Sokolow et al. 2011). On the other hand, NCXs are crucial to refill the intracellular Ca^{2+} stores (Sisalli et al. 2014) and the upregulation could act as an compensatory

effect due to the higher frequency of intracellular Ca^{2} release in astrocytes triggered by AD pathology (Figure 2-8C).

Conclusively, these two clusters uncovered interesting proteins upregulated in response to Aβ pathology. For some of the identified genes, other studies have already demonstrated a putative relevance to astrocytes or AD, while several other proteins have currently not yet been characterized in this context. Due to the important role of Ca^{2+} signalling in astrocytes mediated by GPCRs, the most promising candidates for further studies represent the α1-ARs. Remarkably, the *in situ* hybridization also showed a significant upregulation of both genes specifically in cortical reactive astrocytes of APPPS1-21 mice (Figure 2-21, 22). The functional consequences of these results will be discussed below.

3.5 Behaviour-dependent Ca^{2+} response in cortical astrocytes underlines adrenergic signalling changes in APPPS1-21 mice

To acquire a deeper view of astrocytic changes related to Aβ pathology on a functional level, I performed Ca^{2+} imaging experiments. Ca^{2+} signalling in astrocytes is a common readout to determine altered cellular functions which should help to understand cellular responses linked to disease, behaviour, or even to study the role of specific proteins (Volterra et al. 2014). In the past, several studies were able to uncover cellular mechanisms in astrocyte physiology and diseases by decoding Ca^{2+} transients in astrocytes and thereby studying consequences of their activation (Khakh und Sofroniew 2015; Shigetomi et al. 2016; Hill et al. 2014). Studies in AD mouse models demonstrated under different conditions an increased activity of cortical and hippocampal astrocytes (Kuchibhotla et al. 2009; Delekate et al. 2014; Reichenbach et al. 2018). However, the previous studies featured specific limitations and influencing factors that need to be considered. For example, the experimental setup for Ca^{2+} imaging in astrocytes is an important factor when interpreting Ca^{2+} imaging data (Bindocci et al. 2017). Thus, whereas astrocytes in cell culture lack the physiological tissue environment, acute imaging approaches were already a critical step towards studying astrocytes in their normal cellular network. However, the injection of the commonly used organic Ca^{2+} indicators into the tissue followed by the cranial window implantation required anaesthesia. The surgical insult as well as anaesthesia have been shown to strongly affect the astrocytic Ca^{2+} response (Thrane et al. 2012; Goldey et al. 2014). In later studies, the tissue damage and the induced astrocyte reactivity by the cranial window surgery were overcome by injecting a GECI intracranially and by a certain recovery time after window implantation (Shigetomi et al. 2016). During recovery, the tissue has time to regenerate and return to a normal physiological condition. With the recently achieved possibility to image on a two-photon microscope in combination with a linear treadmill, imaging of awake behaving mice has become possible, which solves the influencing issue by anaesthesia. The remaining issue has been related to the fact that the GECI-encoding virus had to be injected into the brain region, inducing local tissue damage and astrogliosis and restricting imaging to the area near the injection site (Figure 2-9). Therefore, the procedure was further improved with an injection of an AAV that features a BBB permeability (Chan et al. 2017), which I used in my experiments. This AAV enabled the transduction of a high fraction of astrocytes in the entire brain by a single dosed application through the retro-orbital intravenous injection (Figure 2-12B). This improvement drastically reduced astrogliosis and facilitated a transgene integration without disrupting the normal tissue organization in the cortex (Figure 2-9).

Imaging cortical astrocytes is additionally challenging due to their low baseline activity, resulting in very sparse and low Ca^{2+} transients if recorded in a resting or anaesthetized mouse without

external stimuli. To enable an appropriate detection to record the baseline activity of cortical astrocytes also in a resting condition, a suitable analysis tool is important. Analysing Ca^{2+} dynamics from astrocytes is highly demanding and has become a hot topic in astrocyte research. Due to the highly dynamic diverse Ca^{2+} signals (Figure 2-13) within these very morphologically complex cells, many different approaches were developed lately, which usually are best suitable for one specific experimental setup or scientific question (Agarwal et al. 2017; Wang et al. 2019). Conclusively, how to analyse the Ca^{2+} transients needs to be considered by individual needs and specifications. The tool developed in my study was to detect individual active regions within the single astrocytes in one field of view. The classical Ca^{2+} analysis in the past was based on a whole cellular response in the soma with one defined region of interest (ROI) for each individual astrocyte (Kuchibhotla et al. 2009; Delekate et al. 2014; Reichenbach et al. 2018). In comparison, the analysis tool used in my analyses was not based on the whole cellular response, but detected the active domains within each imaged astrocyte, representing a significant advantage over whole-astrocyte analysis approaches. Moreover, my analysis suite also allowed for an unbiased semi-automated detection of the Ca^{2+} kinetics and the frequency of events with the resolution of single active domains (Figure 2-14), which again represents a significant advantage over previous methods that relied on manual or subjective detection.

The synchronized recordings of the locomotor behaviour and the Ca^{2+} signals revealed a simultaneous activation of the active domains within the individual astrocyte with a heightened fluorescent intensity during locomotion (Figure 2-15B). Where Ca^{2+} transients during rest were nearly not visible by eye, the fluorescent intensity was clearly visible as a broad Ca^{2+} signal during locomotion (Figure 2-13, 14). Analysing the kinetic features of Ca^{2+} transients in rest compared to locomotion showed that the Ca^{2+} transients last longer during locomotion (Figure 2-16B). This was particularly apparent when using the fast imaging setup, indicating that a temporal resolution of >40 Hz is necessary to capture the full spectrum of astrocytic signals in future studies. This is in line with recent studies that have identified very fast stimulus-evoked astrocytic responses (Volterra et al. 2014; Stobart et al. 2018a; Schipke et al. 2008).

The locomotion-triggered Ca^{2+} elevations are induced specifically by the release of NE from the neuronal projections of the LC (Bekar et al. 2008). This release is initiated by a vigilant or arousal state and mediated by α1-ARs on astrocytes. This adrenergic response was demonstrated for cortical astrocytes and Bergmann glia (Ding et al. 2013; Paukert et al. 2014). Previous studies from our lab showed an increased hyperactivity of cortical astrocytes in APPPS1-21 mice by using the acute approach with the mentioned drawbacks (Delekate et al. 2014). However, hippocampal astrocytes showed also an increased activity using GCaMP6f in anaesthetized APPPS1-21 mice (Reichenbach et al. 2018). Both studies demonstrated a dependency of this spontaneous activity on purinergic signalling via the purinoreceptor P2y1 expressed by astrocytes. Similar to α1-ARs,

P2y1 receptor is a G_q-coupled receptor and thereby activates the Ca^{2+} release from intracellular stores via the IP_3 dependent pathway. Chronic inhibition of this pathway normalized the elevated Ca^{2+} activity in astrocytes, as well as astrocyte-neuronal network activity and spatial learning and memory deficits in APPPS1-21 mice (Delekate et al. 2014; Reichenbach et al. 2018). However, these studies were performed in anaesthetized mice, and consequently the Ca^{2+} response to NE release could not be studied under these conditions due to the requirement of wakefulness for NE signalling.

While the active region or the size of the active domains were not significantly different between wild type and APPPS1-21 mice in my study (Figure 2-18), the frequency of Ca^{2+} events was significantly higher in APPPS1-21 mice, suggesting an increased activity in astrocytic active domains (Figure 2-19B). Moreover, in both genotypes the activity was significantly higher during locomotion compared to resting condition. Due to the previously reported NE-induced locomotor activity and the recorded astrocyte response, this strongly suggests that the increased astrocytic response during locomotion in APPPS1-21 mice is mediated by the increased expression of α1-ARs in astrocytes identified in my translatome analysis. Moreover, APPPS1-21 mice also showed a higher Ca^{2+} signal frequency under resting conditions, pointing to an additional NE-independent Ca^{2+} elevation, potentially by P2y1-mediated pathway. In line with this, my RNAseq data also identified several other genes involved in Ca^{2+} signalling pathways that may be addressed in future studies.

4 Conclusions and future perspectives

The focus of this study was to uncover Aβ pathology-initiated alterations in the translatome of astrocytes during disease progression compared to aging. These analyses revealed upregulations in pathways linked to Ca^{2+} signalling that are essential for a normal physiological function of astrocytes (Agulhon et al. 2008). The upregulation of this group of genes serves as a molecular framework for the increased astrocytic Ca^{2+} signals observed *in vivo* in mouse models of AD. The increased expression of two different α1-ARs in cortical astrocytes and the increased locomotion-triggered Ca^{2+} response in APPPS1-21 mice suggest that the astrocyte-neuron network dysfunction observed in different AD models may in part be related to dysregulation of the noradrenergic system (Kjaerby et al. 2017). In future studies, it will be important to verify this hypothesis by manipulating α1-ARs specifically in astrocytes, using genetic knock-out or knock-down techniques. In particular, these experiments could establish which effects are mediated by direct activation of astrocytes by the LC or indirect effects mediated by neighbouring cortical neurons activated by the LC. Recently, a newly developed noradrenalin (NA) sensor enabled the visualization of extracellular NA released in response to LC stimulation and demonstrated the initiation of large cytosolic Ca^{2+} transients in astrocytes (Oe et al. 2020a) similar to our observed responses triggered by locomotion. Furthermore, different currently available NA/NE fluorescent sensors can be used for *in vivo* studies to correlate the NA/NE release with the Ca^{2+} response in astrocytes in AD mouse models (Oe et al. 2020a; Feng et al. 2019). Another possibility is the stimulation of LC neurons expressing the photoactivatable receptor channelrhodopsin and the simultaneous recording of astrocytic Ca^{2+} response with additional inhibition of the release from local NTs such as glutamate. With the continuously advancing state-of-the-art techniques, increasing knowledge of astrocyte functions in their specialized neural circuits will also result in a better understanding of how astrocytic signalling shapes neuronal activity.

Overall, identifying new astrocytic targets by transcriptome analysis, and verifying their role through functional imaging studies and behavioural analyses, holds great promise to develop novel AD treatment strategies (Verkhratsky et al. 2010).

5 Material & Methods

5.1 Genetically modified mouse lines, genotyping, and husbandry

5.1.1 Mouse lines

Transgenic mouse lines and their references are listed in Table 5-1.

Rpl22$^{tm1.1Psam}$ (RiboTag) mice were generated by inserting a transgene containing the endogenous floxed exon4 of the *Rpl22* gene, followed downstream by a recombinant exon4 carrying 3 sequence repeats encoding the hemagglutinin eptiope (HA) upstream of the endogenous stop codon. By cross breeding with Gja1$^{tm5(cre/ERT)Kwi}$ (Cx43$^{Cre-ER(T)}$) mice, the astrocyte-specific connexin 43 (Cx43) promoter induced the Cre recombinase expression upon tamoxifen injection thereby leading to the recombination of RiboTag transgene. This transgene combination results in an astrocyte-specific expression of Rpl22 tagged with HA epitope. The generated Cx43$^{Cre-ER(T)}$/RiboTag mouse line was crossbred with the double transgenic AD mouse model Tg(APPswe,PSEN1dE9)85Dbo (APPswe/PS1dE9). The APPswe/PS1dE9 mice express a chimeric human/mouse amyloid precursor protein (APP) with the specific Swedish mutations Mo/HuAPPK594M/N595L and a truncated form of PS1 with a deletion of exon 9 (HuPS1-dE9) under the mouse prion protein promoter (PrP). APPswe/PS1dE9 animals are developing amyloidosis and thereby Aβ plaques at an age of around 6 months accompanied with increased $A\beta_{42}$ levels (Jankowsky et al. 2001). The resulting animals from the crossing of the APPswe/PS1dE9 line with Cx43$^{Cre-ER(T)}$/RiboTag mice were utilized for the transcriptome analysis, comparing gene expression profiles of 4, 8, and 12 months old mice to identify Alzheimer's disease specific changes in gene expression. In this study APPswe/PS1dE9 line with Cx43$^{Cre-ER(T)}$/RiboTag mice are simplified as APP/PS1 mice and Cx43$^{Cre-ER(T)}$/RiboTag as wild type mice.

Tg(Thy1-APPSw,Thy1-PSEN1*L166P)21Jckr (APPPS1-21) mice were generated by the insertion of the human APP mutations APPKM670/671NL and mutant human presinilin1 (PS1) with a specific exchange of leucin to proline at amino acid position 166. Both human genes were placed downstream of the neuron-specific murine Thy1 promoter region. These mutations lead to an early onset of amyloidosis by increasing the amyloid β (Aβ) production at the age of 6-8 weeks especially in the cortex with the specific elevation of $A\beta_{42}$ (Radde et al. 2006). APPPS1-21 mice were utilized to study cortical astrocyte Ca^{2+} signalling in awake mice in a longitudinally fashion at an age of 5-8 months. Control animals were wild type littermates from the APPPS1-21 mouse line.

Table 5-1 Transgenic mouse lines and references.

Mouse line	Background	Generated by	References	MGI
RiboTag	C57Bl/6N	Paul S Amieux	Sanz E, et al., 2009 (Sanz et al. 2009)	MGI:4355967
Cx43$^{Cre-ER(T)}$	C57Bl/6N	Klaus Willecke	Kretz M, et al., 2003 (Kretz et al. 2003)	MGI:2676327
APP$_{swe}$/PS1dE9	C57Bl/6N	David R Borchelt	Jankowsky JL, et al., 2001(Jankowsky et al. 2001)	MGI:3524957
APPPS1-21	C57Bl/6J	Mathias Jucker	Radde R, et al., 2006 (Radde et al. 2006)	MGI:3765351

5.1.2 Genotyping

Genomic DNA was isolated from ear biopsies by using the DirectPCR Lysis Reagent Tail (Viagen #102-T) and Proteinase K (20 mg/ml) to lyse the tissue according to the manufacturer's instructions. The PCR reactions were performed using the C1000 Thermal Cycler (Bio-Rad). Primers were provided by Eurofins MWG.

5.1.2.1 RiboTag

Fragments: 260 bp for wild type and 290 bp for mutant allele

Table 5-2 Genotyping primer for RiboTag

Name	Sequence 5' to 3'	Tm (°C)
Forward	GGG AGG CTT GCT GGA TAT G	63
Reverse	TTT CCA GAC ACA GGC TAA GTA CAC	65

Table 5-3 PCR reaction mix for RiboTag genotyping

Reagent/Solution	Volume (µl)	Concentration
10x PCR buffer (Invitrogen)	2	1x
MgCl2	0.8	2 µM
dNTPs (Thermo Fisher Scientific, #10297018)	0.4	0.2 µM
Forward primer	1	1 µM
Reverse Primer	1	1 µM
Platinum Taq (Invitrogen, #10966-018)	0.1	2 U/reaction
Template DNA	2	
Total reaction mix	20	

Table 5-4 PCR program for RiboTag genotyping

Step	Temperature (°C)	Time (s)	Repeats
Denaturation	94	180	1x
Denaturation	94	30	35x
Hybridization	64	30	
Elongation	72	30	
Elongation	72	120	1x
Cooling	4	∞	∞

5.1.2.2 Cx43Cre-ER(T)

Fragments: 324 bp for wild type and 100 bp for Cre allele

Table 5-5 Genotyping primer for Cre

Name	Sequence 5' to 3'	Tm (°C)
Forward	GCGGTCTGGCAGTAAAAACTATC	60
Reverse	GTGAAACAGCATTGCTGTCACTT	60
IPC forward	CTAGGCCACAGAATTGAAAGATCT	59
IPC reverse	GTAGGTGGAAATTCTAGCATCATCC	59

Table 5-6 PCR reaction mix for Cre genotyping

Reagent/Solution	Volume (µl)	Concentration
10x CoralLoad Concentrate (Qiagen)	2.5	1
Forward primer	1	0.8 µM
Reverse Primer	1	0.8 µM
IPC forward primer	0.8	0.6 µM
IPC reverse primer	0.8	0.6 µM
Hot Star Taq Master Mix (Qiagen, #203645)	12.5	
Template DNA	0.5	
Total reaction mix	25	

Table 5-7 PCR program for Cre genotyping

Step	Temperature (°C)	Time (s)	Repeats
Denaturation	94	180	1x
Denaturation	94	30	35x
Hybridization	51.7	60	
Elongation	72	60	
Elongation	72	120	1x
Cooling	4	∞	∞

5.1.2.3 APPswe/PS1dE9

Fragments: 324 bp for wild type and 608 bp for PS1dE9 allele

Table 5-8 Genotyping primer for PS1dE9 mutant

Name	Sequence 5' to 3'	Tm (°C)
Forward	AATAGAGAACGGCAGGAGCA	59
Reverse	GCCATGAGGGCACTAATCAT	58
IPC forward	CTAGGCCACAGAATTGAAAGATCT	59
IPC reverse	GTAGGTGGAAATTCTAGCATCATCC	59

Table 5-9 PCR reaction mix for APPswe/PS1dE9 genotyping

Reagent/Solution	Volume (µl)	Concentration
10x CoralLoad Concentrate (Qiagen)	2.5	1
Forward primer	1	0.8 µM
Reverse Primer	1	0.8 µM
IPC forward primer	0.8	0.6 µM
IPC reverse primer	0.8	0.6 µM
Hot Star Taq Master Mix (Qiagen, #203645)	12.5	
Template DNA	0.5	
Total reaction mix	25	

Table 5-10 PCR program for APPswe/PS1dE9 genotyping

Step	Temperature (°C)	Time (s)	Repeats
Denaturation	94	180	1x
Denaturation	94	30	35x
Hybridization	54	60	
Elongation	72	60	
Elongation	72	120	1x
Cooling	4	∞	∞

5.1.2.4 APPPS1-21

Fragments: 427 bp for wild type and 246 bp for APP mutant allele

Table 5-11 Genotyping primer for APP mutant

Name	Sequence 5' to 3'	Tm (°C)
Forward	GAATTCCGACATGACTCAGG	56
Reverse	GTTCTGCTGCATCTTGGACA	58
IPC forward	CCTCATGAAGATCCTGACCG	58
IPC reverse	GCACTGTGTTGGCATAGAGG	59

Table 5-12 PCR reaction mix for APPPS1-21 genotyping

Reagent/Solution	Volume (µl)	Concentration
10x CoralLoad Concentrate (Qiagen)	2.5	1
Forward primer	1	0.8 µM
Reverse Primer	1	0.8 µM
IPC forward primer	0.8	0.6 µM
IPC reverse primer	0.8	0.6 µM
Hot Star Taq Master Mix (Qiagen, #203645)	12.5	
Template DNA	0.5	
Total reaction mix	25	

Table 5-13 PCR program for APPPS1-21 genotyping

Step	Temperature (°C)	Time (s)	Repeats
Denaturation	94	180	1x
Denaturation	94	30	35x
Hybridization	54	60	
Elongation	72	60	
Elongation	72	120	1x
Cooling	4	∞	∞

5.1.3 Husbandry

Mice were group-housed with one to five mice per individually ventilated cages (IVCs, TECNIPLAST) with free access to acidified tap water and food (ssniff®, ssniff Spezialdiäten). The light/dark cycle was 12/12 h and mice were kept under specific pathogen-free conditions (SPF). The temperature was constantly kept at 22°C with 40% relative humidity (RH). Experiments were performed according to institutional animal welfare guidelines and were previously approved by the State Agency for Nature, Environment and Consumer Protection (LANUV) of North Rhine-Westphalia, Germany.

5.1.4 Genetic modification via virus transduction

5.1.4.1 Virus

Conditional expression of the genetically encoded Ca^{2+} indicator GCaMP6f under the short GFAP promoter (sGFAP or gfaABC1D)

Table 5-14 Adeno-associates viruses

Virus	Company/Donor
AAV2/5-gfaABC1D-cyto-GCaMP6f (Haustein et al. 2014)	Addgene
AAV.PHPeB-sGFAP-cyto-GCaMP6f	Sirion-Biotech/ Gilles Bonvento (I2BM)

5.2 Surgical procedures and treatments

5.2.1 Stereotactic microinjections

Before the surgical intervention, all surgical tools (Fine Science Tools) were sterilized in a hot bead sterilizer (FST). The working space and the stereotactic frame (David Kopf Instruments) were cleaned with 70 % Ethanol. Mice were weighed and according to the body mass subcutaneously injected (s.c) with the analgesic drug Buprenorphine (0.1 mg/kg animal; Reckitt Benckiser Healthcare, #PZN 00345928) and the anti-inflammatory drug Dexamethasone (0.2 mg/kg animal; Sigma, #D1159) 20 min prior to surgery. Anaesthesia was initiated with 3 % Isoflurane (Baxter, #PZN6497131) with 1 L/min oxygen, while during surgery anaesthesia was reduced to 1.0-1.5 % Isoflurane. The depth of the anaesthesia was constantly checked during the whole procedure by pinch-withdrawal reflex on the hind limb of the mouse. Before the mouse was placed into the surgical frame, the head was shaved (Moser Chromini Pro) to minimize loose irritating hair entering the wound during surgery. By using a heat-pad (npi electronics), body temperature was controlled and kept at 37-38°C. Eyes were covered with Bepanthen eye ointment (Bayer, #PNZ 01578681) to prevent drying. The surgery was conducted under visual control through a stereomicroscope (Zeiss) and a cold light source (Zeiss). The mouse head was fixed with ear bars in the stereotactic frame with an additional microinjection unit and orientated planar for the stereotactic injection. Subsequently, the head was cleaned with 70% ethanol and additional local anaesthesia was administered above the skull by s.c. injection of Xylocitin® (lidocain hydro chloride2% with 0.001% epinephrine hydrogen tartrate, 50-100 µl. After 5 min, a longitudinal incision (approx. 1.5 cm) with a scalpel was performed to expose the skull above the cortex. The skull and edges of the skin were cleaned with a scalpel (Swann-Morton, #0505), forceps, and cotton buds (deltalab, #300202) by removing loose hair, blood and connective tissue. The injection hole was drilled using a dental drill (Komet Dental, #800745) over the somatosensory cortex with the coordinates 1.8 mm posterior and 1.5 mm lateral from bregma. The injection glass capillary (pulled with a vertical puller, Narishige) was mounted on the microinjection unit, filled with the AAV2/5-gfaABC1D-cyto-GCaMP6f virus (approx. $5x10^{10}$ vg) and was inserted in the hole with a depth of 200 µm from the brain surface. Next, 1 µl of the AAV was injected with an injection speed of 100 nl/min using a microinjection pump (WPI) afterwards the capillary was kept at the injection position for another 10 min. After removing the glass capillary, the wound was cleaned with saline (0.9 % NaCl; B Braun, #350720) and the skin sewed with sutures (B Braun, #XC29.1). The mouse was transferred to a recovery chamber (VetTech) warmed at 37°C, after waking up the animal was placed into a fresh home cage.

5.2.2 Retro-orbital virus injection

The mice were injected s.c. according to their body weight with the analgesic drug Buprenorphine (0.1 mg/kg animal) 20 min before retro-orbital AAV injection. Anaesthesia was initiated with 3 % Isoflurane with (1 L/min oxygen) and further kept at 1.0-1.5 % Isoflurane during the procedure. AAV.PHPeB.sGFAP.cyto-GCaMP6f was diluted with sterile saline (0.9 % NaCl, B Braun, #350720) to a virus concentration of 1x1011 vg/50 µl. By using a heat-pad, body temperature was controlled and kept at 37-38°C. Eyes were covered with Bepanthen eye ointment to prevent drying. The mouse was placed in left lateral recumbency with its head facing right. By applying gentle pressure on the skin dorsal and ventral from the eye the eyeball is protruding for approx. 1-2 mm. As a local anaesthesia one drop of 1 % Xylocitin® was applied directly on the eye. A 33-gauge syringe (B Braun, #5427807) was filled with 50 µl of the diluted virus and the needle was introduced in a 30° angel into the media canthus and thereby into the retro-orbital sinus. The bevel of the needle was positioned to face down (Figure 5-1) to reduce the probability of damaging the eye. Subsequently, virus solution was slowly injected, and the mouse was transferred into a recovery chamber at 37°C, to allow for waking up under warm condition. The procedure was adopted as described by Yardeni et al. 2011 (Yardeni et al. 2011).

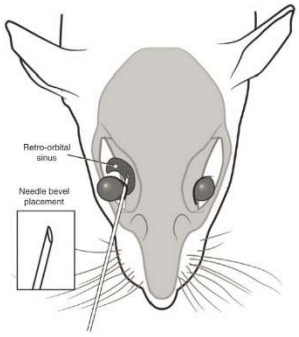

Figure 5-1 Correct placement of the needle relative to the retro-orbital sinus, the eyeball and the back of the orbit. Illustration by Darryl Leja. (Yardeni et al. 2011)

5.2.3 Chronic cranial window implantation

Two weeks after AAV injection either performed by stereotactic microinjection or retro-orbital injection, a chronic cranial window was implanted. The pre-surgical preparations, drug administration and the conditions for the anaesthesia were the same as for the stereotactic microinjection including the Xylocitin® injection. Subsequently, the scalp was removed, and the skull and edges of the skin were cleaned with a scalpel, forceps, and cotton buds by removing loose hair, blood and connective tissue. To ensure the stability of the later fixation with the UV light-cured dental cement, the skull was dried and prepared by coating with a two-component dental adhesive (OptiBond, FL, Kerr, # 26684E). First, a thin layer of the priming component was applied with a light brushing motion for 15 s and air dried for 5 s. The coating with the adhesive component was performed likewise, finalized by crosslinking both components with UV light (LED smart plus, Smart'n easy) for 20 s. Next, the position for the cranial window was marked with a ø 4 mm biopsy punch (pfm medical, #0197) above the right somatosensory cortex with the coordinates 1.8 mm posterior and 1.5 mm lateral from bregma at the centre of the window. By using a dental drill, the ø 4 mm craniotomy was produced, and the skull piece was carefully removed without injuring the dura. After cleaning the craniotomy with sterile saline (0.9 % NaCl), a glass coverslip was precisely fitted into the craniotomy. Next, the coverslip was pre-fixed with superglue (Henkel, #Loctite), followed by permanent fixation using the UV light-cured dental cement (Gradia Direct Flo, GC Europe, #36500). In addition, a stainless-steel head-holder (dovetail headpost holder, Luigs and Neumann) was placed and fixed on the contralateral site of the skull. The remaining exposed skull was completely covered with the UV light-cured dental cement, thereby also sealing the skin wound at the edges. Finally, to prevent infections the mouse received one dose of the antibiotic drug Cefotaxime sodium salt (2 g/kg animal; Thermo Fisher Scientific) and was transferred to a recovery chamber at 37°C, to allow for waking up under warm condition.

5.2.4 Post-surgical care

After the stereotactic microinjections and chronic cranial window implantations, mice received one dose of Buprenorphine (0.1 mg/kg animal) for 3 days every 8 hours.

5.2.5 Tamoxifen treatment

Tamoxifen (Sigma, #T5648) was administered with intraperitoneal injections for 5 days with 5 µl/g body mass with an emulsion of 20 mg/ml tamoxifen in sunflower oil:ethanol mix (10% ethanol). Sunflower oil was acquired from Sigma (Sigma, #47123). Three weeks post-injection, mice were sacrificed, and brains were snap-frozen in liquid nitrogen for the later RNA isolation.

5.3 Astrocytic Ca^{2+} imaging in awake mice

The two-photon imaging technique uses the physical principle of the excitation of fluorophores with the approx. doubled wavelength compared to the conventional excitation wavelength in one-photon microscopy. The used longer wavelength in the near infrared spectrum, leads to an improved tissue penetration, low phototoxicity and reduced light scattering. These characteristics of two-photon microscopy facilitated the visualization of biological processes and structures in living animals (Belluscio 2005). In this study, a two-photon microscope in combination with a linear treadmill was used to visualize Ca^{2+} signals in cortical astrocytes in response to locomotion and resting behaviour.

5.3.1 Habituation to the linear treadmill

Before starting the awake imaging experiments, each mouse was habituated to the linear treadmill (Luigs and Neumann) for 1 hour on at least 3 consecutive days. Therefore, the previously implanted head-holder allowed for the head-fixation of the mice on the linear treadmill that was equipped with a two-meter belt. As soon as the mice were able to run in an appropriate way with reduced stress levels, they were well habituated for the imaging experiments.

5.3.2 Two-photon Ca^{2+}imaging of cortical astrocytes

Head-fixed mice with a chronic cortical window, expressing GCaMP6f specifically in astrocytes were imaged awake, while they were running on a linear treadmill. The locomotion behaviour was recorded by using an optical computer mouse to read out the position of the belt (Luigs and Neumann). The start of the recorded belt position was triggered by the start of the microscope scanner and was controlled by using a customized Python 2.7 (Python Software Foundation, Delaware, USA) script. The temporal synchronization of the different hardware components was operated using an ITC-18 board (HEKA Instruments Inc., Bellmore, USA) and the IGOR Pro software (WaveMetrics Inc., Portland, USA).

Astrocytic Ca^{2+} changes were recorded in a time series of 5 min using two different upright two-photon microscopes, equipped with a 16x water immersion objective with a numerical aperture of 0.8 (N16XLWD-PF, Nikon). Fluorophores were excited with a wavelength of 920 nm at a depth of 100-200 µm beneath the cortical surface. To prevent phototoxicity, laser power was kept between 20 to 40 mW below the objective.

For the visualization of blood vessels, which were used as landmarks during longitudinal imaging, mice were injected s.c. with 50 µl, Texas Red Dextran 3000 MW (10 mg/ml in saline; Life Technologies, #D3328) prior to each imaging session.

5.3.4 Two-photon microscope setup specification

For imaging performed with the SP8 DIVE (Deep In Vivo Imager) microscope from Leica, Ca^{2+} changes were recorded at a frequency of 3.82 Hz (256x256 µm; 256 px) using a galvo scanner. GCaMP6f emission was detected by using hybrid detectors (HyD) with two filters (500/550,560/620 nm) and excited by using a Spectra Physics InSight DS+ laser. Leica LAS X software was used to control image acquisition. With the custom-made Thorlabs two-photon microscope Ca^{2+} changes were recorded at a frequency of 14.8 Hz (59.19 Hz four times averaged; 256x256 µm; 256 px) using a galvo-resonant scanner (Thorlabs). GCaMP6f emission was detected by using a band-pass filter (525/50, AHF) and a GaAsP PMT (Thorlabs) and excited by using a titanium sapphire (Ti:Sa) 80 MHz Cameleon Ultra II two-photon laser (Coherent). ThorImageLS software (Thorlabs, version 2.1) was used to control image acquisition.

5.4 Analysis of time series

5.4.1 Raw data processing, segmentation, and data extraction

Motion correction was performed on all recorded time series to remove motion-induced artifacts. Time series were computed by using a combination of efficient subpixel registration and in-frame motion correction with the Lucas-Kanade method (Lucas und Kanade 1981; Guizar-Sicairos et al. 2008) using MATLAB R2018a (MathWorks). To distinguish Ca^{2+} transients during locomotion or rest, time series were segmented to image series during each specific behavioural state. Mouse activity was either estimated by visually studying the time series to estimate the active period (slow imaging setup) or with the recorded synchronized position read out (fast imaging setup).

Active domain identification and extraction was performed by using a custom-written macro in Fiji (version 2.0.0-rc-69/1.52p) (Schindelin et al. 2012). First, to smooth the image series the noise was removed by 3D convolution using a small Gaussian-filter (1 x 1 x 1 pixels (x, y, z)). Secondly, a large Gaussian-filter (20 x 20 x3 pixel (x, y, z)) was applied to reduce the background noise followed by its subtraction from the smoothed image series. Next, the filtered image series was processed by maximum 2D projection along the time axis which was utilized to define regions of interest (ROIs) after thresholding with the "Li" threshold method (Li und Lee 1993) provided in Fiji. Finally, a ROI-map, representing the active domains with Ca^{2+} elevation, was generated by the definition of detected maxima with a minimal size of 5 x 5 pixels. The generated output was a data table with the mean intensity values over time for each defined ROI (active domain). The used macro was based on the CaSCaDe algorithm published by Agarwal et al. 2017 (Agarwal et al. 2017) and was modified to this research project.

5.4.2 Ca^{2+} peak detection analysis

The detection of Ca^{2+} peaks from the generated mean intensity data of the defined active domains was performed using a supervised machine learning approach that was implemented with a support vector machines algorithm (from the scikit-learn library). The output table from the data extraction was used as input. Peak candidates were identified by normalizing the data to robust z-score followed by a Gaussian filtering of $2*\sigma$ and a threshold of 2-fold change of intensity in an analysis window width of 55 frames from the time series. Next, the algorithm was taught manually on the basis of the peak profile to distinguish between invalid and valid Ca^{2+} peaks. After a training session with a representative data set, a classifier was saved and was used for all following Ca^{2+}peak detections in an unbiased fashion. The resulting data output includes the raw, normalized, and smoothed fluorescent intensity values and the corresponding kymographs of all active domains as well as the peak kinetics for all detected valid peaks, like amplitude, full duration at half maximum, mean increase of the slope from analysis window start to peak maximum (rise time) and mean decrease of the slope from peak maximum to analysis window end (decay time). The frequency of Ca^{2+} events was determined by the number of valid events detected in one image series (field of view, (FOV)), divided by the length in seconds of the specified image series.

In addition, using another custom-made macro in Fiji, a mask was created, fractioning the analysed area of the FOV to the regions where active cells were noticeable in sum projections of the time series. This facilitates further the exclusion of false positive event detection due to auto fluorescent particles in the FOV.

5.5 Translatome purification with RiboTag

Seven days after Cre recombinase activation by tamoxifen injection, brains from Cx43$^{CreER(T)}$; RiboTag$^{+/-}$; APP/PS1$^{+/-}$ or $^{-/-}$ mice were collected at 4, 8, and 12 months of age. Before brains were frozen in liquid nitrogen, the olfactory bulb and the cerebellum were removed, and brain hemispheres were snap-frozen separately. The purification protocol was based on the publication from Elisenda Sanz and colleagues (Sanz et al. 2009) with slight modifications.

5.5.1 Co-immunoprecipitation of mRNA

For the preparation of a 10 % homogenate, brain tissue was weighed and homogenized with the corresponding volume (1 ml PSB/0.1 g tissue) of polysome buffer (PSB, Table 5-15) using a 5 ml Teflon-glass (Potter-Elvehjem) homogenizer with a motorized device. Frozen tissue was transferred to the homogenizer followed by the addition of ice cold PSB buffer with subsequent homogenization by a steering speed of 450 rpm and a up and down motion of the pestle for around 1 min. Next, the homogenate was centrifuged by 10,000 g for 30 min at 4°C and the supernatant (S1) was separated from the pellet. S1, containing the polysomes, was used as input for the immunoprecipitation. Subsequently, 100 µl of S1 were added to 700 µl QIAzole (Qiagen, #79306) serving as input sample as well as a total mRNA sample including mRNA from all cells. Further, 1300 µl S1 were pre-cleared by 30 min incubation with 75 µl Protein G Dynabeads (PGDB; Life Technologies, #10004D) at 4°C on a rotor for gentle mixing. PGDB were previously washed two times with PBS followed by equilibration with PSB. After pre-clearing, reaction tubes (Roth, #4182,1) were placed in an ice-cold magnetic rack (DynaMag-2, Thermo Fischer Scientific) and after PGDB adhered to the tube wall, S1 was transferred in a tube containing the anti-HA antibody (12 µl/ 300 µl S1;12CA5, Sigma, #11583816001). To enable anti-HA antibody binding to the HA-tagged polysomes, S1-antibody mixture was incubated for 45 min at 4°C with gentle mixing. For the pull-down of the HA-tagged polysomes, the S1-antibody mixture was added to fresh PSB equilibrated 75 µl PGDB with further 80 min incubation under gentle mixing at 4°C. Subsequently, the tubes were placed in an ice-cold magnetic rack and the supernatant was discarded. PGDB were washed three times with 500 µl high salt buffer (HBS, Table 5-15) and three times with 500 µl extra high salt buffer (EHSB, Table 5-15), each washing step was performed by gentle mixing on a rotator at 4°C for 5 min. In the last washing step samples were split into two, to create a technical replicate. Elution of the polysomes was facilitated by mixing PGDB with 700 µl QIAzole at room temperature (RT) for 15 min on an Eppendorf mixer at 1400 rpm.

Table 5-15 Buffers for the co-immunoprecipitation of mRNA

Buffer	Reagent	Final concentration
Polysome buffer (PSB)	Tris, pH 7.5	50 mM
	KCl	100 mM
	MgCl2	12 mM
	Nonident P-40	1%
	DTT	1 mM
	RNase Inhibitor (Life Technologies, #EO0382)	3.75 µl/ml
	Cyclohexamide	100 µg/ml
	Protease inhibitor (Sigma, #C7698)	2x
	Phosphatase inhibitor (Sigma, #4906845001)	1x
High salt buffer (HBS)	Tris, pH 7.5	50 mM
	KCl	300 mM
	MgCl2	12 mM
	Nonident P-40	1%
	DTT	1 mM
	RNase Inhibitor	1.25 µl/ml
	Cyclohexamide	10 µg/ml
	Protease inhibitor	0.5x
	Phosphatase inhibitor	1x
Extra high salt buffer (EHBS)	Tris, pH 7.5	50 mM
	KCl	300 mM
	NaCl	300 mM
	MgCl2	12 mM
	Nonident P-40	1%
	DTT	1 mM
	RNase Inhibitor	1.25 µl/ml
	Cyclohexamide	10 µg/ml
	Protease inhibitor	0.5x
	Phosphatase inhibitor	1x

5.5.2 RNA extraction

As described above 700 µl QIAzole was added to samples of total mRNA and the immunoprecipitated sample (RiboTag mRNA). After the addition of 140 µl chloroform, each sample was extensively vortexed for >15 s. with following 2-3 min incubation at RT. To facilitate a clear separation of the three different phases samples were centrifuged at 4°C for 15 min at 13,000 g. The aqueous upper phase was transferred into a fresh tube and the containing RNA was precipitated by adding 1.5-fold the sample volume of 100% ethanol to each sample. For further purification, the Qiagen RNeasy kit (Qiagen, #74134) was used with slight modifications and that were performed at RT. The ethanol-sample mixture was loaded to the RNeasyMinElute spin column and centrifuged for 15 s with 9000 g. From this step on the procedure was performed by following the instructions of the kit. Finally, purified RNA was eluted from the column with appropriate volumes of RNA free water. Samples for total RNA were eluted with 60 µl and RiboTag samples with 14 µl RNA free water.

5.5.3 Photometric determination of RNA concentration

The concentration of RNA was measured with a Nanodrop 2000 (Thermo Fisher Scientific) system using 1 µl aqua bidest as blank and 1 µl of the sample for the measurement.

5.5.4 RNA quality control

To determine the RNA quality to estimate the level of degradation, the RNA integrity number (RIN) was measured in the Agilent 2100 Bioanalyzer in combination with the Agilent RNA 6000 pico Kit (Agilent Technologies, #5067-1513) by following the manufacturer's instructions.

5.6 Multiplex fluorescent RNAscope *in situ* hybridization

Multifluorescent RNAscope (Advanced Cell Diagnostics, #320850) *in situ* hybridization was performed using probes for Sox9, Adra1a, Adra1d, and Gfap (Mm-Sox9-C3 #563571-C3, Mm-Adra1a-C1 #408611, Mm-Adra1d-C1 #563571 and Mm-Gfap-C2 #313211-C2) according to the manufacturer's instructions. Therefore, APP/PS1 mice (APPPS1-21) with 7 months of age were transcardially perfused by using 20 ml ice-cold sterile 0.9% NaCl. Subsequently, the brain was removed and embedded in OCT embedding medium (Fisher Scientific, #12678646) and quickly frozen by using 2-Methylbutane pre-cooled on dry ice. Frozen brains were stored at -80°C until sectioning at -20°C using a Cryostat (CryoStar NX70, Thermo Fisher Scientific). The 20 µm coronal brain sections were directly transferred to coated glass slides (Superfrost plus, Thermo Fisher Scientific, #10149870) and stored at -80°C until usage. The following procedure was performed according to the manufacturer's instructions with time and temperature specifications described in Table 5-16. In amplification step 4 Amp Alt-4C used a C1 probe labelled with Atto 550, a C2 probe with Atto 647 and C3 probe with Atto 488 fluorophores. To determine the background fluorescent of the Amp Alt-4C, a 3-plex negative control probe was applied on one section. To check for the RNA integrity in the used tissue, 3-plex positive control specific for mouse tissue was applied on another section. The incubation steps for the RNAscope procedure are described in Table 5-16.

Table 5-16 Incubation steps for the RNAscope procedure.

Step	Reagent	Time (min)	Temperature
Wash	PBS	5	Ice-cold
Fixation	4% PFA (Sigma, #P6148)	20	Ice-cold
Wash	2xPBS	5 each	RT
Dehydration	50% Ethanol	5	RT
Dehydration	70% Ethanol	5	RT
Dehydration	2x100% Ethanol	5 each	RT
Air dry	Create hydrophobic barrier (Biozol Diagnostica, #VEC-H4000)		RT
Digestion	Protease IV	15	RT
Wash	2xPBS	5 each	RT
Probe hybridization	Ms-Adra1a-C1, Ms-Gfap-C2, Ms-Sox9-C3 (50:1:1 dilution)	120	40°C
Wash	2xPBS	5 each	RT
Amplification 1	Amp-1	30	40°C
Wash	2xPBS	2 each	RT
Amplification 2	Amp-2	15	40°C
Wash	2xPBS	2 each	RT
Amplification 3	Amp-3	30	40°C
Wash	2xPBS	2 each	RT
Amplification 4	Amp Alt-4C	45	40°C
Wash	2xPBS	2 each	RT
Mounting	Prolong Gold Antifade with Dapi (Life Technologies, #P36931)		Stored at 4°C

5.6.1 Imaging of multiplex fluorescent RNAscope

Fluorescent images from multiplex fluorescent RNAscope stainings were obtained using a confocal microscope (Zeiss LSM900). Atto 550 was excited at 548 nm, emission was detected using emission wavelength between 535-632 nm. Atto 647 was excited at 650 nm, emission was detected using emission wavelength between 650-673 nm. Atto 488 was excited at 488 nm, emission was detected using emission wavelength between 410-545 nm. Dapi and Methoxy-XO4 were excited at 353, emission was detected using emission wavelength between 535-632 nm. To enable a quantification of Adra1a and Adra1d expression in the cortex and the hippocampus, ten z-stacks of 4 µm with a z-slice interval of 0.19 µm were imaged per region. Z-stacks were further processed by calculating the maximum intensity projections. The pinhole was set to an airy unit of one. Images were acquired with a x,y-resolution of 0.156 µm/pixel (higher magnified images, see Figure 2-10/11A,B). Overview images (see Figure 2-9) were obtained using a slide scanning microscope (Axio Scan.Z1, Zeiss). Atto 550 was excited at 553 nm, emission was detected using an emission filter 586 – 601 nm. Dapi and Methoxy-XO4 were excited at 353 nm, emission was detected using an emission filter 412-438. Images were acquired with a x,y-resolution of 0.650 µm/pixel (Localization of Adra1a and Adra1d, see Figure 2-9).

5.6.2 Semi-quantitative analysis of multiplex fluorescent RNAscope

To determine the number of cells positive for the different probes a customized pipeline was generated using CellProfiler. Therefore, maximum intensity projections were loaded with separated channels into the program. First, Dapi images with nuclei as the first primary object were identified with a diameter range of 30-120 pixel units and a defined threshold, followed by an object expansion with 40 pixels to consider the cell cytosol. Second, within these identified expanded objects, the small dotted staining for each probe was identified in a diameter range of 3-10 pixel units separately for each probe. Subsequently, all identified dots of the different probes were related to the expanded nuclei. The final output included the number of dots for each cell and for each analysed probe. Next, a positive cell was defined to contain >15 dots/cell of each used probe. The specific classifications for the quantified cell populations are defined in Table 5-17.

Table 5-17 Cell classifications from identified probe expression from RNAscope.

Classification	Probe
Nonreactive astrocytes	Sox9+, Gfap-, Adra1a/d+or-
Reactive astrocytes	Sox9+, Gfap+, Adra1a/d+or-

5.7 RNA sequencing and data analysis

Library preparation and RNA-sequencing has been performed at the DZNE in Bonn (Research Group Schultze). The data analysis was mainly performed as a collaboration project with Stefanie Warnat-Herresthal.

5.7.1 RNA-sequencing library preparation and RNA-sequencing

mRNA was converted into libraries of double stranded cDNA molecules as a template for high throughput sequencing using TruSeq RNA Sample Prep Kit V2 (Illumina, # RS-122-2001) protocol according to manufacturer's instruction. In brief, mRNA was purified using poly-T oligo-attached magnetic beads. Fragmentation was carried out using divalent cations under elevated temperature in Illumina proprietary fragmentation buffer. First strand cDNA synthesis was performed using random oligonucleotides and Super Script II (Thermo Fisher Scientific, # 18064022) followed by second strand synthesis using DNA Polymerase I and RNaseH. Remaining overhangs were converted into blunt ends via exonuclease/polymerase activities and enzymes were removed. Subsequently, 3'ends were adenylated, and Illumina indexed PE adapter oligonucleotides were ligated to prepare for hybridization to Illumina flowcells. DNA fragments with ligated adapter molecules were selectively enriched using Illumina PCR primer PE1.0 and PE2.0 in a 15 cycle PCR reaction. SPRI beads (Beckman Coulter, # B23319) were used for purification and size selection of cDNA fragments preferentially 200–300 bp long. The size-distribution of cDNA libraries was measured using the Agilent high sensitivity D1000 assay on a 4200 TapeStation instrument (Agilent Technologies). cDNA libraries were quantified using the KAPA Library Quantification Kit (Roche, # 07960140001). After cluster generation on a cBot, a 75 bp single-end run was performed on a HiSeq1500 using the TruSeq SBS v3 chemistry (Illumina, #FC-401-3001).

5.7.2 Data processing

Transcript abundances were quantified using kallisto (v 0.44.0) (Bray et al. 2016). The index for quantification was built from the murine transcriptome M16 as published by GENCODE (ftp://ftp.ebi.ac.uk/pub/databases/gencode/Gencode_mouse/release_M16/gencode.vM16.primary_assembly.annotation.gtf.gz). Samples with less than 2 million pseudoaligned reads were excluded from further analysis. The raw read counts were imported into R and analyzed using the R package DESeq2 (Love et al. 2014) . Genes were filtered for a minimum expression of 10 counts over all samples. For analysis, two datasets were generated and normalized separately. The first dataset consisted of all 39 samples (18 Ribotag and 27 non-Ribotag) and 29189 genes, the second one of 18 Ribotag samples and 22895 genes.

5.7.3 Statistics and descriptive bioinformatics

Differentially expressed genes (DEGs) between all groups were determined using the package DESeq2, which uses negative binomial generalized linear models to test for differential expression. All genes with a p-value < 0.05 were considered differentially expressed. Multiple testing correction was done using independent hypothesis weighting as implemented in the R package DESeq2. Data visualization was facilitated by performing Principle Component Analysis (PCA) on all genes and hierarchical clustering of union of DEGs for the data set including all samples and DEGs with only the RiboTag samples with default settings in R. Gene set enrichment analysis (GSEA) DE genes for RiboTag data was performed with clusterProfiler (Yu et al. 2012) with a background set of all present genes or a known list of genes representing the surfaceome (https://www.proteinatlas.org/about/licence). The 1,665 DEGs for the RiboTag data were filtered by a list of known murine surface proteins and downstream effector proteins. These data were analysed using R. The $p < 0.05$ was accepted as statistically significant.

5.8 Immunohistochemistry (IHC)

Mice were transcranial perfused using ice-cold sterile 10 ml 0.9% NaCl followed by ice-cold 20 ml 4% paraformaldehyde (PFA) for tissue fixation. Fixed brains were removed and post-fixed in 4% PFA over-night at 4°C. For cryoprotection, brains were transferred on the next day first to 15% and second to 25% Sucrose (Sigma, #S5016) diluted in PBS with 0.01% (v/v) sodium azide (NaN_3, Roth) at 4°C. Next, brains were embedded in OCT embedding medium (Fisher Scientific, #12678646) and sliced into 20 µm thin sagittal sections at -20°C using a cryostat (Cryostar NX70, Thermo Fisher Scientific). Section were collected and stored in PBS with 0.01% (v/v) NaN_3 at 4°C. Immunohistochemical (IHC) staining was conducted in a free-floating procedure. First, sections were blocked and permeabilized by 1 h incubation at RT with blocking solution (10% NGS, 0.3% Triton-X 100(Roth, #3051.3) in PBS) with subsequent over-night incubation at 4°C with the primary antibodies diluted in appropriate buffer (5% NGS, 0.05% Triton-X 100 in PBS) On the next day, sections were washed three time for 5 min with PBS+5% normal goat serum (NGS) and then incubated for 3 h with the secondary antibodies diluted in PBS at RT. After incubation with the secondary antibodies, sections were washed three times with PBS and in the case of APP/PS1 mouse brains, additional staining with Methoxy-XO4 (1:5000 in PBS, Bio Techne , #4920/10) for 30 min at RT was performed to visualize Aβ plaques. Finally, sections were mounted on glass slides (Superfrost plus, Thermo Fisher Scientific, #10149870) either with Fluoromount-G without Dapi (Biozol Diagnostica Vertrieb , #SBA-0100-01) for Methoxy-XO4 stained sections or with Fluoromount-G with Dapi (Biozol Diagnostica Vertrieb, #SBA-0100-20). Used antibodies, dilutions and information are listed in Table 5-18.

Table 5-18 Antibodies used in immunohistochemistry.

Antibody	Dilution	Company	Order-No.
Rabbit anti-Sox9	1:2000	Sigma-Aldrich	AB5535
Rat anit-HA	1:200	Roche	11867423001
Chicken anti-GFP	1:500	Abcam	ab13970
Goat-anti-chicken Alexa fluor488	1:1000	Invitrogen	A-11039
Goat-anti-rat Alexa fluor488	1:1000	Invitrogen	A-11006
Goat-anti-rabbit Alexa fluor647	1:1000	Invitrogen	A-21244

5.8.1 Imaging of IHC staining

Fluorescent images from multiplex fluorescent RNAscope staining were obtained using a confocal microscope (Zeiss LSM700). Alexa Fluor647 was excited at 639 nm, emission was detected using a longpass filter (640 nm; Zeiss). Alexa Fluor488 was excited at 488 nm, emission was detected using a bandpass filter (490–555 nm; Zeiss). Dapi and Methoxy-XO4 were excited at 405, emission was detected using a shortpass filter (490 nm; Zeiss). The pinhole was set to an airy unit of one. Images with a x,y-resolution of 1.250 µm/pixel (RiboTag specificity, see Figure 2-1) and 0.625 µm/pixel (transduction efficiency, see Figure 2-22).

5.8.2 Quantification of the virus transduction efficiency

To determine the number of cells GCaMP6f expressing astrocytes, a customized pipeline was generated using CellProfiler. Therefore, images were loaded with separated channels into the program. First, Sox9 stainings representing astrocytic nuclei as the first primary object were identified with a diameter range of 4-10 pixel units and a defined threshold, followed by an object expansion with 4 pixels to consider the cell cytosol. Second, within these identified expanded objects, the intensity of the GCaMP6f staining surrounding the nuclei for cytosolic fluorescent signal was identified. Finally, all Sox9 and GCaMP6f positive cells were determined and the ratio between all Sox9 positive cells to double positive cells was calculated and demonstrated in percentage.

5.9 Statistics

Statistical significance was analysed with R. Analysed data was not following the normal distribution (Gaussian distribution) and was thereby tested by non-parametric tests. Statistical comparison of two groups was performed using Kruskal-Wallis test. Statistical significance for multiple comparisons was performed by Kruskal-Wallis test followed by pairwise Wilcoxon test or Dunn's multi comparison test with original False Discovery Rate p.adjustment method. *N* was defined as the number of field of views, time points, or mice throughout on a case-by-case basis depending on the particular experiment. Detailed statistical specifications were mentioned in the corresponding figures. P-value < 0.05 was defined as statistically significant.

6 Appendix

6.1 List of Figures

6.2 List of Tables

6.3 Abbreviations

2PLSM	Two photon laser scanning microscopy
AAV	adeno associated virus
ACh	acetylcholine
AD	Alzheimer's disease
ADP	adenosine diphosphate
AICD	intracellular APP domain
APOE	Apolipoprotein E
APP	amyloid precursor protein
APs	action potentials
AR	adrenergic receptors
ATP	adenosine triphosphate
Aβ	amyloid beta
BBB	blood brain barrier
Bp	base pairs
Bp	base pairs
C3ar1	C3a receptor 1
Ca^{2+}	Calcium
Cacna	voltage-gated calcium channel
CaSCaDe	Ca^{2+} Signal Classification and Decoding
Cers1	Ceramide synthase 1
CNS	central nervous system
CTF	C-terminal fragment
Cx43	Connexin 43, gap-junction alpha-1 protein (Gja1)
dE9	deleted exon9
DEGs	differentially expressed genes
EHSB	extra high salt polysome buffer
Entpd2	ectonucleoside triphosphate diphosphohydrolase 2
EphA4	erythropoietin producing hepatocellular A4
ER	Endoplasmic Reticulum
ER(T)	estrogen receptor (tamoxifen)
FACS	fluorescence activated cell sorting
FACS	fluorescence activated cell sorting
FAD	familial Alzheimer's disease
FC	fold change
FDHM	full duration at half maxium

FDR	false discovery rate
FLIM	fluorescent life-time imaging microscopy
FOV	Field of view
GABA	gamma-aminobutyric acid
GECI	genetically encoded calcium indicator
GFAP	Glial fibrillary acidic protein
GO	Gene ontology
GPCR	G-protein couple receptor
GSEA	gene set enrichment analysis
GT	Gliotransmitter
HA	Haemagglutinin
HSB	high salt polysome buffer
Hu	Human
IP3	inositol-1,4,5-trisphosphate
IP_3R	inositol-1,4,5-trisphosphate receptor
KEGG	Kyoto Encyclopedia of Genes and Genomes
LANUV	State Agency for Nature Environment and Consumer Protection
LC	locus coeruleus
LPS	lipopolysaccharide
LTD	long-term depression
LTP	long-term potentiation
mAChRs	metabotropic choline muscarinic receptors
MCAO	middle cerebral artery occlusion
MGI	Mouse Genome Informatics
Mo	Mouse
mRNA	messenger RNA
MW	Molecular weight
NA	noradrenalin
NCX2	Sodium/Calcium Exchanger 2
NE	norepinephrine
NFT	Neurofibrillary tangles
NMDAR	N-methyl-D-aspartate receptor
NT	Neurotransmitter
P2y1	P2 purinoceptor subtype Y1
PCA	principle component analysis
PFA	paraformaldehyde

PGDB	Protein G Dynabeads
PLC	Phospholipase C
Prp	prion protein
PS1	Presenilin 1
PS2	Presenilin 2
PSB	Polysome buffer
Psmb10	proteasome 20S subunit beta 10
qPCR	quantitative polymerase chain reaction
qPCR	quantitative polymerase chain reaction
RH	relative humidity
RNA	Ribonucleic acid
RNAseq	RNA sequencing
ROI	region of interest
ROS	reactive oxygen species
Rpl22	ribosomal protein L22
Rpm	rounds per minute
s.c.	subcutaneously
S1P	Sphingosin-1-phosphate
scqPCR	single cell qPCR
Slc8a2	Solute Carrier Family 8 Member A2
SNA	string network analysis
SNARE	soluble N-ethylmaleimide-sensitive fusion protein attachment protein receptor
SPF	specific pathogen-free conditions
Sphk1	Sphingosine kinase 1
Swe	Swedish
Tg	transgenic
Tm	melting temperature
Tm	temperature
Trem2	triggering receptor expressed on myeloid cells 2
TRP	transient receptor potential
Tyr	Tyrosinase
WT	wild type

6.4 Contributions

Theresa Schulte and Jan Peter conducted the genotyping for transgenic mice. Hana Matuskova provided help to optimize the RNAscope experiments and took the overview images of the brain slices. Walker S. Jackson provided the $Cx43^{Cre\text{-}ER(T)}$; RiboTag mice. Kristian Händler conducted the RNA sequencing and Stefanie Warnat-Herresthal performed the main data analysis (AG Schultze). Falko Fuhrmann helped with the awake imaging setup with the linear treadmill and the position read-out. Gilles Bonvento from Institut d'Imagerie Biomédicale (France) produced and provided the AAV.PHPeB-sGFAP-cyto-GCaMP6f in the first place. Christoph Möhl (Imaging and Data Analysis Facility) produced and optimized the used Ca^{2+} peak detection tools. Figures were partly created by using the online software BioRender.

7 References

Agarwal, Amit; Wu, Pei-Hsun; Hughes, Ethan G.; Fukaya, Masahiro; Tischfield, Max A.; Langseth, Abraham J. et al. (2017): Transient Opening of the Mitochondrial Permeability Transition Pore Induces Microdomain Calcium Transients in Astrocyte Processes. In: *Neuron* 93 (3), 587-605.e7. DOI: 10.1016/j.neuron.2016.12.034.

Agulhon, Cendra; Petravicz, Jeremy; McMullen, Allison B.; Sweger, Elizabeth J.; Minton, Suzanne K.; Taves, Sarah R. et al. (2008): What is the role of astrocyte calcium in neurophysiology? In: *Neuron* 59 (6), S. 932–946. DOI: 10.1016/j.neuron.2008.09.004.

Allen, Nicola J.; Eroglu, Cagla (2017): Cell Biology of Astrocyte-Synapse Interactions. In: *Neuron* 96 (3), S. 697–708. DOI: 10.1016/j.neuron.2017.09.056.

Alzheimer, A. (1911): über eigenartige Krankheitsfälle des späteren Alters. In: *Z. f. d. g. Neur. u. Psych.* 4 (1), S. 356–385. DOI: 10.1007/BF02866241.

Araque, Alfonso; Carmignoto, Giorgio; Haydon, Philip G.; Oliet, Stéphane H. R.; Robitaille, Richard; Volterra, Andrea (2014): Gliotransmitters travel in time and space. In: *Neuron* 81 (4), S. 728–739. DOI: 10.1016/j.neuron.2014.02.007.

Ashe, K. H. (2001): Learning and memory in transgenic mice modeling Alzheimer's disease. In: *Learning & memory (Cold Spring Harbor, N.Y.)* 8 (6), S. 301–308. DOI: 10.1101/lm.43701.

Aston-Jones, Gary; Cohen, Jonathan D. (2005): An integrative theory of locus coeruleus-norepinephrine function: adaptive gain and optimal performance. In: *Annual review of neuroscience* 28, S. 403–450. DOI: 10.1146/annurev.neuro.28.061604.135709.

Ballatore, Carlo; Lee, Virginia M-Y; Trojanowski, John Q. (2007): Tau-mediated neurodegeneration in Alzheimer's disease and related disorders. In: *Nature reviews. Neuroscience* 8 (9), S. 663–672. DOI: 10.1038/nrn2194.

Barres, Ben A. (2008): The mystery and magic of glia: a perspective on their roles in health and disease. In: *Neuron* 60 (3), S. 430–440. DOI: 10.1016/j.neuron.2008.10.013.

Bazargani, Narges; Attwell, David (2017): Amines, Astrocytes, and Arousal. In: *Neuron* 94 (2), S. 228–231. DOI: 10.1016/j.neuron.2017.03.035.

Bekar, Lane K.; He, Wei; Nedergaard, Maiken (2008): Locus coeruleus alpha-adrenergic-mediated activation of cortical astrocytes in vivo. In: *Cerebral cortex (New York, N.Y. : 1991)* 18 (12), S. 2789–2795. DOI: 10.1093/cercor/bhn040.

Belluscio, Leonardo (2005): Two-photon imaging in live rodents. In: *Current protocols in neuroscience* Chapter 2, Unit 2.9. DOI: 10.1002/0471142301.ns0209s32.

Ben Haim, Lucile; Ceyzériat, Kelly; Carrillo-de Sauvage, Maria Angeles; Aubry, Fabien; Auregan, Gwennaëlle; Guillermier, Martine et al. (2015): The JAK/STAT3 pathway is a common inducer of astrocyte reactivity in Alzheimer's and Huntington's diseases. In: *J. Neurosci.* 35 (6), S. 2817–2829. DOI: 10.1523/JNEUROSCI.3516-14.2015.

Bernardinelli, Yann; Randall, Jerome; Janett, Elia; Nikonenko, Irina; König, Stéphane; Jones, Emma Victoria et al. (2014): Activity-dependent structural plasticity of perisynaptic astrocytic domains promotes excitatory synapse stability. In: *Current biology : CB* 24 (15), S. 1679–1688. DOI: 10.1016/j.cub.2014.06.025.

Bindocci, Erika; Savtchouk, Iaroslav; Liaudet, Nicolas; Becker, Denise; Carriero, Giovanni; Volterra, Andrea (2017): Three-dimensional Ca2+ imaging advances understanding of astrocyte biology. In: *Science (New York, N.Y.)* 356 (6339). DOI: 10.1126/science.aai8185.

Bird, Thomas D. (2005): Genetic factors in Alzheimer's disease. In: *N Engl J Med* 352 (9), S. 862–864. DOI: 10.1056/NEJMp058027.

Boisvert, Matthew M.; Erikson, Galina A.; Shokhirev, Maxim N.; Allen, Nicola J. (2018): The Aging Astrocyte Transcriptome from Multiple Regions of the Mouse Brain. In: *Cell reports* 22 (1), S. 269–285. DOI: 10.1016/j.celrep.2017.12.039.

Boulay, Anne-Cécile; Saubaméa, Bruno; Adam, Nicolas; Chasseigneaux, Stéphanie; Mazaré, Noémie; Gilbert, Alice et al. (2017): Translation in astrocyte distal processes sets molecular heterogeneity at the gliovascular interface. In: *Cell discovery* 3, S. 17005. DOI: 10.1038/celldisc.2017.5.

Braak, H.; Braak, E. (1991): Neuropathological stageing of Alzheimer-related changes. In: *Acta neuropathologica* 82 (4), S. 239–259. DOI: 10.1007/bf00308809.

Bray, Nicolas L.; Pimentel, Harold; Melsted, Páll; Pachter, Lior (2016): Near-optimal probabilistic RNA-seq quantification. In: *Nat Biotechnol* 34 (5), S. 525–527. DOI: 10.1038/nbt.3519.

Brazhe, Alexey R.; Verisokin, Andrey Y.; Verveyko, Darya V.; Postnov, Dmitry E. (2018): Sodium-Calcium Exchanger Can Account for Regenerative Ca2+ Entry in Thin Astrocyte Processes. In: *Frontiers in cellular neuroscience* 12, S. 250. DOI: 10.3389/fncel.2018.00250.

Bronzuoli, Maria Rosanna; Facchinetti, Roberta; Valenza, Marta; Cassano, Tommaso; Steardo, Luca; Scuderi, Caterina (2019): Astrocyte Function Is Affected by Aging and Not Alzheimer's Disease: A Preliminary Investigation in Hippocampi of 3xTg-AD Mice. In: *Frontiers in pharmacology* 10, S. 644. DOI: 10.3389/fphar.2019.00644.

Burda, Joshua E.; Sofroniew, Michael V. (2014): Reactive Gliosis and the Multicellular Response to CNS Damage and Disease. In: *Neuron* 81 (2), S. 229–248. DOI: 10.1016/j.neuron.2013.12.034.

Bushong, Eric A.; Martone, Maryann E.; Jones, Ying Z.; Ellisman, Mark H. (2002): Protoplasmic Astrocytes in CA1 Stratum Radiatum Occupy Separate Anatomical Domains. In: *J. Neurosci.* 22 (1), S. 183–192. DOI: 10.1523/JNEUROSCI.22-01-00183.2002.

Calhoun, M. E.; Burgermeister, P.; Phinney, A. L.; Stalder, M.; Tolnay, M.; Wiederhold, K. H. et al. (1999): Neuronal overexpression of mutant amyloid precursor protein results in prominent deposition of cerebrovascular amyloid. In: *Proceedings of the National Academy of Sciences of the United States of America* 96 (24), S. 14088–14093. DOI: 10.1073/pnas.96.24.14088.

Calhoun, M. E.; Wiederhold, K. H.; Abramowski, D.; Phinney, A. L.; Probst, A.; Sturchler-Pierrat, C. et al. (1998): Neuron loss in APP transgenic mice. In: *Nature* 395 (6704), S. 755–756. DOI: 10.1038/27351.

Campos, Carlos; Rocha, Nuno Barbosa; Vieira, Renata Teles; Rocha, Susana A.; Telles-Correia, Diogo; Paes, Flávia et al. (2016): Treatment of Cognitive Deficits in Alzheimer's disease: A psychopharmacological review. In: *Psychiatria Danubina* 28 (1), S. 2–12.

Cao, Jiqing; Hou, Jianwei; Ping, Jing; Cai, Dongming (2018): Advances in developing novel therapeutic strategies for Alzheimer's disease. In: *Mol Neurodegeneration* 13 (1), S. 64. DOI: 10.1186/s13024-018-0299-8.

Castiglioni, A. J.; Legare, M. E.; Busbee, D. L.; Tiffany-Castiglioni, E. (1991): Morphological changes in astrocytes of aging mice fed normal or caloric restricted diets. In: *AGE* 14 (4), S. 102–106. DOI: 10.1007/BF02435015.

Ceyzériat, Kelly; Ben Haim, Lucile; Denizot, Audrey; Pommier, Dylan; Matos, Marco; Guillemaud, Océane et al. (2018): Modulation of astrocyte reactivity improves functional deficits in mouse

models of Alzheimer's disease. In: *Acta neuropathologica communications* 6 (1), S. 104. DOI: 10.1186/s40478-018-0606-1.

Chai, Hua; Diaz-Castro, Blanca; Shigetomi, Eiji; Monte, Emma; Octeau, J. Christopher; Yu, Xinzhu et al. (2017): Neural Circuit-Specialized Astrocytes: Transcriptomic, Proteomic, Morphological, and Functional Evidence. In: *Neuron* 95 (3), 531-549.e9. DOI: 10.1016/j.neuron.2017.06.029.

Chan, Ken Y.; Jang, Min J.; Yoo, Bryan B.; Greenbaum, Alon; Ravi, Namita; Wu, Wei-Li et al. (2017): Engineered AAVs for efficient noninvasive gene delivery to the central and peripheral nervous systems. In: *Nature neuroscience* 20 (8), S. 1172–1179. DOI: 10.1038/nn.4593.

Chen, Naiyan; Sugihara, Hiroki; Sharma, Jitendra; Perea, Gertrudis; Petravicz, Jeremy; Le, Chuong; Sur, Mriganka (2012): Nucleus basalis-enabled stimulus-specific plasticity in the visual cortex is mediated by astrocytes. In: *Proceedings of the National Academy of Sciences of the United States of America* 109 (41), E2832-41. DOI: 10.1073/pnas.1206557109.

Chen, Tsai-Wen; Wardill, Trevor J.; Sun, Yi; Pulver, Stefan R.; Renninger, Sabine L.; Baohan, Amy et al. (2013): Ultrasensitive fluorescent proteins for imaging neuronal activity. In: *Nature* 499 (7458), S. 295–300. DOI: 10.1038/nature12354.

Clarke, Laura E.; Liddelow, Shane A.; Chakraborty, Chandrani; Münch, Alexandra E.; Heiman, Myriam; Barres, Ben A. (2018): Normal aging induces A1-like astrocyte reactivity. In: *Proceedings of the National Academy of Sciences of the United States of America* 115 (8), E1896-E1905. DOI: 10.1073/pnas.1800165115.

Cline, Erika N.; Bicca, Maíra Assunção; Viola, Kirsten L.; Klein, William L. (2018): The Amyloid-β Oligomer Hypothesis: Beginning of the Third Decade. In: *Journal of Alzheimer's Disease* 64 (s1), S567-S610. DOI: 10.3233/JAD-179941.

Cummings, Jeffrey; Lee, Garam; Ritter, Aaron; Sabbagh, Marwan; Zhong, Kate (2019): Alzheimer's disease drug development pipeline: 2019. In: *Alzheimer's & dementia (New York, N. Y.)* 5, S. 272–293. DOI: 10.1016/j.trci.2019.05.008.

Delekate, Andrea; Füchtemeier, Martina; Schumacher, Toni; Ulbrich, Cordula; Foddis, Marco; Petzold, Gabor C. (2014): Metabotropic P2Y1 receptor signalling mediates astrocytic hyperactivity in vivo in an Alzheimer's disease mouse model. In: *Nature communications* 5, S. 5422. DOI: 10.1038/ncomms6422.

Di Castro, Maria Amalia; Chuquet, Julien; Liaudet, Nicolas; Bhaukaurally, Khaleel; Santello, Mirko; Bouvier, David et al. (2011): Local Ca2+ detection and modulation of synaptic release by astrocytes. In: *Nature neuroscience* 14 (10), S. 1276–1284. DOI: 10.1038/nn.2929.

Diaz-Castro, Blanca; Gangwani, Mohitkumar R.; Yu, Xinzhu; Coppola, Giovanni; Khakh, Baljit S. (2019): Astrocyte molecular signatures in Huntington's disease. In: *Science translational medicine* 11 (514). DOI: 10.1126/scitranslmed.aaw8546.

Ding, Fengfei; O'Donnell, John; Thrane, Alexander S.; Zeppenfeld, Douglas; Kang, Hongyi; Xie, Lulu et al. (2013): α1-Adrenergic receptors mediate coordinated Ca2+ signaling of cortical astrocytes in awake, behaving mice. In: *Cell calcium* 54 (6), S. 387–394. DOI: 10.1016/j.ceca.2013.09.001.

Djogo, Nevena; Jakovcevski, Igor; Müller, Christian; Lee, Hyun Joon; Xu, Jin-Chong; Jakovcevski, Mira et al. (2013): Adhesion molecule L1 binds to amyloid beta and reduces Alzheimer's disease pathology in mice. In: *Neurobiology of disease* 56, S. 104–115. DOI: 10.1016/j.nbd.2013.04.014.

Dong, Jun-hong; Chen, Xin; Cui, Min; Yu, Xiao; Pang, Qi; Sun, Jin-peng (2012): β2-adrenergic receptor and astrocyte glucose metabolism. In: *J Mol Neurosci* 48 (2), S. 456–463. DOI: 10.1007/s12031-012-9742-4.

Dovey, H. F.; John, V.; Anderson, J. P.; Chen, L. Z.; Saint Andrieu, P. de; Fang, L. Y. et al. (2001): Functional gamma-secretase inhibitors reduce beta-amyloid peptide levels in brain. In: *Journal of neurochemistry* 76 (1), S. 173–181. DOI: 10.1046/j.1471-4159.2001.00012.x.

Drewes, Gerard; Ebneth, Andreas; Mandelkow, Eva-Maria (1998): MAPs, MARKs and microtubule dynamics. In: *Trends in Biochemical Sciences* 23 (8), S. 307–311. DOI: 10.1016/S0968-0004(98)01245-6.

Dunn, Kathryn M.; Hill-Eubanks, David C.; Liedtke, Wolfgang B.; Nelson, Mark T. (2013): TRPV4 channels stimulate Ca2+-induced Ca2+ release in astrocytic endfeet and amplify neurovascular coupling responses. In: *Proceedings of the National Academy of Sciences of the United States of America* 110 (15), S. 6157–6162. DOI: 10.1073/pnas.1216514110.

Edwards Iii, George A.; Gamez, Nazaret; Escobedo, Gabriel; Calderon, Olivia; Moreno-Gonzalez, Ines (2019): Modifiable Risk Factors for Alzheimer's Disease. In: *Frontiers in aging neuroscience* 11, S. 146. DOI: 10.3389/fnagi.2019.00146.

Eggermann, Emmanuel; Kremer, Yves; Crochet, Sylvain; Petersen, Carl C. H. (2014): Cholinergic signals in mouse barrel cortex during active whisker sensing. In: *Cell reports* 9 (5), S. 1654–1660. DOI: 10.1016/j.celrep.2014.11.005.

Elhusseiny, A.; Cohen, Z.; Olivier, A.; Stanimirović, D. B.; Hamel, E. (1999): Functional acetylcholine muscarinic receptor subtypes in human brain microcirculation: identification and cellular localization. In: *Journal of cerebral blood flow and metabolism : official journal of the International Society of Cerebral Blood Flow and Metabolism* 19 (7), S. 794–802. DOI: 10.1097/00004647-199907000-00010.

Escartin, Carole; Guillemaud, Océane; Carrillo-de Sauvage, Maria-Angeles (2019): Questions and (some) answers on reactive astrocytes. In: *Glia* 67 (12), S. 2221–2247. DOI: 10.1002/glia.23687.

Feng, Jiesi; Zhang, Changmei; Lischinsky, Julieta E.; Jing, Miao; Zhou, Jingheng; Wang, Huan et al. (2019): A Genetically Encoded Fluorescent Sensor for Rapid and Specific In Vivo Detection of Norepinephrine. In: *Neuron* 102 (4), 745-761.e8. DOI: 10.1016/j.neuron.2019.02.037.

Ferreira, Sergio T.; Vieira, Marcelo N. N.; Felice, Fernanda G. de (2007): Soluble protein oligomers as emerging toxins in Alzheimer's and other amyloid diseases. In: *IUBMB life* 59 (4-5), S. 332–345. DOI: 10.1080/15216540701283882.

Fischer, Iris; Alliod, Chantal; Martinier, Nicolas; Newcombe, Jia; Brana, Corinne; Pouly, Sandrine (2011): Sphingosine kinase 1 and sphingosine 1-phosphate receptor 3 are functionally upregulated on astrocytes under pro-inflammatory conditions. In: *PloS one* 6 (8), e23905. DOI: 10.1371/journal.pone.0023905.

Foskett, J. Kevin; White, Carl; Cheung, King-Ho; Mak, Don-On Daniel (2007): Inositol trisphosphate receptor Ca2+ release channels. In: *Physiological reviews* 87 (2), S. 593–658. DOI: 10.1152/physrev.00035.2006.

Frugier, Tony; Conquest, Alison; McLean, Catriona; Currie, Peter; Moses, David; Goldshmit, Yona (2012): Expression and activation of EphA4 in the human brain after traumatic injury. In: *Journal of neuropathology and experimental neurology* 71 (3), S. 242–250. DOI: 10.1097/NEN.0b013e3182496149.

Fu, Amy K. Y.; Hung, Kwok-Wang; Huang, Huiqian; Gu, Shuo; Shen, Yang; Cheng, Elaine Y. L. et al. (2014a): Blockade of EphA4 signaling ameliorates hippocampal synaptic dysfunctions in mouse models of Alzheimer's disease. In: *Proceedings of the National Academy of Sciences of the United States of America* 111 (27), S. 9959–9964. DOI: 10.1073/pnas.1405803111.

Fu, Yu; Tucciarone, Jason M.; Espinosa, J. Sebastian; Sheng, Nengyin; Darcy, Daniel P.; Nicoll, Roger A. et al. (2014b): A cortical circuit for gain control by behavioral state. In: *Cell* 156 (6), S. 1139–1152. DOI: 10.1016/j.cell.2014.01.050.

Games, D.; Adams, D.; Alessandrini, R.; Barbour, R.; Berthelette, P.; Blackwell, C. et al. (1995): Alzheimer-type neuropathology in transgenic mice overexpressing V717F beta-amyloid precursor protein. In: *Nature* 373 (6514), S. 523–527. DOI: 10.1038/373523a0.

Gatz, Margaret; Reynolds, Chandra A.; Fratiglioni, Laura; Johansson, Boo; Mortimer, James A.; Berg, Stig et al. (2006): Role of genes and environments for explaining Alzheimer disease. In: *Arch Gen Psychiatry* 63 (2), S. 168–174. DOI: 10.1001/archpsyc.63.2.168.

Genoud, Christel; Quairiaux, Charles; Steiner, Pascal; Hirling, Harald; Welker, Egbert; Knott, Graham W. (2006): Plasticity of astrocytic coverage and glutamate transporter expression in adult mouse cortex. In: *PLoS biology* 4 (11), e343. DOI: 10.1371/journal.pbio.0040343.

Glawe, John D.; Patrick, D. Ross; Huang, Meng; Sharp, Christopher D.; Barlow, Shayne C.; Kevil, Christopher G. (2009): Genetic deficiency of Itgb2 or ItgaL prevents autoimmune diabetes through distinctly different mechanisms in NOD/LtJ mice. In: *Diabetes* 58 (6), S. 1292–1301. DOI: 10.2337/db08-0804.

Goate, A.; Chartier-Harlin, M. C.; Mullan, M.; Brown, J.; Crawford, F.; Fidani, L. et al. (1991): Segregation of a missense mutation in the amyloid precursor protein gene with familial Alzheimer's disease. In: *Nature* 349 (6311), S. 704–706. DOI: 10.1038/349704a0.

Goldey, Glenn J.; Roumis, Demetris K.; Glickfeld, Lindsey L.; Kerlin, Aaron M.; Reid, R. Clay; Bonin, Vincent et al. (2014): Removable cranial windows for long-term imaging in awake mice. In: *Nature protocols* 9 (11), S. 2515–2538. DOI: 10.1038/nprot.2014.165.

Goldshmit, Yona; Bourne, James (2010): Upregulation of EphA4 on astrocytes potentially mediates astrocytic gliosis after cortical lesion in the marmoset monkey. In: *Journal of neurotrauma* 27 (7), S. 1321–1332. DOI: 10.1089/neu.2010.1294.

Gómez-Gonzalo, Marta; Martin-Fernandez, Mario; Martínez-Murillo, Ricardo; Mederos, Sara; Hernández-Vivanco, Alicia; Jamison, Stephanie et al. (2017): Neuron-astrocyte signaling is preserved in the aging brain. In: *Glia* 65 (4), S. 569–580. DOI: 10.1002/glia.23112.

Götz, Jürgen; Schild, Andreas; Hoerndli, Fred; Pennanen, Luis (2004): Amyloid-induced neurofibrillary tangle formation in Alzheimer's disease: insight from transgenic mouse and tissue-culture models. In: *International journal of developmental neuroscience : the official journal of the International Society for Developmental Neuroscience* 22 (7), S. 453–465. DOI: 10.1016/j.ijdevneu.2004.07.013.

Gratuze, Maud; Leyns, Cheryl E. G.; Holtzman, David M. (2018): New insights into the role of TREM2 in Alzheimer's disease. In: *Mol Neurodegeneration* 13 (1), S. 66. DOI: 10.1186/s13024-018-0298-9.

Grossman, Murray (1992): Book Review Dementia: A clinical approach Second edition. By Jeffrey L. Cummings and D. Frank Benson. 548 pp., illustrated. Boston, Butterworth-Heinemann, 1992. $95. ISBN 0–7506–9065–8. In: *N Engl J Med* 327 (1), S. 61. DOI: 10.1056/NEJM199207023270122.

Guerra-Gomes, Sónia; Sousa, Nuno; Pinto, Luísa; Oliveira, João F. (2017): Functional Roles of Astrocyte Calcium Elevations: From Synapses to Behavior. In: *Frontiers in cellular neuroscience* 11, S. 427. DOI: 10.3389/fncel.2017.00427.

Guerreiro, Rita; Wojtas, Aleksandra; Bras, Jose; Carrasquillo, Minerva; Rogaeva, Ekaterina; Majounie, Elisa et al. (2013): TREM2 variants in Alzheimer's disease. In: *The New England journal of medicine* 368 (2), S. 117–127. DOI: 10.1056/NEJMoa1211851.

Guizar-Sicairos, Manuel; Thurman, Samuel T.; Fienup, James R. (2008): Efficient subpixel image registration algorithms. In: *Opt. Lett., OL* 33 (2), S. 156–158. DOI: 10.1364/OL.33.000156.

Haass, Christian; Selkoe, Dennis J. (2007): Soluble protein oligomers in neurodegeneration: lessons from the Alzheimer's amyloid beta-peptide. In: *Nature reviews. Molecular cell biology* 8 (2), S. 101–112. DOI: 10.1038/nrm2101.

Habib, Naomi; McCabe, Cristin; Medina, Sedi; Varshavsky, Miriam; Kitsberg, Daniel; Dvir-Szternfeld, Raz et al. (2020): Disease-associated astrocytes in Alzheimer's disease and aging. In: *Nat Neurosci*, S. 1–6. DOI: 10.1038/s41593-020-0624-8.

Halassa, Michael M.; Fellin, Tommaso; Haydon, Philip G. (2007): The tripartite synapse: roles for gliotransmission in health and disease. In: *Trends in molecular medicine* 13 (2), S. 54–63. DOI: 10.1016/j.molmed.2006.12.005.

Halassa, Michael M.; Haydon, Philip G. (2010): Integrated brain circuits: astrocytic networks modulate neuronal activity and behavior. In: *Annual review of physiology* 72, S. 335–355. DOI: 10.1146/annurev-physiol-021909-135843.

Hall, Alicia M.; Roberson, Erik D. (2012): Mouse models of Alzheimer's disease. In: *Brain research bulletin* 88 (1), S. 3–12. DOI: 10.1016/j.brainresbull.2011.11.017.

Haustein, Martin D.; Kracun, Sebastian; Lu, Xiao-Hong; Shih, Tiffany; Jackson-Weaver, Olan; Tong, Xiaoping et al. (2014): Conditions and constraints for astrocyte calcium signaling in the hippocampal mossy fiber pathway. In: *Neuron* 82 (2), S. 413–429. DOI: 10.1016/j.neuron.2014.02.041.

Head, Elizabeth; Helman, Alex M.; Powell, David; Schmitt, Frederick A. (2018): Down syndrome, beta-amyloid and neuroimaging. In: *Free radical biology & medicine* 114, S. 102–109. DOI: 10.1016/j.freeradbiomed.2017.09.013.

Heller, Janosch P.; Rusakov, Dmitri A. (2015): Morphological plasticity of astroglia: Understanding synaptic microenvironment. In: *Glia* 63 (12), S. 2133–2151. DOI: 10.1002/glia.22821.

Hendrie, H. C. (1998): Epidemiology of dementia and Alzheimer's disease. In: *The American journal of geriatric psychiatry : official journal of the American Association for Geriatric Psychiatry* 6 (2 Suppl 1), S3-18. DOI: 10.1097/00019442-199821001-00002.

Henneberger, Christian; Rusakov, Dmitri A. (2010): Synaptic plasticity and Ca2+ signalling in astrocytes. In: *Neuron glia biology* 6 (3), S. 141–146. DOI: 10.1017/S1740925X10000153.

Herculano-Houzel, Suzana (2014): The glia/neuron ratio: how it varies uniformly across brain structures and species and what that means for brain physiology and evolution. In: *Glia* 62 (9), S. 1377–1391. DOI: 10.1002/glia.22683.

Hill, Julia M.; Stefani, Diego de; Jones, Aleck W. E.; Ruiz, Asier; Rizzuto, Rosario; Szabadkai, Gyorgy (2014): Measuring baseline Ca(2+) levels in subcellular compartments using genetically engineered fluorescent indicators. In: *Methods in enzymology* 543, S. 47–72. DOI: 10.1016/B978-0-12-801329-8.00003-9.

Hillen, Anne E. J.; Burbach, J. Peter H.; Hol, Elly M. (2018): Cell adhesion and matricellular support by astrocytes of the tripartite synapse. In: *Progress in neurobiology* 165-167, S. 66–86. DOI: 10.1016/j.pneurobio.2018.02.002.

Hsiao, K.; Chapman, P.; Nilsen, S.; Eckman, C.; Harigaya, Y.; Younkin, S. et al. (1996): Correlative memory deficits, Abeta elevation, and amyloid plaques in transgenic mice. In: *Science (New York, N.Y.)* 274 (5284), S. 99–102. DOI: 10.1126/science.274.5284.99.

Huang, Yadong (2011): Roles of apolipoprotein E4 (ApoE4) in the pathogenesis of Alzheimer's disease: lessons from ApoE mouse models. In: *Biochemical Society transactions* 39 (4), S. 924–932. DOI: 10.1042/BST0390924.

Irizarry, M. C.; McNamara, M.; Fedorchak, K.; Hsiao, K.; Hyman, B. T. (1997a): APPSw transgenic mice develop age-related A beta deposits and neuropil abnormalities, but no neuronal loss in CA1. In: *Journal of neuropathology and experimental neurology* 56 (9), S. 965–973. DOI: 10.1097/00005072-199709000-00002.

Irizarry, M. C.; Soriano, F.; McNamara, M.; Page, K. J.; Schenk, D.; Games, D.; Hyman, B. T. (1997b): Abeta deposition is associated with neuropil changes, but not with overt neuronal loss in the human amyloid precursor protein V717F (PDAPP) transgenic mouse. In: *The Journal of neuroscience : the official journal of the Society for Neuroscience* 17 (18), S. 7053–7059.

Iturria-Medina, Y.; Sotero, R. C.; Toussaint, P. J.; Mateos-Pérez, J. M.; Evans, A. C. (2016): Early role of vascular dysregulation on late-onset Alzheimer's disease based on multifactorial data-driven analysis. In: *Nat Commun* 7 (1), S. 11934. DOI: 10.1038/ncomms11934.

Jankowsky, J. L.; Slunt, H. H.; Ratovitski, T.; Jenkins, N. A.; Copeland, N. G.; Borchelt, D. R. (2001): Co-expression of multiple transgenes in mouse CNS: a comparison of strategies. In: *Biomolecular engineering* 17 (6), S. 157–165. DOI: 10.1016/s1389-0344(01)00067-3.

Jay, Taylor R.; Saucken, Victoria E. von; Muñoz, Braulio; Codocedo, Juan F.; Atwood, Brady K.; Lamb, Bruce T.; Landreth, Gary E. (2019): TREM2 is required for microglial instruction of astrocytic synaptic engulfment in neurodevelopment. In: *Glia* 67 (10), S. 1873–1892. DOI: 10.1002/glia.23664.

Jiang, Lin-Hua; Li, Xin; Syed Mortadza, Sharifah A.; Lovatt, Megan; Yang, Wei (2018): The TRPM2 channel nexus from oxidative damage to Alzheimer's pathologies: An emerging novel intervention target for age-related dementia. In: *Ageing research reviews* 47, S. 67–79. DOI: 10.1016/j.arr.2018.07.002.

Jyothi, H. J.; Vidyadhara, D. J.; Mahadevan, Anita; Philip, Mariamma; Parmar, Suresh Kumar; Manohari, S. Gowri et al. (2015): Aging causes morphological alterations in astrocytes and microglia in human substantia nigra pars compacta. In: *Neurobiology of aging* 36 (12), S. 3321–3333. DOI: 10.1016/j.neurobiolaging.2015.08.024.

Kanehisa, Minoru (2019): Toward understanding the origin and evolution of cellular organisms. In: *Protein science : a publication of the Protein Society* 28 (11), S. 1947–1951. DOI: 10.1002/pro.3715.

Kanemaru, Kazunori; Sekiya, Hiroshi; Xu, Ming; Satoh, Kaname; Kitajima, Nami; Yoshida, Keitaro et al. (2014): In vivo visualization of subtle, transient, and local activity of astrocytes using an ultrasensitive Ca(2+) indicator. In: *Cell reports* 8 (1), S. 311–318. DOI: 10.1016/j.celrep.2014.05.056.

Kang, Silvia S.; Baker, Kelsey E.; Wang, Xuewei; Kocher, Jeanne-Pierre; Fryer, John D. (2017): Translational profiling of microglia reveals artifacts of cell sorting.

Katzman, R. (1976): Editorial: The prevalence and malignancy of Alzheimer disease. A major killer. In: *Archives of neurology* 33 (4), S. 217–218. DOI: 10.1001/archneur.1976.00500040001001.

Kennedy, Matthew E.; Stamford, Andrew W.; Chen, Xia; Cox, Kathleen; Cumming, Jared N.; Dockendorf, Marissa F. et al. (2016): The BACE1 inhibitor verubecestat (MK-8931) reduces CNS β-amyloid in animal models and in Alzheimer's disease patients. In: *Science translational medicine* 8 (363), 363ra150. DOI: 10.1126/scitranslmed.aad9704.

Khakh, Baljit S.; Sofroniew, Michael V. (2015): Diversity of astrocyte functions and phenotypes in neural circuits. In: *Nature neuroscience* 18 (7), S. 942–952. DOI: 10.1038/nn.4043.

King, Anthony (2018): The search for better animal models of Alzheimer's disease. In: *Nature* 559 (7715), S13-S15. DOI: 10.1038/d41586-018-05722-9.

King, Claire M.; Bohmbach, Kirsten; Minge, Daniel; Delekate, Andrea; Zheng, Kaiyu; Reynolds, James et al. (2020): Local Resting Ca2+ Controls the Scale of Astroglial Ca2+ Signals. In: *Cell reports* 30 (10), 3466-3477.e4. DOI: 10.1016/j.celrep.2020.02.043.

King, Helen A.; Gerber, André P. (2016): Translatome profiling: methods for genome-scale analysis of mRNA translation. In: *Briefings in functional genomics* 15 (1), S. 22–31. DOI: 10.1093/bfgp/elu045.

Kjaerby, Celia; Rasmussen, Rune; Andersen, Mie; Nedergaard, Maiken (2017): Does Global Astrocytic Calcium Signaling Participate in Awake Brain State Transitions and Neuronal Circuit Function? In: *Neurochemical research* 42 (6), S. 1810–1822. DOI: 10.1007/s11064-017-2195-y.

Kretz, Markus; Euwens, Carsten; Hombach, Sonja; Eckardt, Dominik; Teubner, Barbara; Traub, Otto et al. (2003): Altered connexin expression and wound healing in the epidermis of connexin-deficient mice. In: *Journal of cell science* 116 (Pt 16), S. 3443–3452. DOI: 10.1242/jcs.00638.

Kuchibhotla, Kishore V.; Lattarulo, Carli R.; Hyman, Bradley T.; Bacskai, Brian J. (2009): Synchronous hyperactivity and intercellular calcium waves in astrocytes in Alzheimer mice. In: *Science (New York, N.Y.)* 323 (5918), S. 1211–1215. DOI: 10.1126/science.1169096.

Lanjakornsiripan, Darin; Pior, Baek-Jun; Kawaguchi, Daichi; Furutachi, Shohei; Tahara, Tomoaki; Katsuyama, Yu et al. (2018): Layer-specific morphological and molecular differences in neocortical astrocytes and their dependence on neuronal layers. In: *Nature communications* 9 (1), S. 1623. DOI: 10.1038/s41467-018-03940-3.

Lanz, Thomas A.; Wood, Kathleen M.; Richter, Karl E. G.; Nolan, Charles E.; Becker, Stacey L.; Pozdnyakov, Nikolay et al. (2010): Pharmacodynamics and pharmacokinetics of the gamma-secretase inhibitor PF-3084014. In: *The Journal of pharmacology and experimental therapeutics* 334 (1), S. 269–277. DOI: 10.1124/jpet.110.167379.

Lee, Youngjin; Messing, Albee; Su, Mu; Brenner, Michael (2008): GFAP promoter elements required for region-specific and astrocyte-specific expression. In: *Glia* 56 (5), S. 481–493. DOI: 10.1002/glia.20622.

Leshchyns'ka, Iryna; Sytnyk, Vladimir (2016): Synaptic Cell Adhesion Molecules in Alzheimer's Disease. In: *Neural plasticity* 2016, S. 6427537. DOI: 10.1155/2016/6427537.

Leuzy, Antoine; Chiotis, Konstantinos; Lemoine, Laetitia; Gillberg, Per-Göran; Almkvist, Ove; Rodriguez-Vieitez, Elena; Nordberg, Agneta (2019): Tau PET imaging in neurodegenerative tauopathies-still a challenge. In: *Molecular psychiatry* 24 (8), S. 1112–1134. DOI: 10.1038/s41380-018-0342-8.

Li, C. H.; Lee, C. K. (1993): Minimum cross entropy thresholding. In: *Pattern Recognition* 26 (4), S. 617–625. DOI: 10.1016/0031-3203(93)90115-D.

Lian, Hong; Litvinchuk, Alexandra; Chiang, Angie C-A; Aithmitti, Nadia; Jankowsky, Joanna L.; Zheng, Hui (2016): Astrocyte-Microglia Cross Talk through Complement Activation Modulates

Amyloid Pathology in Mouse Models of Alzheimer's Disease. In: *The Journal of neuroscience : the official journal of the Society for Neuroscience* 36 (2), S. 577–589. DOI: 10.1523/JNEUROSCI.2117-15.2016.

Liddelow, Shane A.; Guttenplan, Kevin A.; Clarke, Laura E.; Bennett, Frederick C.; Bohlen, Christopher J.; Schirmer, Lucas et al. (2017): Neurotoxic reactive astrocytes are induced by activated microglia. In: *Nature* 541 (7638), S. 481–487. DOI: 10.1038/nature21029.

Litvinchuk, Alexandra; Wan, Ying-Wooi; Swartzlander, Dan B.; Chen, Fading; Cole, Allysa; Propson, Nicholas E. et al. (2018): Complement C3aR Inactivation Attenuates Tau Pathology and Reverses an Immune Network Deregulated in Tauopathy Models and Alzheimer's Disease. In: *Neuron* 100 (6), 1337-1353.e5. DOI: 10.1016/j.neuron.2018.10.031.

Liu, Jinping; Chang, Lirong; Song, Yizhi; Li, Hui; Wu, Yan (2019): The Role of NMDA Receptors in Alzheimer's Disease. In: *Frontiers in neuroscience* 13, S. 43. DOI: 10.3389/fnins.2019.00043.

Livingston, Gill; Sommerlad, Andrew; Orgeta, Vasiliki; Costafreda, Sergi G.; Huntley, Jonathan; Ames, David et al. (2017): Dementia prevention, intervention, and care. In: *Lancet (London, England)* 390 (10113), S. 2673–2734. DOI: 10.1016/S0140-6736(17)31363-6.

Love, Michael I.; Huber, Wolfgang; Anders, Simon (2014): Moderated estimation of fold change and dispersion for RNA-seq data with DESeq2. In: *Genome biology* 15 (12), S. 550. DOI: 10.1186/s13059-014-0550-8.

Lucas, Bruce D.; Kanade, Takeo (1981): An iterative image registration technique with an application to stereo vision, zuletzt geprüft am 19.05.2020.

Luchena, Celia; Zuazo-Ibarra, Jone; Alberdi, Elena; Matute, Carlos; Capetillo-Zarate, Estibaliz (2018): Contribution of Neurons and Glial Cells to Complement-Mediated Synapse Removal during Development, Aging and in Alzheimer's Disease. In: *Mediators of Inflammation* 2018, S. 2530414. DOI: 10.1155/2018/2530414.

Lundgaard, I.; Osório, M. J.; Kress, B. T.; Sanggaard, S.; NEDERGAARD, M. (2014): White matter astrocytes in health and disease. In: *Neuroscience* 276, S. 161–173. DOI: 10.1016/j.neuroscience.2013.10.050.

Matias, Isadora; Morgado, Juliana; Gomes, Flávia Carvalho Alcantara (2019): Astrocyte Heterogeneity: Impact to Brain Aging and Disease. In: *Frontiers in aging neuroscience* 11, S. 59. DOI: 10.3389/fnagi.2019.00059.

May, Patrick C.; Willis, Brian A.; Lowe, Stephen L.; Dean, Robert A.; Monk, Scott A.; Cocke, Patrick J. et al. (2015): The potent BACE1 inhibitor LY2886721 elicits robust central Aβ pharmacodynamic responses in mice, dogs, and humans. In: *The Journal of neuroscience : the official journal of the Society for Neuroscience* 35 (3), S. 1199–1210. DOI: 10.1523/JNEUROSCI.4129-14.2015.

McGinley, Matthew J.; Vinck, Martin; Reimer, Jacob; Batista-Brito, Renata; Zagha, Edward; Cadwell, Cathryn R. et al. (2015): Waking State: Rapid Variations Modulate Neural and Behavioral Responses. In: *Neuron* 87 (6), S. 1143–1161. DOI: 10.1016/j.neuron.2015.09.012.

Mehta, Dev; Jackson, Robert; Paul, Gaurav; Shi, Jiong; Sabbagh, Marwan (2017): Why do trials for Alzheimer's disease drugs keep failing? A discontinued drug perspective for 2010-2015. In: *Expert opinion on investigational drugs* 26 (6), S. 735–739. DOI: 10.1080/13543784.2017.1323868.

Minelli, Andrea; Castaldo, Pasqualina; Gobbi, Pietro; Salucci, Sara; Magi, Simona; Amoroso, Salvatore (2007): Cellular and subcellular localization of Na+-Ca2+ exchanger protein isoforms,

NCX1, NCX2, and NCX3 in cerebral cortex and hippocampus of adult rat. In: *Cell calcium* 41 (3), S. 221–234. DOI: 10.1016/j.ceca.2006.06.004.

Montana, Vedrana; Malarkey, Erik B.; Verderio, Claudia; Matteoli, Michela; Parpura, Vladimir (2006): Vesicular transmitter release from astrocytes. In: *Glia* 54 (7), S. 700–715. DOI: 10.1002/glia.20367.

Murray, C. E.; King, A.; Troakes, C.; Hodges, A.; Lashley, T. (2019): APOE ε4 is also required in TREM2 R47H variant carriers for Alzheimer's disease to develop. In: *Neuropathology and applied neurobiology* 45 (2), S. 183–186. DOI: 10.1111/nan.12474.

Navarrete, Marta; Perea, Gertrudis; Fernandez de Sevilla, David; Gómez-Gonzalo, Marta; Núñez, Angel; Martín, Eduardo D.; Araque, Alfonso (2012): Astrocytes mediate in vivo cholinergic-induced synaptic plasticity. In: *PLoS biology* 10 (2), e1001259. DOI: 10.1371/journal.pbio.1001259.

Ngandu, Tiia; Lehtisalo, Jenni; Solomon, Alina; Levälahti, Esko; Ahtiluoto, Satu; Antikainen, Riitta et al. (2015): A 2 year multidomain intervention of diet, exercise, cognitive training, and vascular risk monitoring versus control to prevent cognitive decline in at-risk elderly people (FINGER): a randomised controlled trial. In: *Lancet (London, England)* 385 (9984), S. 2255–2263. DOI: 10.1016/S0140-6736(15)60461-5.

O'Donnell, John; Zeppenfeld, Douglas; McConnell, Evan; Pena, Salvador; Nedergaard, Maiken (2012): Norepinephrine: a neuromodulator that boosts the function of multiple cell types to optimize CNS performance. In: *Neurochemical research* 37 (11), S. 2496–2512. DOI: 10.1007/s11064-012-0818-x.

Oe, Yuki; Wang, Xiaowen; Patriarchi, Tommaso; Konno, Ayumu; Ozawa, Katsuya; Yahagi, Kazuko et al. (2020a): Distinct temporal integration of noradrenaline signaling by astrocytic second messengers during vigilance. In: *Nat Commun* 11 (1), S. 471. DOI: 10.1038/s41467-020-14378-x.

Oe, Yuki; Wang, Xiaowen; Patriarchi, Tommaso; Konno, Ayumu; Ozawa, Katsuya; Yahagi, Kazuko et al. (2020b): Distinct temporal integration of noradrenaline signaling by astrocytic second messengers during vigilance. In: *Nature communications* 11 (1), S. 471. DOI: 10.1038/s41467-020-14378-x.

Okaty, Benjamin W.; Sugino, Ken; Nelson, Sacha B. (2011): Cell type-specific transcriptomics in the brain. In: *J. Neurosci.* 31 (19), S. 6939–6943. DOI: 10.1523/JNEUROSCI.0626-11.2011.

Palygin, Oleg; Lalo, Ulyana; Verkhratsky, Alexei; Pankratov, Yuriy (2010): Ionotropic NMDA and P2X1/5 receptors mediate synaptically induced Ca2+ signalling in cortical astrocytes. In: *Cell calcium* 48 (4), S. 225–231. DOI: 10.1016/j.ceca.2010.09.004.

Panatier, Aude; Vallée, Joanne; Haber, Michael; Murai, Keith K.; Lacaille, Jean-Claude; Robitaille, Richard (2011): Astrocytes are endogenous regulators of basal transmission at central synapses. In: *Cell* 146 (5), S. 785–798. DOI: 10.1016/j.cell.2011.07.022.

Panza, Francesco; Solfrizzi, Vincenzo; Seripa, Davide; Imbimbo, Bruno P.; Lozupone, Madia; Santamato, Andrea et al. (2016): Tau-Centric Targets and Drugs in Clinical Development for the Treatment of Alzheimer's Disease. In: *BioMed research international* 2016, S. 3245935. DOI: 10.1155/2016/3245935.

Papouin, Thomas; Dunphy, Jaclyn; Tolman, Michaela; Foley, Jeannine C.; Haydon, Philip G. (2017): Astrocytic control of synaptic function. In: *Philosophical Transactions of the Royal Society B: Biological Sciences* 372 (1715). DOI: 10.1098/rstb.2016.0154.

Patel, Sandip; Docampo, Roberto (2010): Acidic calcium stores open for business: expanding the potential for intracellular Ca2+ signaling. In: *Trends in cell biology* 20 (5), S. 277–286. DOI: 10.1016/j.tcb.2010.02.003.

Paukert, Martin; Agarwal, Amit; Cha, Jaepyeong; van Doze, A.; Kang, Jin U.; Bergles, Dwight E. (2014): Norepinephrine controls astroglial responsiveness to local circuit activity. In: *Neuron* 82 (6), S. 1263–1270. DOI: 10.1016/j.neuron.2014.04.038.

Pekny, Milos; Wilhelmsson, Ulrika; Pekna, Marcela (2014): The dual role of astrocyte activation and reactive gliosis. In: *Neuroscience letters* 565, S. 30–38. DOI: 10.1016/j.neulet.2013.12.071.

Perea, Gertrudis; Araque, Alfonso (2005): Properties of synaptically evoked astrocyte calcium signal reveal synaptic information processing by astrocytes. In: *J. Neurosci.* 25 (9), S. 2192–2203. DOI: 10.1523/JNEUROSCI.3965-04.2005.

Perez-Nievas, Beatriz G.; Serrano-Pozo, Alberto (2018): Deciphering the Astrocyte Reaction in Alzheimer's Disease. In: *Frontiers in aging neuroscience* 10, S. 114. DOI: 10.3389/fnagi.2018.00114.

Petzold, Gabor C.; Murthy, Venkatesh N. (2011): Role of Astrocytes in Neurovascular Coupling. In: *Neuron* 71 (5), S. 782–797. DOI: 10.1016/j.neuron.2011.08.009.

Pike, Christian J.; Cummings, Brian J.; Cotman, Carl W. (1995): Early association of reactive astrocytes with senile plaques in Alzheimer's disease. In: *Experimental Neurology* 132 (2), S. 172–179. DOI: 10.1016/0014-4886(95)90022-5.

Pirttimaki, Tiina Maria; Codadu, Neela Krushna; Awni, Alia; Pratik, Pandey; Nagel, David Andrew; Hill, Eric James et al. (2013): α7 Nicotinic receptor-mediated astrocytic gliotransmitter release: Aβ effects in a preclinical Alzheimer's mouse model. In: *PloS one* 8 (11), e81828. DOI: 10.1371/journal.pone.0081828.

Poskanzer, Kira E.; Yuste, Rafael (2016): Astrocytes regulate cortical state switching in vivo. In: *Proceedings of the National Academy of Sciences of the United States of America* 113 (19), E2675-84. DOI: 10.1073/pnas.1520759113.

Radde, Rebecca; Bolmont, Tristan; Kaeser, Stephan A.; Coomaraswamy, Janaky; Lindau, Dennis; Stoltze, Lars et al. (2006): Aβ42-driven cerebral amyloidosis in transgenic mice reveals early and robust pathology. In: *EMBO Rep* 7 (9), S. 940–946. DOI: 10.1038/sj.embor.7400784.

Raffai, R. L.; Dong, L. M.; Farese, R. V.; Weisgraber, K. H. (2001): Introduction of human apolipoprotein E4 "domain interaction" into mouse apolipoprotein E. In: *Proceedings of the National Academy of Sciences of the United States of America* 98 (20), S. 11587–11591. DOI: 10.1073/pnas.201279298.

Rakers, Cordula; Schleif, Melvin; Blank, Nelli; Matušková, Hana; Ulas, Thomas; Händler, Kristian et al. (2019): Stroke target identification guided by astrocyte transcriptome analysis. In: *Glia* 67 (4), S. 619–633. DOI: 10.1002/glia.23544.

Rea, Irene Maeve; Gibson, David S.; McGilligan, Victoria; McNerlan, Susan E.; Alexander, H. Denis; Ross, Owen A. (2018): Age and Age-Related Diseases: Role of Inflammation Triggers and Cytokines. In: *Frontiers in Immunology* 9, S. 586. DOI: 10.3389/fimmu.2018.00586.

Reichenbach, Nicole; Delekate, Andrea; Breithausen, Björn; Keppler, Kevin; Poll, Stefanie; Schulte, Theresa et al. (2018): P2Y1 receptor blockade normalizes network dysfunction and cognition in an Alzheimer's disease model. In: *The Journal of experimental medicine* 215 (6), S. 1649–1663. DOI: 10.1084/jem.20171487.

Reichenbach, Nicole; Delekate, Andrea; Plescher, Monika; Schmitt, Franziska; Krauss, Sybille; Blank, Nelli et al. (2019): Inhibition of Stat3-mediated astrogliosis ameliorates pathology in an Alzheimer's disease model. In: *EMBO molecular medicine* 11 (2). DOI: 10.15252/emmm.201809665.

Robillard, Katelyn N.; Lee, Kim M.; Chiu, Kevin B.; MacLean, Andrew G. (2016): Glial cell morphological and density changes through the lifespan of rhesus macaques. In: *Brain, behavior, and immunity* 55, S. 60–69. DOI: 10.1016/j.bbi.2016.01.006.

Rodríguez, José J.; Yeh, Chia-Yu; Terzieva, Slavica; Olabarria, Markel; Kulijewicz-Nawrot, Magdalena; Verkhratsky, Alexei (2014): Complex and region-specific changes in astroglial markers in the aging brain. In: *Neurobiology of aging* 35 (1), S. 15–23. DOI: 10.1016/j.neurobiolaging.2013.07.002.

Rudy, Carolyn C.; Hunsberger, Holly C.; Weitzner, Daniel S.; Reed, Miranda N. (2015): The role of the tripartite glutamatergic synapse in the pathophysiology of Alzheimer's disease. In: *Aging and disease* 6 (2), S. 131–148. DOI: 10.14336/AD.2014.0423.

Rungta, Ravi L.; Bernier, Louis-Philippe; Dissing-Olesen, Lasse; Groten, Christopher J.; LeDue, Jeffrey M.; Ko, Rebecca et al. (2016): Ca2+ transients in astrocyte fine processes occur via Ca2+ influx in the adult mouse hippocampus. In: *Glia* 64 (12), S. 2093–2103. DOI: 10.1002/glia.23042.

Sakono, Masafumi; Zako, Tamotsu (2010): Amyloid oligomers: formation and toxicity of Abeta oligomers. In: *The FEBS journal* 277 (6), S. 1348–1358. DOI: 10.1111/j.1742-4658.2010.07568.x.

Salloway, Stephen; Sperling, Reisa; Fox, Nick C.; Blennow, Kaj; Klunk, William; Raskind, Murray et al. (2014): Two phase 3 trials of bapineuzumab in mild-to-moderate Alzheimer's disease. In: *N Engl J Med* 370 (4), S. 322–333. DOI: 10.1056/NEJMoa1304839.

Sanz, Elisenda; Yang, Linghai; Su, Thomas; Morris, David R.; McKnight, G. Stanley; Amieux, Paul S. (2009): Cell-type-specific isolation of ribosome-associated mRNA from complex tissues. In: *Proceedings of the National Academy of Sciences of the United States of America* 106 (33), S. 13939–13944. DOI: 10.1073/pnas.0907143106.

Schenk, D.; Barbour, R.; Dunn, W.; Gordon, G.; Grajeda, H.; Guido, T. et al. (1999): Immunization with amyloid-beta attenuates Alzheimer-disease-like pathology in the PDAPP mouse. In: *Nature* 400 (6740), S. 173–177. DOI: 10.1038/22124.

Schiemann, Julia; Puggioni, Paolo; Dacre, Joshua; Pelko, Miha; Domanski, Aleksander; van Rossum, Mark C. W.; Duguid, Ian (2015): Cellular mechanisms underlying behavioral state-dependent bidirectional modulation of motor cortex output. In: *Cell reports* 11 (8), S. 1319–1330. DOI: 10.1016/j.celrep.2015.04.042.

Schindelin, Johannes; Arganda-Carreras, Ignacio; Frise, Erwin; Kaynig, Verena; Longair, Mark; Pietzsch, Tobias et al. (2012): Fiji: an open-source platform for biological-image analysis. In: *Nature methods* 9 (7), S. 676–682. DOI: 10.1038/nmeth.2019.

Schipke, Carola G.; Haas, Brigitte; Kettenmann, Helmut (2008): Astrocytes discriminate and selectively respond to the activity of a subpopulation of neurons within the barrel cortex. In: *Cerebral cortex (New York, N.Y. : 1991)* 18 (10), S. 2450–2459. DOI: 10.1093/cercor/bhn009.

Serrano-Pozo, Alberto; Muzikansky, Alona; Gómez-Isla, Teresa; Growdon, John H.; Betensky, Rebecca A.; Frosch, Matthew P.; Hyman, Bradley T. (2013): Differential relationships of reactive astrocytes and microglia to fibrillar amyloid deposits in Alzheimer disease. In: *Journal of neuropathology and experimental neurology* 72 (6), S. 462–471. DOI: 10.1097/NEN.0b013e3182933788.

Sherrington, R.; Rogaev, E. I.; Liang, Y.; Rogaeva, E. A.; Levesque, G.; Ikeda, M. et al. (1995): Cloning of a gene bearing missense mutations in early-onset familial Alzheimer's disease. In: *Nature* 375 (6534), S. 754–760. DOI: 10.1038/375754a0.

Shibasaki, Koji; Ishizaki, Yasuki; Mandadi, Sravan (2013): Astrocytes express functional TRPV2 ion channels. In: *Biochemical and biophysical research communications* 441 (2), S. 327–332. DOI: 10.1016/j.bbrc.2013.10.046.

Shigetomi, Eiji; Bushong, Eric A.; Haustein, Martin D.; Tong, Xiaoping; Jackson-Weaver, Olan; Kracun, Sebastian et al. (2013): Imaging calcium microdomains within entire astrocyte territories and endfeet with GCaMPs expressed using adeno-associated viruses. In: *The Journal of general physiology* 141 (5), S. 633–647. DOI: 10.1085/jgp.201210949.

Shigetomi, Eiji; Patel, Sandip; Khakh, Baljit S. (2016): Probing the Complexities of Astrocyte Calcium Signaling. In: *Trends in cell biology* 26 (4), S. 300–312. DOI: 10.1016/j.tcb.2016.01.003.

Simpson, Julie E.; Ince, Paul G.; Shaw, Pamela J.; Heath, Paul R.; Raman, Rohini; Garwood, Claire J. et al. (2011): Microarray analysis of the astrocyte transcriptome in the aging brain: relationship to Alzheimer's pathology and APOE genotype. In: *Neurobiology of aging* 32 (10), S. 1795–1807. DOI: 10.1016/j.neurobiolaging.2011.04.013.

Sisalli, M. J.; Secondo, A.; Esposito, A.; Valsecchi, V.; Savoia, C.; Di Renzo, G. F. et al. (2014): Endoplasmic reticulum refilling and mitochondrial calcium extrusion promoted in neurons by NCX1 and NCX3 in ischemic preconditioning are determinant for neuroprotection. In: *Cell Death Differ* 21 (7), S. 1142–1149. DOI: 10.1038/cdd.2014.32.

Sita, Giulia; Hrelia, Patrizia; Graziosi, Agnese; Ravegnini, Gloria; Morroni, Fabiana (2018): TRPM2 in the Brain: Role in Health and Disease. In: *Cells* 7 (7). DOI: 10.3390/cells7070082.

Small, Scott A.; Duff, Karen (2008): Linking Abeta and tau in late-onset Alzheimer's disease: a dual pathway hypothesis. In: *Neuron* 60 (4), S. 534–542. DOI: 10.1016/j.neuron.2008.11.007.

Sofroniew, Michael V. (2009): Molecular dissection of reactive astrogliosis and glial scar formation. In: *Trends in neurosciences* 32 (12), S. 638–647. DOI: 10.1016/j.tins.2009.08.002.

Sofroniew, Michael V.; Vinters, Harry V. (2010): Astrocytes: biology and pathology. In: *Acta neuropathologica* 119 (1), S. 7–35. DOI: 10.1007/s00401-009-0619-8.

Sokolow, Sophie; Luu, Sanh H.; Headley, Alison J.; Hanson, Alecia Y.; Kim, Taeree; Miller, Carol A. et al. (2011): High levels of synaptosomal Na(+)-Ca(2+) exchangers (NCX1, NCX2, NCX3) co-localized with amyloid-beta in human cerebral cortex affected by Alzheimer's disease. In: *Cell calcium* 49 (4), S. 208–216. DOI: 10.1016/j.ceca.2010.12.008.

Somjen, G. G. (1988): Nervenkitt: notes on the history of the concept of neuroglia. In: *Glia* 1 (1), S. 2–9. DOI: 10.1002/glia.440010103.

Srinivasan, Karpagam; Friedman, Brad A.; Larson, Jessica L.; Lauffer, Benjamin E.; Goldstein, Leonard D.; Appling, Laurie L. et al. (2016): Untangling the brain's neuroinflammatory and neurodegenerative transcriptional responses. In: *Nature communications* 7, S. 11295. DOI: 10.1038/ncomms11295.

Srinivasan, Rahul; Huang, Ben S.; Venugopal, Sharmila; Johnston, April D.; Chai, Hua; Zeng, Hongkui et al. (2015): Ca(2+) signaling in astrocytes from Ip3r2(-/-) mice in brain slices and during startle responses in vivo. In: *Nature neuroscience* 18 (5), S. 708–717. DOI: 10.1038/nn.4001.

Stobart, Jillian L.; Ferrari, Kim David; Barrett, Matthew J. P.; Glück, Chaim; Stobart, Michael J.; Zuend, Marc; Weber, Bruno (2018a): Cortical Circuit Activity Evokes Rapid Astrocyte Calcium

Signals on a Similar Timescale to Neurons. In: *Neuron* 98 (4), 726-735.e4. DOI: 10.1016/j.neuron.2018.03.050.

Stobart, Jillian L.; Ferrari, Kim David; Barrett, Matthew J. P.; Stobart, Michael J.; Looser, Zoe J.; Saab, Aiman S.; Weber, Bruno (2018b): Long-term In Vivo Calcium Imaging of Astrocytes Reveals Distinct Cellular Compartment Responses to Sensory Stimulation. In: *Cerebral cortex (New York, N.Y. : 1991)* 28 (1), S. 184–198. DOI: 10.1093/cercor/bhw366.

Straub, Stephen V.; Bonev, Adrian D.; Wilkerson, M. Keith; Nelson, Mark T. (2006): Dynamic inositol trisphosphate-mediated calcium signals within astrocytic endfeet underlie vasodilation of cerebral arterioles. In: *The Journal of general physiology* 128 (6), S. 659–669. DOI: 10.1085/jgp.200609650.

Su, Joseph H.; Cummings, Brian J.; Cotman, Carl W. (1993): Identification and distribution of axonal dystrophic neurites in Alzheimer's disease. In: *Brain research* 625 (2), S. 228–237. DOI: 10.1016/0006-8993(93)91063-X.

Swartzlander, Dan B.; Propson, Nicholas E.; Roy, Ethan R.; Saito, Takashi; Saido, Takaomi; Wang, Baiping; Zheng, Hui (2018): Concurrent cell type-specific isolation and profiling of mouse brains in inflammation and Alzheimer's disease. In: *JCI insight* 3 (13). DOI: 10.1172/jci.insight.121109.

Szot, Patricia; White, Sylvia S.; Greenup, J. Lynne; Leverenz, James B.; Peskind, Elaine R.; Raskind, Murray A. (2006): Compensatory changes in the noradrenergic nervous system in the locus ceruleus and hippocampus of postmortem subjects with Alzheimer's disease and dementia with Lewy bodies. In: *J. Neurosci.* 26 (2), S. 467–478. DOI: 10.1523/JNEUROSCI.4265-05.2006.

TAKANO, T.; HAN, X.; DEANE, R.; ZLOKOVIC, B.; NEDERGAARD, M. (2007): Two-Photon Imaging of Astrocytic Ca2+ Signaling and the Microvasculature in Experimental Mice Models of Alzheimer's Disease. In: *Annals of the New York Academy of Sciences* 1097 (1), S. 40–50. DOI: 10.1196/annals.1379.004.

Takata, Norio; Mishima, Tsuneko; Hisatsune, Chihiro; Nagai, Terumi; Ebisui, Etsuko; Mikoshiba, Katsuhiko; Hirase, Hajime (2011): Astrocyte calcium signaling transforms cholinergic modulation to cortical plasticity in vivo. In: *J. Neurosci.* 31 (49), S. 18155–18165. DOI: 10.1523/JNEUROSCI.5289-11.2011.

Tanaka, Mika; Shih, Pei-Yu; Gomi, Hiroshi; Yoshida, Takamasa; Nakai, Junichi; Ando, Reiko et al. (2013): Astrocytic Ca2+ signals are required for the functional integrity of tripartite synapses. In: *Molecular brain* 6, S. 6. DOI: 10.1186/1756-6606-6-6.

The Fine Structure of the Nervous System. Neurons and their Supporting Cells. 3rd edition (1991). In: *Journal of neuropathology and experimental neurology* 50 (3), 282.1-282.

Thordardottir, Steinunn; Kinhult Ståhlbom, Anne; Almkvist, Ove; Thonberg, Håkan; Eriksdotter, Maria; Zetterberg, Henrik et al. (2017): The effects of different familial Alzheimer's disease mutations on APP processing in vivo. In: *Alzheimer's research & therapy* 9 (1), S. 9. DOI: 10.1186/s13195-017-0234-1.

Thrane, Alexander Stanley; Rangroo Thrane, Vinita; Zeppenfeld, Douglas; Lou, Nanhong; Xu, Qiwu; Nagelhus, Erlend Arnulf; Nedergaard, Maiken (2012): General anesthesia selectively disrupts astrocyte calcium signaling in the awake mouse cortex. In: *Proceedings of the National Academy of Sciences of the United States of America* 109 (46), S. 18974–18979. DOI: 10.1073/pnas.1209448109.

van Broeckhoven, C.; Backhovens, H.; Cruts, M.; Winter, G. de; Bruyland, M.; Cras, P.; Martin, J. J. (1992): Mapping of a gene predisposing to early-onset Alzheimer's disease to chromosome 14q24.3. In: *Nat Genet* 2 (4), S. 335–339. DOI: 10.1038/ng1292-335.

van Dam, Debby; Deyn, Peter Paul de (2006): Drug discovery in dementia: the role of rodent models. In: *Nature reviews. Drug discovery* 5 (11), S. 956–970. DOI: 10.1038/nrd2075.

van Dyck, Christopher H. (2018): Anti-Amyloid-β Monoclonal Antibodies for Alzheimer's Disease: Pitfalls and Promise. In: *Biological psychiatry* 83 (4), S. 311–319. DOI: 10.1016/j.biopsych.2017.08.010.

Verkhratsky, Alexei; Matteoli, Michela; Parpura, Vladimir; Mothet, Jean-Pierre; Zorec, Robert (2016): Astrocytes as secretory cells of the central nervous system: idiosyncrasies of vesicular secretion. In: *The EMBO journal* 35 (3), S. 239–257. DOI: 10.15252/embj.201592705.

Verkhratsky, Alexei; Olabarria, Markel; Noristani, Harun N.; Yeh, Chia-Yu; Rodriguez, Jose Julio (2010): Astrocytes in Alzheimer's disease. In: *Neurotherapeutics : the journal of the American Society for Experimental NeuroTherapeutics* 7 (4), S. 399–412. DOI: 10.1016/j.nurt.2010.05.017.

Volterra, Andrea; Liaudet, Nicolas; Savtchouk, Iaroslav (2014): Astrocyte Ca^{2+} signalling: an unexpected complexity. In: *Nat Rev Neurosci* 15 (5), S. 327–335. DOI: 10.1038/nrn3725.

Wang, Jing; Jackson, Michael F.; Xie, Yu-Feng (2016): Glia and TRPM2 Channels in Plasticity of Central Nervous System and Alzheimer's Diseases. In: *Neural plasticity* 2016, S. 1680905. DOI: 10.1155/2016/1680905.

Wang, Yizhi; DelRosso, Nicole V.; Vaidyanathan, Trisha V.; Cahill, Michelle K.; Reitman, Michael E.; Pittolo, Silvia et al. (2019): Accurate quantification of astrocyte and neurotransmitter fluorescence dynamics for single-cell and population-level physiology. In: *Nat Neurosci* 22 (11), S. 1936–1944. DOI: 10.1038/s41593-019-0492-2.

Wegiel, J.; Wisniewski, H. M. (1994): Rosenthal fibers, eosinophilic inclusions, and anchorage densities with desmosome-like structures in astrocytes in Alzheimer's disease. In: *Acta neuropathologica* 87 (4), S. 355–361. DOI: 10.1007/bf00313604.

Wink, M. R.; Braganhol, E.; Tamajusuku, A. S. K.; Lenz, G.; Zerbini, L. F.; Libermann, T. A. et al. (2006): Nucleoside triphosphate diphosphohydrolase-2 (NTPDase2/CD39L1) is the dominant ectonucleotidase expressed by rat astrocytes. In: *Neuroscience* 138 (2), S. 421–432. DOI: 10.1016/j.neuroscience.2005.11.039.

Wisniewski, Thomas; Konietzko, Uwe (2008): Amyloid-beta immunisation for Alzheimer's disease. In: *The Lancet Neurology* 7 (9), S. 805–811. DOI: 10.1016/S1474-4422(08)70170-4.

Wit, Nienke M. de; den Hoedt, Sandra; Martinez-Martinez, Pilar; Rozemuller, Annemieke J.; Mulder, Monique T.; Vries, Helga E. de (2019): Astrocytic ceramide as possible indicator of neuroinflammation. In: *Journal of neuroinflammation* 16 (1), S. 48. DOI: 10.1186/s12974-019-1436-1.

Witcher, Mark R.; Kirov, Sergei A.; Harris, Kristen M. (2007): Plasticity of perisynaptic astroglia during synaptogenesis in the mature rat hippocampus. In: *Glia* 55 (1), S. 13–23. DOI: 10.1002/glia.20415.

Witcher, Mark R.; Park, Yong D.; Lee, Mark R.; Sharma, Suash; Harris, Kristen M.; Kirov, Sergei A. (2010): Three-dimensional relationships between perisynaptic astroglia and human hippocampal synapses. In: *Glia* 58 (5), S. 572–587. DOI: 10.1002/glia.20946.

Wojtukiewicz, Marek Z.; Hempel, Dominika; Sierko, Ewa; Tucker, Stephanie C.; Honn, Kenneth V. (2019): Endothelial Protein C Receptor (EPCR), Protease Activated Receptor-1 (PAR-1) and Their Interplay in Cancer Growth and Metastatic Dissemination. In: *Cancers* 11 (1). DOI: 10.3390/cancers11010051.

Wu, Tiffany; Dejanovic, Borislav; Gandham, Vineela D.; Gogineni, Alvin; Edmonds, Rose; Schauer, Stephen et al. (2019): Complement C3 Is Activated in Human AD Brain and Is Required for Neurodegeneration in Mouse Models of Amyloidosis and Tauopathy. In: *Cell reports* 28 (8), 2111-2123.e6. DOI: 10.1016/j.celrep.2019.07.060.

Yamada, Marina; Chiba, Tomohiro; Sasabe, Jumpei; Nawa, Mikiro; Tajima, Hirohisa; Niikura, Takako et al. (2005): Implanted cannula-mediated repetitive administration of Abeta25-35 into the mouse cerebral ventricle effectively impairs spatial working memory. In: *Behavioural brain research* 164 (2), S. 139–146. DOI: 10.1016/j.bbr.2005.03.026.

Yang, Ting; Li, Shaomin; Xu, Huixin; Walsh, Dominic M.; Selkoe, Dennis J. (2017): Large Soluble Oligomers of Amyloid β-Protein from Alzheimer Brain Are Far Less Neuroactive Than the Smaller Oligomers to Which They Dissociate. In: *The Journal of neuroscience : the official journal of the Society for Neuroscience* 37 (1), S. 152–163. DOI: 10.1523/JNEUROSCI.1698-16.2016.

Yardeni, Tal; Eckhaus, Michael; Morris, H. Douglas; Huizing, Marjan; Hoogstraten-Miller, Shelley (2011): Retro-orbital injections in mice. In: *Lab animal* 40 (5), S. 155–160. DOI: 10.1038/laban0511-155.

Yu, Guangchuang; Wang, Li-Gen; Han, Yanyan; He, Qing-Yu (2012): clusterProfiler: an R package for comparing biological themes among gene clusters. In: *Omics : a journal of integrative biology* 16 (5), S. 284–287. DOI: 10.1089/omi.2011.0118.

Zamanian, Jennifer L.; Xu, Lijun; Foo, Lynette C.; Nouri, Navid; Zhou, Lu; Giffard, Rona G.; Barres, Ben A. (2012): Genomic analysis of reactive astrogliosis. In: *J. Neurosci.* 32 (18), S. 6391–6410. DOI: 10.1523/JNEUROSCI.6221-11.2012.

Zhang, Qi; Pangrsic, Tina; Kreft, Marko; Krzan, Mojca; Li, Nianzhen; Sul, Jai-Yoon et al. (2004): Fusion-related release of glutamate from astrocytes. In: *The Journal of biological chemistry* 279 (13), S. 12724–12733. DOI: 10.1074/jbc.M312845200.

Zhang, Ye; Chen, Kenian; Sloan, Steven A.; Bennett, Mariko L.; Scholze, Anja R.; O'Keeffe, Sean et al. (2014): An RNA-sequencing transcriptome and splicing database of glia, neurons, and vascular cells of the cerebral cortex. In: *J. Neurosci.* 34 (36), S. 11929–11947. DOI: 10.1523/JNEUROSCI.1860-14.2014.

Zheng, Kaiyu; Bard, Lucie; Reynolds, James P.; King, Claire; Jensen, Thomas P.; Gourine, Alexander V.; Rusakov, Dmitri A. (2015): Time-Resolved Imaging Reveals Heterogeneous Landscapes of Nanomolar Ca(2+) in Neurons and Astroglia. In: *Neuron* 88 (2), S. 277–288. DOI: 10.1016/j.neuron.2015.09.043.

Zlokovic, Berislav V. (2008): The blood-brain barrier in health and chronic neurodegenerative disorders. In: *Neuron* 57 (2), S. 178–201. DOI: 10.1016/j.neuron.2008.01.003.

Danksagung

An erster Stelle möchte ich Prof. Dr. Gabor C. Petzold danken, dass er mir die Möglichkeit gegeben hat, bei Ihm in seiner Forschungsgruppe am DZNE meine Dissertation anfertigen zu dürfen. Dank seiner Bereuung, Zuversicht und seines Vertrauens in meine Arbeit konnte ich mich in vielen interessanten Projekten einbringen und konnte dadurch viele wertvolle wissenschaftliche Erfahrungen sammeln. Des Weiteren war es ein Privileg die Vorteile eins derart gut ausgestatteten Instituts nutzen zu dürfen.

Darüber hinaus danke ich Prof. Dr. Michael Pankratz der die Ko-Betreuung meiner Dissertation übernommen hat. Natürlich geht auch ein Dank an Prof. Dr. Irmgard Förster, die sich bereit erklärt hat, als fachnahes Mitglied der Promotionskommission beizuwohnen. Im Besonderen möchte ich Prof. Dr. Dagmar Wachten dafür danken, dass Sie als fachfremdes Mitglied in der Promotionskommission fungiert, aber besonders, dass Sie mich ermutigt hat eine wissenschaftliche Karriere anzustreben, bei der Sie mich stets mit Motivation und Begeisterung begleitet hat.

Großen Dank auch an die Mitglieder der Animal Research Facility (ARF), Imaging and Data Analysis Facility (IDAF) und der Light Microscope Facility (LMF). Ich danke auch den Kooperationspartnern Walker Jackson und Lech Kaczmarczyk für die technische Hilfestellung bei der RNA Aufreinigung und der AG Schultze, insbesondere Stefanie Warnat-Herresthal für die RNA Sequenzierung und Datenanalyse.

Ein Riesen Dankeschön geht an die gesamte AG Petzold, wir haben in diesen Jahren viel miteinander gelacht und legendäre Feste gefeiert. Besonders möchte ich Andrea und Hana dafür danken, dass sie stets mit Rat und Tat zur Seite standen und wir dadurch diverse experimentelle Schwierigkeiten gemeinsam lösen konnten. Dann danke ich natürlich Theresa und Jan für die stetige Unterstützung und die dadurch immense Entlastung im Laboralltag. Zusätzlich möchte ich meinem Tischnachbarn Christof für die ganzen Zankereien danken, die mich nicht selten in den Wahnsinn getrieben haben, jedoch auch immer wieder in gute Laune versetzt haben. Außerdem möchte ich betonen, wie großartig es sein kann, ein Teil einer solchen wissenschaftlichen Community zu sein und dadurch so viele interessante, intelligente und lustige Menschen kennenzulernen. Vielen Dank auch an die lieben Kollegen, die sich die Zeit für die Korrektur dieser Dissertation genommen haben. Moni und Steffi möchte ich dafür danken, dass sie vor allem in der letzten Phase meiner Doktorarbeit stets ein offenes Ohr für meine Belange hatten. Nicht zu vergessen ist auch die zuverlässige Hilfe von Nancy in organisatorischen Dingen außerhalb des Labors.

Mein Herzlichster Dank geht an meine bessere Hälfte Micha, der mich immer unterstützt und mir den Rücken freigehalten hat. Einen großen Dank auch an meine beste Freundin Olli die

immer sehr leidenschaftlich an Problemlösungen Anteil genommen hat. Auch meiner Familie und besonders meinen Eltern möchte ich für Ihre Bestärkung und Ihr Vertrauen in mich danken, was mir immer eine große mentale Stütze war.

Zuallerletzt möchte ich den kleinen Mäusen für die große Mitwirkung an dieser Dissertation danken.

List of Publications

Reichenbach, Nicole; Delekate, Andrea; Plescher, Monika; Schmitt, Franziska; Krauss, Sybille; Blank, Nelli et al. (2019): Inhibition of Stat3-mediated astrogliosis ameliorates pathology in an Alzheimer's disease model. In: EMBO molecular medicine 11 (2). DOI: 10.15252/emmm.201809665.

Rakers, Cordula; Schleif, Melvin; Blank, Nelli; Matušková, Hana; Ulas, Thomas; Händler, Kristian et al. (2019): Stroke target identification guided by astrocyte transcriptome analysis. In: Glia 67 (4), S. 619–633. DOI: 10.1002/glia.23544.

Björkgren, Ida; Alvarez, Luis; Blank, Nelli; Balbach, Melanie; Turunen, Heikki; Laajala, Teemu Daniel et al. (2016): Targeted inactivation of the mouse epididymal beta-defensin 41 alters sperm flagellar beat pattern and zona pellucida binding. In: Molecular and cellular endocrinology 427, S. 143–154. DOI: 10.1016/j.mce.2016.03.013.

Matthes, Frank; Hettich, Moritz M.; Schilling, Judith; Flores-Dominguez, Diana; Blank, Nelli; Wiglenda, Thomas et al. (2018): Inhibition of the MID1 protein complex: a novel approach targeting APP protein synthesis. In: Cell death discovery 4, S. 4. DOI: 10.1038/s41420-017-0003-8.

Reichenbach, Nicole; Delekate, Andrea; Breithausen, Björn; Keppler, Kevin; Poll, Stefanie; Schulte, Theresa et al. (2018): P2Y1 receptor blockade normalizes network dysfunction and cognition in an Alzheimer's disease model. In: The Journal of experimental medicine 215 (6), S. 1649–1663. DOI: 10.1084/jem.20171487.

Studies currently under review

Kaczmarczyk, Lech; Reichenbach, Nicole; Blank, Nelli; Jonson, Maria; Dittrich, Lars; Petzold, Gabor C.; Jackson, Walker (2020): Insights into calcium signaling and gene expression in astrocytes uncovered with 129S4 Slc1a3-2A-CreERT2 knock-in mice.